UNIVERSIDADE DE LISBOA
FACULDADE DE CIÊNCIAS
DEPARTAMENTO DE QUÍMICA E BIOQUÍMICA

Synthesis and characterization of organic and inorganic media with high potential as cathode materials for Li-ion batteries

Catarina Carapeta Gustavo

Dissertação
Mestrado em Química Tecnológica
Especialização em Química Tecnológica

2013

UNIVERSIDADE DE LISBOA
FACULDADE DE CIÊNCIAS
DEPARTAMENTO DE QUÍMICA E BIOQUÍMICA

Synthesis and characterization of organic and inorganic media with high potential as cathode materials for Li-ion batteries

Catarina Carapeta Gustavo

Dissertação
Mestrado em Química Tecnológica
Especialização em Química Tecnológica

Orientadores:
Doutor Jorge Palma Correia (Centro de Química e Bioquímica, DQB-FCUL)
Dr. Jens-Erik Jørgensen (Chemistry Department, Aarhus University)

2013

Acknowledgments / Agradecimentos

Quero agradecer ao *Professor Jorge Correia* por ter aceite ser meu orientador nesta atribulada viagem e pela sua boa disposição contagiante mesmo nos momentos mais críticos.

To *Professor Jens-Erik* for all the support and for accepting an unknown Portuguese girl in his lab spending his time and reagents.

À minha querida amiga *Professora Joana Rodrigues* que me ajudou a descobrir a paixão pela Química, e me guiou até ao Curso de Química Tecnológica.

To *Britta*, *Simon* and *Yanbin Shen* for helping with the characterization techniques.

À *Professora Olinda* pelas sugestões/iluminações dadas na escrita desta tese.

Às senhoras do laboratório do Grupo de Electroquímica Interfacial *Ana Mourato*, *Ana Melato* e *Joana Cabrita* pelo apoio e conselhos dados durante este período de trabalho.

To all my ERASMUS friends *Maud Hennion, Gülcan Çevik, Fatih Aydin, Furkan Aytekin, Bariş Özcan, Tanju Gökmen, Max Friedrich* and *Saskia Klumpers* that always told me "You can do it! Your material-thingy will work out...someday…", especially to *Payam Javadian* that put up with me from Monday to Friday, and sometimes on Saturday in "*The Office*".

Às portuguesas na Dinamarca por tudo o que aconteceu em Aarhus. *Maria Pinto*, *Maria Primo* e em especial à *Ana Miguel Fernandes* que confiaram numa desconhecida e que se tornou numa amiga para a Vida.

À pessoa que escolheu o mesmo orientador que eu, colega nesta "tortura anual" *Isabel Ornelas*. Desde o polimento de electrodos até ao "arrancar de cabelos" e na escrita desta tese, nunca deixámos de sorrir.

À *Nádia Coelho* por continuar a meu lado, até mesmo na Dinamarca, e ao *Nuno Varela* por continuar a dar-me na cabeça por tudo e por nada.

À minha amiga socióloga de longa data, *Joana Baião*, que mesmo estando a estudar no ISCTE, continua a ser "a minha gaja"...excepto uma vez por ano no mês de Setembro.

À *Joana Martins* por ser uma melguinha preocupada e por estar sempre preocupada com a Madrinha.

Ao meu *Padrinho João França* e Pseudo-Padrinho Milan Chhaganlal, que durante estes 5 anos me mostraram o quão boa tinha sido a minha escolha de Curso.

À minha nova *buddy Cátia Crespo*, por toda a sua maldade fofinha, palavras sábias e apoio nestes últimos tempos.

À pessoa que não descansou até eu dizer o "SIM!", *Marta Mourão*, amiga que não vive sem o meu conhecimento e eu não vivo sem o dela. Ainda bem que me convenceste a fazer ERASMUS.

Ao meu *Afilhado Rui Gomes* pelo seu sorriso constante e por "me dar música", à minha *Netita Marisa* por me perguntar sempre "Como está a tese?" e "Se não sou eu a puxar por ti, ninguém o faz!" e à minha *Netita Joana* por arranjar uma nova maneira de chamar por mim "ÁÁÁVÓ!" e especialmente por provarem que a distância é apenas uma medida de separação entre dois pontos. Vocês são o meu orgulho e espero estar cá quando for a vossa vez.

Ao Bioquímico *Sid*, minha consciência e companheiro nesta aventura de 5 anos, pois sem ti não tinha sido a mesma coisa…se é que me entendes.

À *Cátia Loureiro* por conseguir durante um ano inteiro perguntar qual o tema da minha tese, e nunca perceber qual era.

Aos membros da minha família, em especial ao meu primo *Filipe Tempero* e à minha prima *Maria João Barbosa*, pois sem o vosso apoio nunca poderia ter ido para outro País. Aos outros membros mais recentes da minha família, os casalinhos *Márcia* e *João*, e à minha irmãdrasta e ao meu cunhadrasto *Rita* e *Lau*, por me "incentivarem" (gozarem) a continuar a "estudar coisas ao contrário", e por serem uns fantásticos irmãos mais velhos.

Às minhas primas, que são mais do que irmãs, *Rita* e *Inês*, ao meu Padrasto *Artur* por ser mais do que um Pai e um amigo, e à melga da minha Mãe *Rosa Augusta*, que só este ano é que decorou qual era o nome do meu curso.

E a todos os outros que contribuiram da sua maneira ao meu crescimento e evolução neste período.

Resumo

Preparação e caracterização de materiais com potential utilização como cátodos para baterias de ião-Li, que inclui o estudo de materiais orgânicos e inorgânicos

Neste trabalho foram sintetizados e caracterizados materiais que possam funcionar como cátodos nas baterias de ião-Litío. Foram estudados dois tipos de materiais, do tipo orgânico e inorgânico.

Primeiramente procedeu-se ao estudo dos materiais de natureza orgânica e dentro deste tipo de materiais foram escolhidos os polímeros condutores, mais concretamente o poli(3,4-etilenodioxitiofeno) doravante designado por PEDOT, dopado com poliestirenosulfonato doravante designado por PSS. Foi assim possível obter, por via electroquímica, eléctrodos modificados com filmes de PEDOT-PSS que foram os materiais estudados neste trabalho.

Os filmes de PEDOT-PSS foram sintetizados por electrodeposição num eléctrodo de platina a partir de soluções aquosas do monómero (10 mM EDOT) e do dopante (0.1 M PSS). A electropolimerização foi efectuada através de dois métodos: electrodeposição em modo galvanostático, onde foi aplicada uma corrente constante (i_g=0.2 mA.cm^{-2}) durante um certo período de tempo (t=275 s) e pelo modo potenciodinâmico, onde se efectuaram diversos varrimentos de potencial (80 ciclos) dentro de uma gama de potenciais (-0.7 a 0.8 V vs SCE) a uma velocidade de varrimento de ν=50 mV.s^{-1}. As condições de electropolimerização foram previamente optimizadas e seleccionadas de modo a obter eléctrodos modificados por filmes de PEDOT-PSS estáveis e homogéneos e com electroactividade semelhante para os dois modos de crescimento.

Os filmes obtidos foram caracterizados por voltametria cíclica (CV), Microgravimetria (EQCM), Deflexão de Raio Laser/Técnica de Efeito de Miragem (PBD) e por Elipsometria (ELL).

O processo de dopagem/dedopagem dos eléctrodos modificados foi estudado por voltametria cíclica em soluções orgâncias (CH_3CN) de $LiClO_4$ (0,1 M) comprovando-se que os filmes eram caracterizados por uma elevada electroactividade e estabilidade durante os processos de conversão redox. Ainda que numa bateria de ião Lítio se tenha que recorrer inevitavelmente a solventes orgânicos

(dada a reactividade do lítio em meio aquoso), o comportamento dos eléctrodos modificados foi ainda avaliado em meio aquoso com o mesmo electrólito (0,1 M $LiClO_4$) de forma a contribuir para o esclarecimento do efeito do solvente nos processos de transferência de massa decorrentes da conversão redox do polímero. Acresce ainda o facto de o lítio apresentar uma massa molar bastante baixa, o que se traduz numa dificuldade acrescida de detecção dos seus fluxos por electrogravimetria quando não solvatado, como acontece em meio orgânico.

O fenómeno da transferência de massa que tem lugar durante a conversão redox dos filmes dos polímeros modificados de PEDOT-PSS foi investigado por EQCM e PDB. A informação combinada dos dados obtidos por estas técnicas permitiu distinguir os fluxos de massa do solvente dos fluxos iónicos, podendo ser resolvidos individualmente. Os dados revelaram uma dopagem pseudo-catiónica não ideal visto que o anião perclorato também participa no processo de conversão redox, sendo a extensão relativa de cada contribuição claramente dependente do modo electroquímico utilizado na síntese do polímero.

A espessura do filme sintetizado galvanostaticamente e as suas propriedades ópticas foram avaliadas utilizando a técnica de Elipsometria. Concluiu-se que o filme de PEDOT-PSS é um filme poroso composto por duas camadas, tendo-se estimado uma espessura total de 203 nm (interna (88 nm) e externa (115 nm))

Como materiais de interesse para cátodo de natureza inorgânica, os que têm mostrado mais aplicabilidade e interesse de estudo são os compostos de intercalação de Lítio, ou seja, que já contêm lítio na sua constituição. O escolhido para este trabalho foi o composto de intercalação de Lítio Ferro Silicato (Li_2FeSiO_4), contendo também Silício e o Ferro que são dos elementos mais abundantes da crosta terrestre (2º e 4º respectivamente).

Pretendendo-se devenvolver um método de síntese altamente eficiente através de percursores baratos e abundantes e recorrendo a material de laboratório simples, de modo a minimizar os custos de produção, foram estudados e desenvolvidos três métodos distintos de preparação dos compostos: síntese hidrotérmica (HTS), reacção de estado sólido (SS) e de combustão (CM). Tendo em atenção o descrito anteriormente, para o primeiro método os reagentes utilizados foram o LiOH, SiO_2 e $FeCl_2 \cdot 4H_2O$ em diferentes razões estequiométricas, enquanto que para os outros dois

métodos foi usado o Li_2CO_3, SiO_2 e $FeC_2O_4 \cdot 2H_2O$ com a adição de ácido cítrico no método CM. Estes métodos sofreram várias modificações de optimização tendo sido possível obter o composto através do método hidrotérmico, apesar de ainda conter alguma impurezas como o Fe_2SiO_4 e Li_2SiO_3. Este foi então o composto utilizado para os estudos de caracterização.

A caracterização foi feita através das técnicas de Análise Termogravimétrica (TGA/DSC), Difracção de Raios-X de Pós (XRD), Microscopia Electrónica de Varrimento (SEM) e da realização de ensaios-teste de pilhas de botão de ião-Lítio utilizando este material como cátodo.

Para obter a temperatura de calcinação do composto para os métodos de SS e CM foi usada a técnica de TGA/DSC que comprovou a decomposição dos precursores até 710 ºC, onde tem lugar a última reacção endotérmica admitindo-se que é referente à formação do Lítio Ferro Silicato que se pretende obter. Deste modo, as temperaturas de calcinação utilizadas foram superiores a esta temperatura.

A estrutura destes compostos foi estudada através dos difractogramas obtidos por XRD e comprovou-se que tem uma estrutura ortorrômbica com grupo espacial Pmn_{21} tal como já tinha sido demonstrado noutros trabalhos presentes na literatura. Também foi possível comprovar que os compostos obtidos eram pouco cristalinos, o que não é desejável para a finalidade do composto uma vez que esse facto compromete a sua condutividade electrónica e iónica.

A topografia dos materiais obtidos foi caracterizada por SEM onde se verificou que há a formação de aglomerados com 7 a 10 μm de tamanho, de partículas com, aproximadamente, 250 nm de tamanho, que está dentro da gama de tamanhos desejados (50 a 250 nm).

Após esta caracterização, o desempenho electroquímico foi avaliado, utilizando células de botão construídas no laboratório com este material de cátodo e lítio metálico como ânodo. Ainda que promissores, os resultados mostram que a falta de cristalinidade dos materiais sintetizados comprometem as capacidades e eficiência das baterias, apesar de se ter obtido uma eficiência de 80% a partir do 2ºciclo de descarga da bateria.

Palavras-chave: Baterias de ião-Lítio, material de cátodo, polímeros condutores, PEDOT-PSS, Lítio ferro silicatos, PBD, EQCM, Elipsometria, XRD, SEM, TGA/DSC

Abstract

Synthesis and characterization of organic and inorganic media with high potential as cathode materials for Li-ion batteries

In this work the mass transfer phenomena taking place during the redox conversion of PEDOT-PSS films is investigated by microgravimetry (EQCM) and Probe Beam Deflection (PBD). Polymeric films were galvanostatically and potentiodynamically synthesized onto platinum electrodes from aqueous solutions. The doping/undoping processes of the modified electrodes were studied by cyclic voltammetry in organic (CH_3CN) and aqueous solutions of $LiClO_4$. The combined information of the PBD and EQCM allows distinguishing the solvent mass fluxes from that of the ions that can be resolved individually. The data revealed a non-ideal pseudo-cationic doping since the perchlorate anion also participates in the conversion process, being the relative extension of each contribution clearly dependent on the electrochemical mode used in the polymer synthesis. Also the thickness of the galvanostatically grown film and its optical properties were computed using the Ellipsometry technique. It was concluded that the PEDOT-PSS coating is a porous film composed by two layers (internal and external) with a total thickness of 203 nm.

The other cathode material of interest studied in this work was lithium iron silicate (Li_2FeSiO_4). Three cost effective synthetic methods were developed to produce lithium iron silicate starting with low cost precursors and basic laboratory equipment. The material was synthesized using a hydrothermal, solid-state and combustion method synthesis. The structure and morphology of the obtained materials were characterized by XRD and SEM. Afterwards the electrochemical performance was evaluated, using coin cells. Even promising the results suffer from the lack of crystallinity of the synthesised materials that compromises the capacities and efficiency of the batteries. Nevertheless, an interesting efficiency of 80% was obtain after the 2^{nd} cycle of discharge of the battery

Key-words: Lithium-ion battery, cathode material, conducting polymers, PEDOT-PSS, lithium iron silicates, PBD, EQCM, Ellipsometry, XDR, SEM, TGA/DSC

Index

Figures Index

Tables Index

1. Introduction

1.1. The need for batteries

Ever since the primordial times of humanity, that the evolution of our society's way-of-life had not been as sudden and important as in the last 20 years, and together with its increasing need for electric power, lead to an increase of the consumption of the primary energy sources, fossil fuel such as oil, coal and gas (Table 1.1).

Table 1.1 – Fossil fuel sources consumption in Portugal and in the World, in the years of 1990, 2000, 2010 and 2011.[1]

	Consumption / Mton							
	Portugal				**World**			
Year / Source	**1990**	**2000**	**2010**	**2011**	**1990**	**2000**	**2010**	**2011**
Oil	11.1	15.5	12.5	11.6	3158.1	3571.8	4031.9	4059.1
Coal	2.8	4.5	1.9	2.6	2207.0	2372.2	3532.0	3724.3
Gas	-	2.1	4.5	4.6	1768.6	2173.9	2843.1	2905.6

In short, the widely use of these fossil fuel sources, and the associated pollution factor, the so-called CO_2 emissions also tends to increase (Table 1.2), and nowadays the reduction of these emissions became a major concern all over the world resulting in more restrict policies in all sorts of industries.[2,3]

Table 1.2 – CO_2 emissions in Portugal and in the World, in the years of 1990, 2000, 2010 and 2011.[1]

CO_2 Emissions / Mton							
Portugal				**World**			
1990	**2000**	**2010**	**2011**	**1990**	**2000**	**2010**	**2011**
45.2	70.6	56.5	56.6	22587.2	25463.4	33040.6	34032.7

Due to all these concerns and to the electrical energy production from renewable sources start to rise, as environmental friendly and almost unlimited, and today their evolution and growing importance in the Worlds' production of electricity are shown in Table 1.3.

Table 1.3 – Renewable energies total capacity, in Portugal and in the World, in the years of 1990, 2000, 2010 and 2011.[1]

	Total capacity of renewable energies / TWh							
	Portugal				World			
Year / Source	1990	2000	2010	2011	1990	2000	2010	2011
Solar	-	9.64×10^{-3}	1.15	1.26	-	12.3	351	608
Hydro	9.3	11.7	17.0	12.2	2164.7	2659.0	3442.4	3497.9
Wind	-	0.972	33.6	36.9	-	157	1740	2100
Geothermal	0.0263	0.140	0.254	0.254	52.1	70.8	95.7	96.5

Taking the solar energy, for instance, the total amount of this type of energy reaching the upper atmosphere is 1.74×10^{17} W, but only about 50% of this energy reaches the ground, so the total solar power reaching the Earths' surface is 8.9×10^{16} W (Figure 1.1), that means 7.9×10^{17} kWh of solar energy reaching the Earths' surface every year.[4]

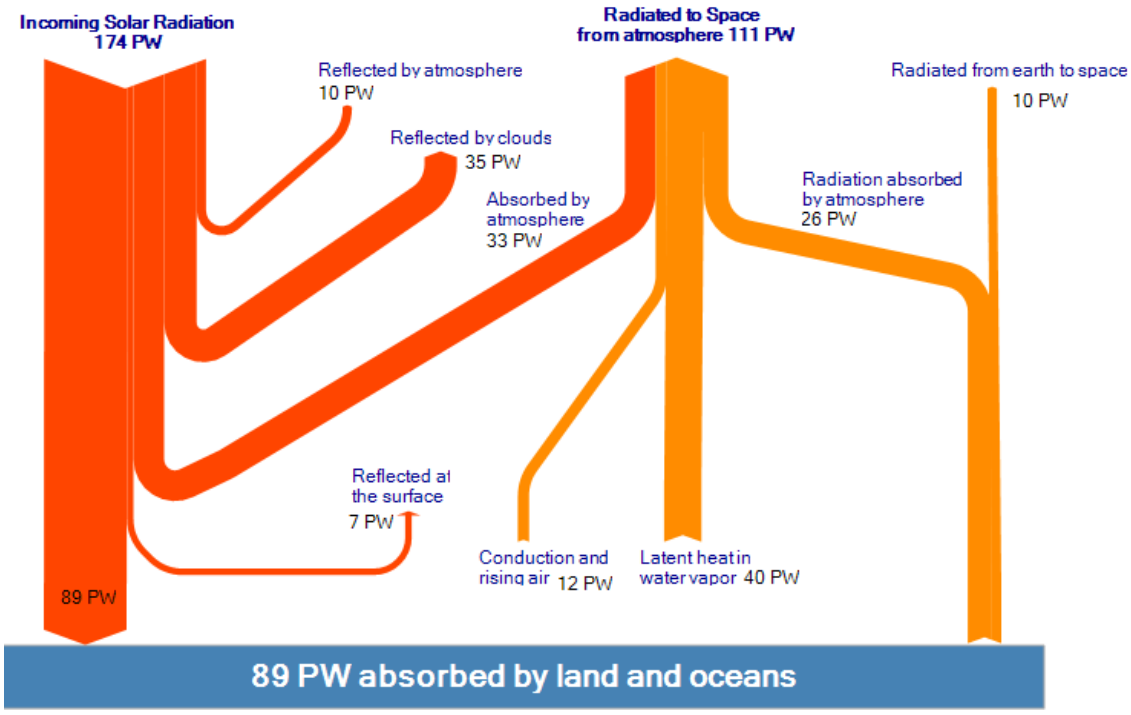

Figure 1.1 – Diagram of the incoming Solar Energy breakdown and the Earth's energy budget.[5]

From the last year electricity consumption of 2.20×10^{13} kWh, we can conclude that if we could store all the solar energy reaching the Earths' surface, we could have obtained all the energy demanded and more.

Therefore it would be a great benefit if we could store this energy. However there isn't enough technological resources to store all this energy. It is here that the batteries importance begins. The need for more efficient, powerful and long-time life batteries induced a deep research effort in this area, and nowadays most of the more common devices, from mobile-phones to computers, use Li-Ion batteries.[6,7]

1.2. Batteries - the Lithium-ion battery

A battery is an important piece in the infrastructure of an energy supply system. It can be of two kinds a primary battery that converts energy of a chemical reaction into electricity only once, or a secondary battery where the electrodes can be restored to their original chemical formula, by passing electricity back through it (therefore charging the battery). This last type of units are also called storage or rechargeable batteries and can be reused many times. Their function is to store energy in its chemical form, which will be transformed into electrical energy when the system requests it. Therefore they are responsible for ensuring uninterrupted power supply to a certain load. In a fail in the power supply system, either by default or lack of energy distributed by the source, the batteries guarantee continuous supply load.[7]

The phenomena taking place in a secondary battery involves the discharge and charge the energy of the device, as schematically illustrated in Figure 1.2 for the Li-ion type battery. During the discharge process the active material in the anode is oxidized therefore producing electrons that create the current flow from the anode onto the external circuit to the load. Simultaneously in the electrolyte, there is an internal ion flow between the electrodes from the anode to the cathode, of the ion that is responsible for the producing of current being reduced at the cathode. The reverse is therefore the charge process, and instead of a load, there is a charger that applies current into the cathode that reverses the process, and forces the flow of electrons from the cathode to the anode, therefore storing the energy in the battery for further use. While the working processes described so far describes generally the functioning of a Li-ion battery, other alternatives of operation with this kind of batteries exist, where the cathodic reaction in discharge does not require the

reduction of the Li^+ produced in the anodic reaction, but just the reduction of the cathode itself. In these cases there is an accumulation of lithium salts in the electrolyte that can origin the saturation and precipitation of such salts, causing important damages to the battery. It is therefore desirable that the lithium ion produced by the anodic reaction can be incorporated into the cathode material either as ion or as a metal atom.[8,9]

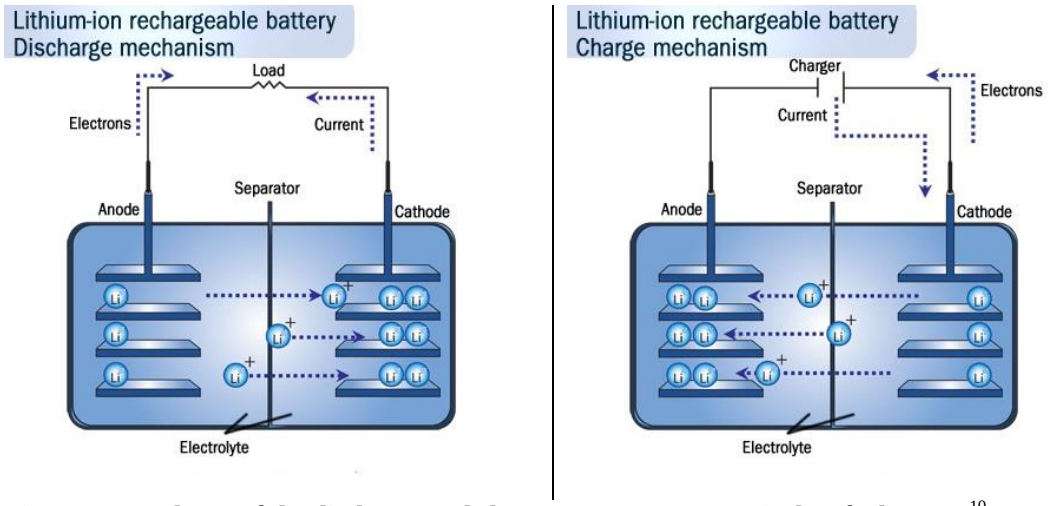

Figure 1.2 – Scheme of the discharge and charge processes, respectively, of a battery.[10]

It is considered an ideal battery, one that owns 100% of its nominal capacity, but due to the number of charges, discharges and incomplete charges, the total charge/discharge capacity of the battery tends to decrease, and sometimes one arrives at the end of battery life. To determine the battery capacity, one must apply a test to examine the capacity of the discharge process. Naturally, the discharge process is performed with the support of an external resistive charge.

For the common batteries, the discharge capacity is frequently expressed as a "C-rate". To calculate this capacity, it's measured the current delivered at a certain time, usually for the common batteries is 10 hours in the test, done by applying a charge rate of C/10, which means that the battery would return the full discharge within 10 hours.

So far, for all the batteries used nowadays, those presenting the higher potential for current applications are the Lithium-ion batteries which, as shown in the

Figure 1.3, are the smaller, lighter and with greater energy density among the most common batteries that we can find out on the market.

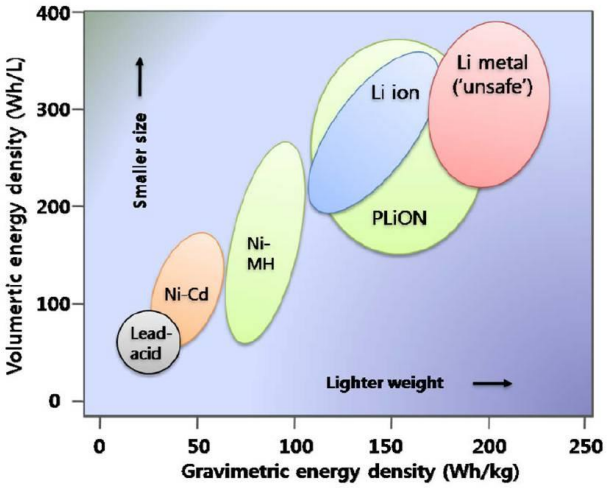

Figure 1.3 – Comparison of different technologies in terms of volumetric and gravimetric energy density.[6]

Currently, the Li-ion batteries are the most popular, in particular the secondary batteries, and they are found in the most variable portable devices like mobile-phones, laptops, music players, etc, due to their higher energy density storage capacity of all the currently existing rechargeable batteries. These characteristics justified the strong effort in their research and development, powered by the recent seeking of electricity storage devices for the important automobile industry.

The Lithium is the most electronegative metal in the Electrochemical Series ($E^0(Li^+/Li)$ = -3.2 V) and confers the greatest amount of electricity per unit weight among the elements. In addition to the high energy density of this type of battery, the high voltage, low self-discharge rate, low maintenance, and low toxicity are also some of the properties that make the Lithium-ion batteries so desirable and worth of the scientific world's attention.[11]

Usually this kind of batteries is, by far, lighter than other types of rechargeable batteries and this is due to the materials used in their manufacturing. The electrodes used to work as cathode and anode are made of lithium intercalation compounds and lithiated graphite, respectively. Commercialized in 1990 by Sony Energetic Inc., the basic architecture of this battery still remain and the Li_xCoO_2 is

still the material of choice to work as cathode, while the anode material started to be lithium metal until it was replaced by lithiated graphite, because of its high reactivity and flammability.

A great characteristic of these batteries is the absence of memory effect, i.e. there's no need for a complete discharge before recharging the battery, like in the other types of batteries, since it can endure for hundreds of discharge/charge processes.

Even though these batteries present a lot of advantages, they also have some disadvantages like their extreme sensitivity to high temperatures, which causes the degradation of the materials such as the cathode much faster than normal. If this happens the lithium-ion battery fails, overheats and sometimes catches fire. This is due to the chemical reactions between the electrolyte and the electrode materials because of the rise of the temperature of the cell.

Subsequently, safety became the major concern for the companies that commercialize these batteries, leading to a continued research work in the most problematic material of the battery, the cathode. Since then it was acquired a wealth of knowledge in terms of: synthesis techniques, reaction mechanisms, effect of particle size, interfaces, structural modifications, effect of doping, electrochemical and thermal stability, among others.

1.3. Materials to work as cathodes

Leaving aside the safety problem associated with the Li-ion batteries, the efficiency of the processes of discharge and charge of the battery tends to decrease.

As shown in Figure 1.4 during the discharge process, the Li^+ moves from the anode (graphite fully lithiated) to the cathode structure (Li_xCoO_2). While this happens, the electrons also move out of the anode to the cathode, and the transition metal (Co) is reduced until the cathode structure is fully lithiated. The reverse situation takes place during the charge process where both the Li^+ and the electrons move out of the cathode to the anode.[12]

It was already demonstrated that the alkali metal ions, such as Li^+, can move rapidly in an electronically conducting lattice containing transition metal atoms in a

mixed valence state, but charging a battery needs more energy than it is need to discharging it. This is due to the poor structure stabilization of the cathode material, in this case the Li_xCoO_2, in the discharge and charge processes.

Therefore, a material to work as cathode needs be an ionic and electronic conductor, i.e. have the capability of intercalate the lithium ion and the electrons without changing its structure. During both processes (discharge/charge) the cathode structure must be stable towards the electrolyte over the entire operating voltage range. The structure needs to be a compound that features low weight and high charge density to achieve high gravimetric and volumetric capacity for the battery, and must have a high quantity of sites for the Li^+ accommodation. Also the coupled diffusion of electrons must be fast enough to grant a good rate capability to achieve a high power battery

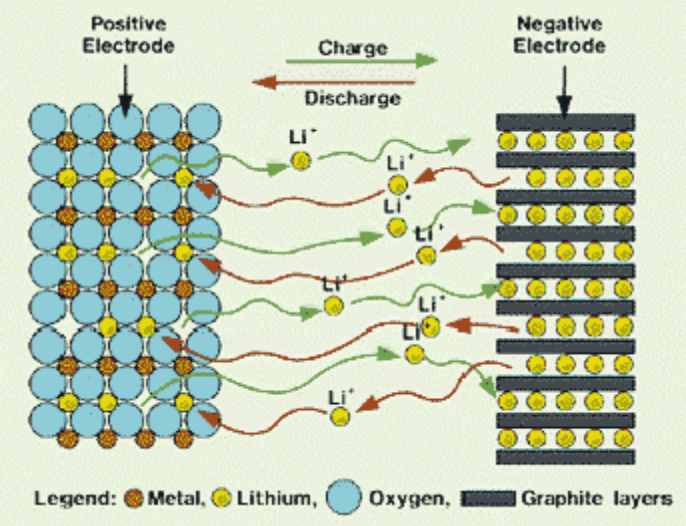

Figure 1.4 - Ionic flux during the discharge and charge processes of a battery.

Together with all of these characteristics, the cathode material must be ease to synthesize, cheap and non-toxic.

2. Objective

The aim of this work is centered in the synthesis and characterization of compound materials to work as cathodes for lithium-ion batteries, both organic and

inorganic in nature, performed respectively, in Portugal at the Interfacial Electrochemistry Group of Centro de Química e Bioquímica of the Faculdade de Ciências de Universidade de Lisboa and in Denmark in the Chemistry Department of the Aarhus University, within a protocol of ERASMUS programme.

The work with the compounds of organic nature was dedicated to the study of the properties of the conducting polymer Poly(3,4-ethylenedioxythiophene) doped with poly(styrene-4-sulfonate) (PEDOT-PSS) to achieve a stable and homogeneous polymer with aptness and ease of mass transfer of Li^+, during the charge/discharge processes of the polymeric matrix..

In what concerns the inorganic compounds, the objective was the development of a novel synthetic method for the preparation of the intercalation compound Li_2FeSiO_4. The idea was to explore a synthesis method that only used low cost precursors and simple equipment in order to minimize the cost of production to achieve a product that would reveal good electrochemical performance while being relatively inexpensive to produce.

3. Conducting Polymers

Nowadays the industry wants inexpensive and non-polluting conductors, which can be moulded into various shapes or made in the form of wires with high electrical conductivity, therefore encouraging the continued research for these materials.[13–16]

Conducting polymers are organic materials like plastics which can electronically conduct electricity. It is known that most of the organic polymers and plastics are generally electrical insulators but the conductive polymers are quite different. Conducting polymers have sequences containing alternating single and double bonds in their chains. While a single bond (or σ-bond) is strong and contains more located electrons, a π-bond contains weaker electrons and less localized. This means that the π-electrons can display greater mobility compared to σ-electrons because the combination result in the formation of an extended orbital. However, to allow the electronic conduction it is necessary that the electrons are removed (or added) from this orbits, with consequent formation of vacancies. If a second electron

moves to the vacancy, leaves behind a new vacancy that can be occupied by other electrons, therefore creating electronic conductivity. In the case of the conduction generated by removal of electrons by the polymer chain, the procedure is called "*p-doping*". The term "doping" arises from the fact that a dopant ion must be introduced in the matrix to preserve the electroneutrality. The dopant ion (retrieved from the electrolyte solution) accompanies the advance of the electronic charge across the polymer chains and should present a higher "apparent diffusion coefficient" within the polymer matrix. For a polymer displaying a high structural regularity, the processes of doping and un-doping are highly reversible, and then good candidates for rechargeable devices (e.g. secondary batteries, capacitors).The possibility of the molecular control of such materials allows that its conductivity can be adjusted so that these polymers exhibit behaviour ranging from insulators to metal-like conductors only by controlling the doping level.[17–23]

The reasons why poly(3,4-ethylenedioxythiophene) (PEDOT) has become a successful conductive polymer are its stability on the reduced and oxidised state, high conductivity and the availability as a polymer dispersion. In combination with poly(styrene-4-sulfonate) (PSS) as a counter-ion - Figure 3.1 – they form a stable dispersion, which is producible on an industrial scale and can be used in many deposition techniques. The PSS does not contribute directly to the charge transport, but acts as a template to keep PEDOT in the dispersed state and provides film-forming properties. The dissociated sulfonate groups balance the charges of the cationic PEDOT by forming a stable salt.[24–29]

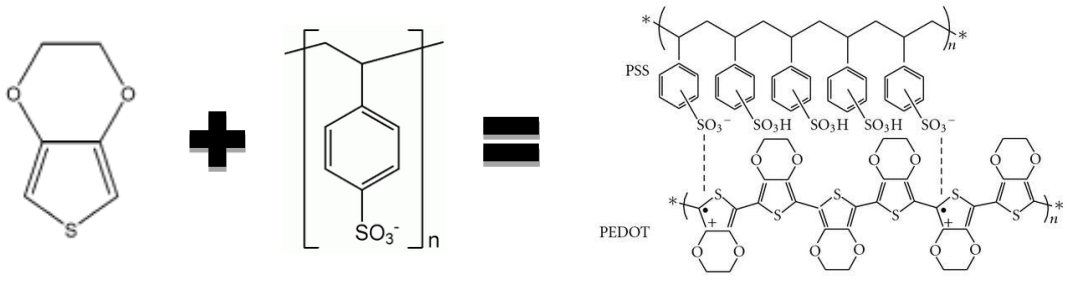

PEDOT PSS$^-$ PEDOT-PSS

Figure 3.1 - Schematic representation of the PEDOT-PSS films structure.

In a PEDOT-PSS film, being the positive charge of the oxidized polymer balanced by the negative sulfonate groups of the immobilized PSS, it is expected that the redox conversion of the polymer between its oxidized and neutral form is accompanied by a cation flux into and out of the polymeric matrix. This phenomenon is known as *pseudo-cationic doping* since the real dopant are the negative moieties of the PSS but the electroneutrality of the overall system is kept by the participation of the cations present in the electrolyte. If this contains Li^+ in its composition, it is therefore expected that the PEDOT-PSS films intakes Li^+ in discharge and releases those ions in oxidation, as required to be employed as cathodes in secondary Li-ion batteries.

3.1. Experimental procedures

3.1.1. Films Synthesis - Electropolymerization

The monomer EDOT was provided by Aldrich and used as received. Poly(sodium 4-styrenesulfonate) (NaPSS, average Mw~70,000) was obtained from Aldrich. Water Milli-Q was used to prepare all solutions.

Electrochemical polymerizations and measurements were performed by using a two-compartment, three-electrode electrochemical cell. A Pt solid disc electrode, with a diameter d=0.46 cm, have been used as working electrode. A large area Pt foil was used as counter electrode and a standard calomel electrode (SCE) as reference. The cell solutions were de-aerated by bubbling N_2 for 10 min prior to all electrochemical experiments, which were successively carried out under N_2 atmosphere at room temperature. Prior to all polymerizations, the Pt working electrodes were polished with 0.05 μm alumina powder and washed with millipore water.

The synthesis and deposition of PEDOT-PSS was carried out using cyclic voltammetry (CV_g) and galvanostatic (i_g) electrochemical polymerization from an aqueous solution containing 10mM EDOT monomer and 0.1 M of the NaPSS polyelectrolyte.

The potentiodynamic growth of PEDOT-PSS was recorded in a potential range between -0.7 and 0.8 V vs. SCE using a sweep rate of 50 $mV.s^{-1}$, as shown in Figure 3.2.

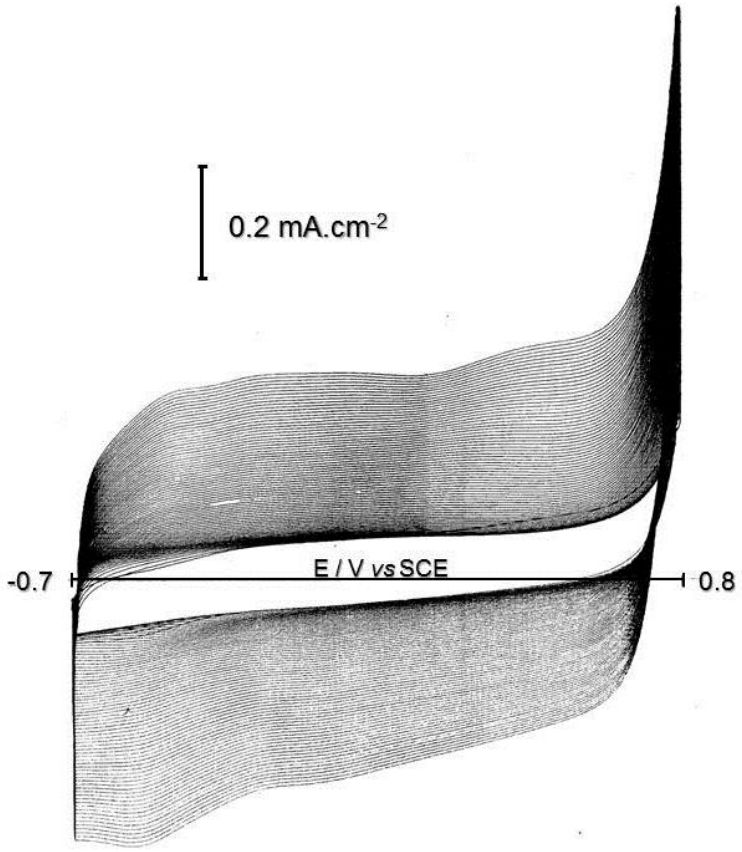

Figure 3.2 – Voltammograms of the potentiodynamic growth of PEDOT-PSS, in aqueous solution of 10 mM EDOT and 0.1 M NaPSS, from -0.7 V to 0.8 V at ν = 50 $mV.s^{-1}$, for 80 growth cycles.

The galvanostatic polymerization was achieved by applying a constant current of 0.033 mA (0.2 $mA.cm^{-2}$) for 275 seconds, i.e., with a polymerization charge of 9 mC (55 $mC.cm^{-2}$), as shown in Figure 3.3

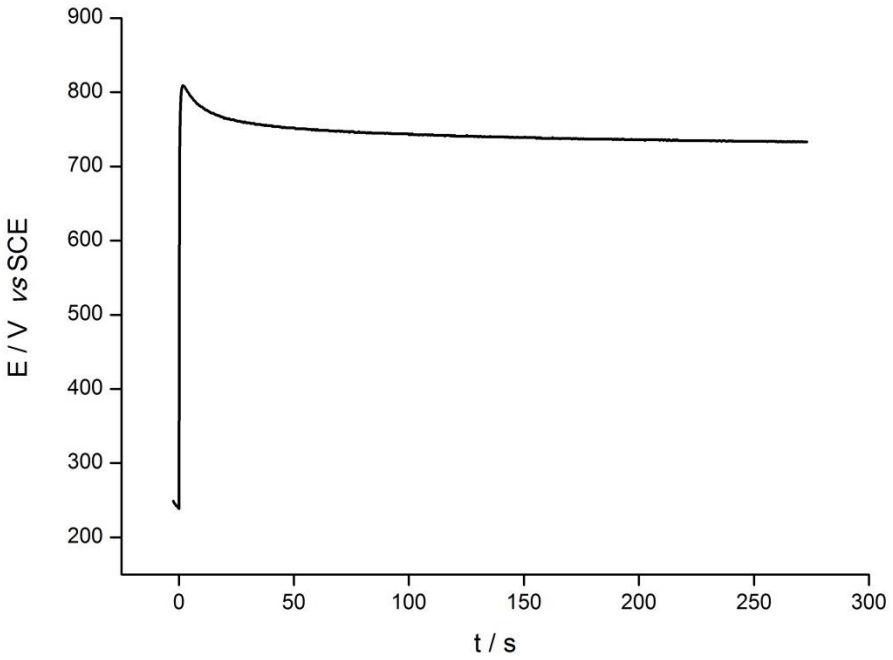

Figure 3.3 – Chronoamperogram of the galvanostatically grown of PEDOT-PSS, in aqueous solution of 10 mM EDOT and 0.1 M NaPSS, by a constant current density of i = 0.2 mA.cm^{-2}

3.1.2. Cyclic Voltammetry

Both linear-sweep voltammetry (LSV) and cyclic voltammetry (CV) are based on recording the current during a linear change of voltage at a stationary working electrode. The rate of change of voltage $\nu = dE/dt$ is relatively high, in the range 1-100 mV.s^{-1}. The difference is that in the case of CV the voltage is returned to the starting potential; CV is therefore also known as triangle sweep voltammetry.

Figure 3.4 compares the variation of voltage with time and the current response for the two methods.

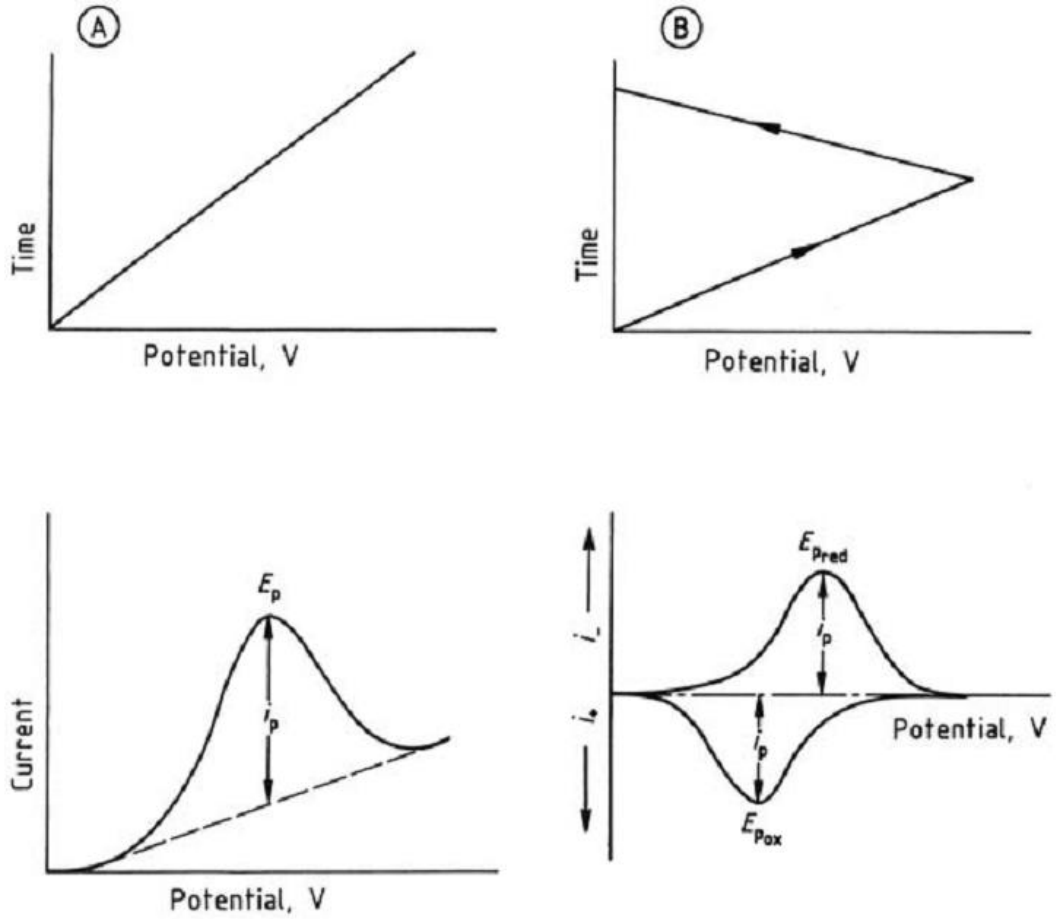

Figure 3.4 - Principle of linear sweep voltammetry (A) and cyclic voltammetry (B). Top. Variation of voltage with time; Bottom. Resulting current - potential curves. [30]

The peak currents, for both LSV and CV, are proportional to the analyte concentration:

$$i_p = kc_a v^{1/2} \qquad \text{Equation a}$$

and are influenced by the rate of change of voltage V. Cyclic voltammetry is mainly used for studying the reversibility of electrode processes and for kinetic observations, and only sometimes for analytical purposes. The voltage cycle illustrated in Figure 3.4 ensures that the reaction products formed at the potential E_{pred} on the cathodic path are reoxidized at E_{pox} in the anodic sweep.

For a reversible redox process:

$$\Delta E_p = E_{p_{red}} - E_{p_{ox}} = \frac{-57}{n}\ mV \qquad \text{Equation b}$$

the position of the current peak in this case being independent of the voltage scan rate. The two peaks have equal heights. With increasing irreversibility, ΔE_p becomes greater. For quasi-reversible processes and for a slow change of voltage, the difference is about (60/n) mV, but it becomes greater for a faster sweep. For totally irreversible processes, the reduction product is not reoxidized, so the anodic current peak is not seen.

If the reversible charge transfer is followed by a chemical reaction during which an electro-chemically active product is formed, a cyclic voltammogram of the type shown in Figure 3.5 can be obtained.

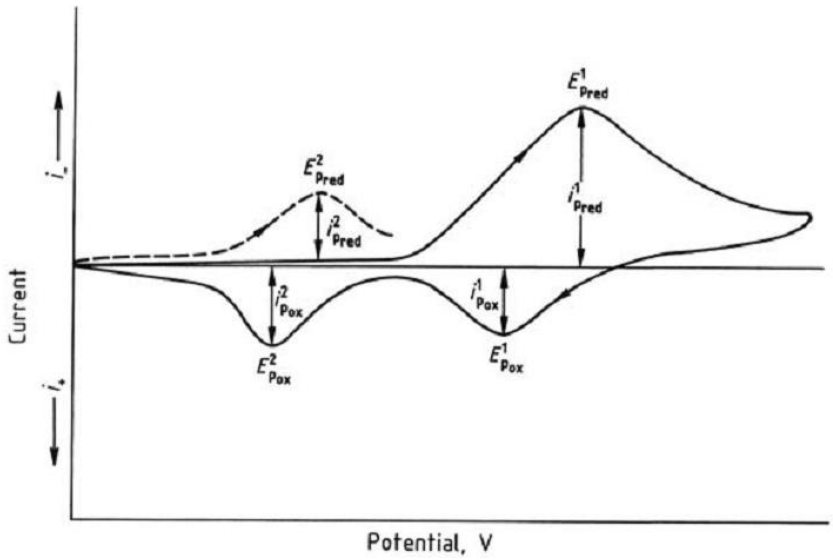

Figure 3.5 – Cyclic voltammogram of a reaction with reversible charge transfer and subsequent chemical. [30]

In the first sweep the two peaks E^1_{pred} and E^1_{pox} appear. The ratio of the peak heights is not, however, 1:1, as would be expected for a reversible process. Rather, E^1_{pox} is smaller than E^1_{pred} since part of the electrolysis product is chemically converted and therefore no longer available for reoxidation. Since the formed product is electrochemically active, a second peak E^2_{pox}, which corresponds to the oxidation of this product, appears in the complete anodic sweep. In the second sweep an additional cathodic peak E^2_{pred} which indicates the reduction of the previously oxidized compound, can also be recorded.[31,32]

Cyclic voltammetry gives information on the redox behaviour of electrochemically active species and on the kinetics of electrode reactions as well as offering the possibility of identifying reactive intermediates or subsequent products.

Cyclic voltammograms of the synthesized PEDOT-PSS were recorded in a potential range between -800 and 800 mV vs. SCE and between -900 and 1100 mV vs. SCE using a sweep rate of 50 $mV.s^{-1}$, in two different solutions of 0.1 M $LiClO_4$ in water and in acetonitrile, respectively.

3.1.3. Probe Beam Deflection

The probe beam deflection (PBD) technique is based on the deflection of a laser beam, aligned parallel to the electrode surface, caused by the concentration gradients evolving in front of the electrode during an electrochemical reaction Figure 3.6.

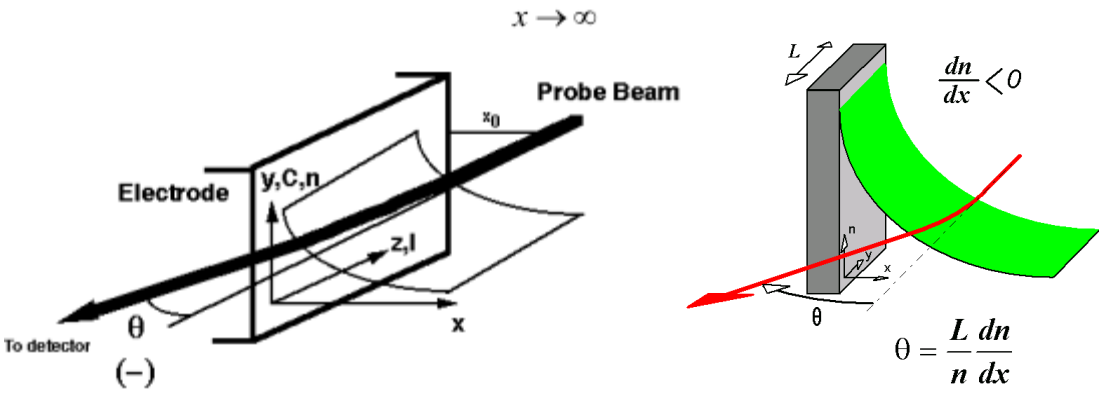

Figure 3.6 - Scheme of the deflection phenomena.[33]

The probe beam deflection (optical beam deflection or mirage effect) is caused by the change of refractive index in the diffusion region in front of the electrode|electrolyte interface.

The deflection of a laser beam aligned close (typically 100 – 200 μm) and parallel to the electrode surface is measured. The beam deflection (θ), considering

the concentration dependence of the refractive index, can be described by the following expression:

$$\theta(x,t) = \frac{L}{n}\sum_i \left(\frac{\delta n}{\delta c}\right)_i \frac{\delta c_i(x,t)}{\delta x} \qquad \text{Equation c}$$

where L is the electrode length (interaction path length), n is the refractive index of the electrolyte solution, $\left(\frac{\delta n}{\delta c}\right)_i$ is the derivative of the refractive index – concentration function related to the species i, and $\left(\frac{\delta c_i}{\delta x}\right)$ is the concentration gradient of the species i perpendicular to the electrode surface.

Due to the high sensitivity to follow the species fluxes towards and away from the electrode surface, the probe beam deflection technique is particularly useful to study redox coupled ion exchange in electroactive polymer or oxide films. It should be noted that this technique is "blind" to what concerns the exchange of solvent, since the concentration gradients created by the solvent intake or expulsion are too small to modify the local refractive index of the solution.

The diffusional delay, present in the experimental data, could be used to determine diffusion coefficients. The analysis of redox reactions in solution is quite complex. The distortion of the data, due to the diffusional delay, could be overcome by the use of sampling techniques (pulse chronodeflectometry) or data processing schemes (convolution or digital simulation). [33–40]

In this work a platinum disk (Ø = 5mm) Johnson-Matthey "Specpure" isolated with epoxy resin on a support of PTFE was employed as working electrode. Prior to the deposition of the polymer the electrode was mechanically polished to a mirror finish in aqueous suspensions of successively finer alumina (up to 0.05 μm).

The measurements were carried out by deflection analysis of the laser beam, caused by concentration gradients near the surface of the electrode, in aqueous solutions of $LiClO_4$ from -800 to 800 mV vs. SCE and acetonitrile solutions of the same salt from -900 to 1000 mV vs. SCE.

The mirage effect setup (Figure 3.7) includes a He-Ne of 2 mW (Oriel model 79200) with a diameter $1/e^2$ of 0.63 mm, assembled on a optic table. The beam is

focused on the centre of the cell through the quartz lenses, converging on a focal waist diameter of $1/e^2$ = 50 μm. A quartz cuvette (4.5 × 2 × 2 cm) with parallel windows placed perpendicular to the incident beam, was used as electrochemical cell. The counter-electrode was made of a platinum grid placed far enough from the Pt disk, ensuring that the transformations that occur therein do not affect the laser deflection caused by the processes that take place in the working electrode. The electrode potentials refer to saturated calomel electrode (SCE) which was placed in a separate compartment attached to the cell via a luggin capillary.

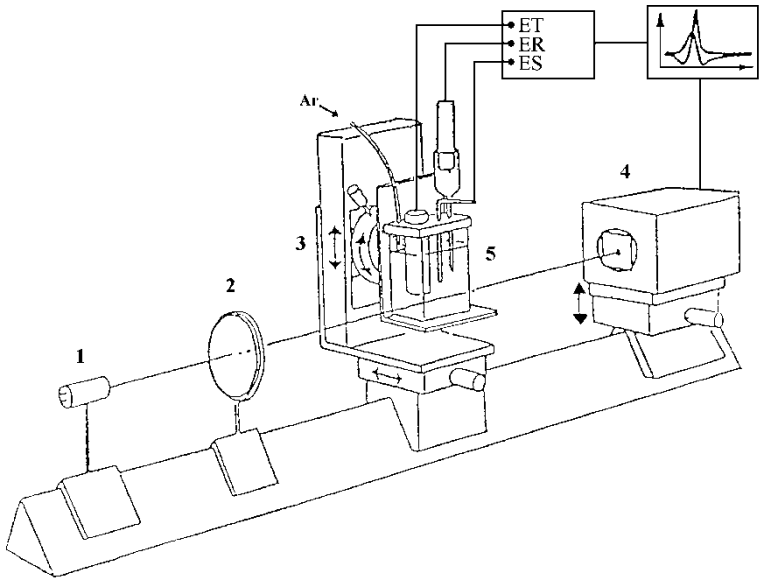

Figure 3.7 – Schematic illustration of the setting used in this work for the mirage effect measurements. 1.He-Ne laser (λ = 632.8 nm); 2.lens (60 mm focal length); 3.Motorized Microcontroller position; 4. Position detector (bifotodiode); 5.Electrochemical cell (quartz curvette).[34]

A motorized microcontrol system allows the positioning of the electrode surface with regard to the parallelism and distance from the laser beam. Under the experimental conditions used in this study, the electrode/laser minimum distance (x_0) was determined as 93 μm following a method proposed by *Vieil et al*.[34]. The working distance (x_0+x) used in all the experiments in this work was of 143 μm.

A positioning detector, consisting of a dual photodiode with 10 μm separation between active surfaces (Optilas spot-2DMI)), was placed 4.7 cm from the focal point.

The position sensor is connected to a differential amplifier, developed at the Faculdade de Ciências da Universidade de Lisboa, which allows to track the beam deflection with a nominal response 219 mV μm^{-1}, which results in a deflection response of 97 $\mu rad\ V^{-1}$. The whole system is mounted on a optical rail stand placed on a table. A more detailed description of the facility used lies in Figure 3.7.

This work considers a signal beam deviation in accordance with the usual convention. Therefore, an increase in the distance from the electrode laser (flow of species toward the electrode) gives rise to a positive θ signal, take the inverse and we will have a negative deflection.

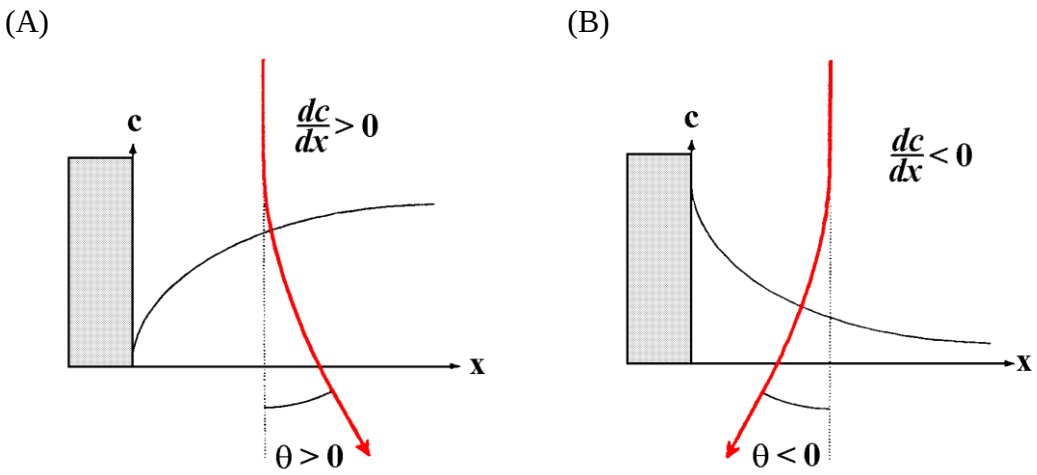

Figure 3.8 – Sign convections in PBD used in this work.[37]

3.1.4. Electrochemical Quartz Crystal Microbalance

The quartz crystal microbalance (QCM) is a well-established method for the measurement of small changes in mass in a surface, based on the relationship between changes in mass of materials attached to the quartz crystal and the oscillation frequency of the crystal. One more recent application of the QCM is its coupling with electrochemical measurements (EQCM) in order to measure mass changes associated with electrochemical processes such as adsorption, electrodeposition, corrosion, and equilibration of redox polymers undergoing charge transfer reactions.

The EQCM is based on the piezoelectric behaviour of a quartz crystal; that is, the deformation of the crystal in the presence of an electric field. An alternating electric field is applied between two metal electrodes (typically gold or platinum) deposited on opposite crystal faces (e.g., the two faces of a disk), which gives rise to an oscillation of the crystal parallel to these surfaces. The resonant frequency of this oscillation (f_0) is inversely related to the thickness of the quartz.

If the mass of the crystal increases (e.g., by deposition of material at the electrode surfaces), then the resonant frequency will also change. The relationship between the changes in mass per unit area (Δm) and frequency (Δf) are given by the Sauerbrey equation, which assumes that the combination of the crystal and deposited mass behaves as a rigid assembly:

$$\Delta f = \frac{-2\Delta m f_0^2}{A\sqrt{\mu_q \rho_q}} \qquad \text{Equation d}$$

Where A is the electrode surface area, μ_q the shear modulus of quartz, ρ_q the density of quartz.

The above relationship shows that, for example, an increase in mass leads to a decrease in frequency, and that the magnitude of the change in frequency is directly proportional to the mass change. This is the basis for quantitative measurements of mass changes using the QCM. Under our operating conditions, the Sauerbrey equation takes the simple form:

$$\Delta f(\text{Hz}) = -144.64\ \Delta m(\mu\text{g cm}^{-2})$$

Since electron transfer reactions of electroactive films are necessarily accompanied by charge transport in or out of the film (in order to maintain electroneutrality) and often by solvent transport and morphological changes, it is not uncommon for the density and/or viscosity of a polymer to vary significantly as a result of electron transfer reactions, leading to changes in the rigidity of the film. Hence, the rigidity of the film must be established for all the observed oxidation states.

The application of the QCM to mass changes occurring during electrochemical processes is conceptually very simple. The QCM electrode that is in

contact with the solution also serves as the working electrode in the electrochemical cell; that is, the adsorption, deposition, mass transport processes, etc., under investigation occur at this electrode. Until recently, the combination of the QCM and commercial potentiostats to make the electrochemical QCM (EQCM) has required some modification of the potentiostat electronics related to the grounding of the working electrode.[32,37,38,41,42,29,43–45]

The electrochemical gravimetric experiments were performed in a 420 model CH Instruments frequency analyser for electrochemical quartz crystal microbalance. The adsorption was carried out at room temperature onto a 8 MHz AT-cut quartz crystal coated with 1000 Å of Pt (0.2 cm^2) fitted in a one-compartment Teflon cell. A platinum wire and a saturated calomel electrode (SCE) were used as counter and reference electrodes, respectively.

3.1.5. Ellipsometry

Ellipsometry is a unique optical technique of great sensitivity for in situ non-destructive characterization of surface (inter-facial) phenomena (reactions) by measuring the change of the polarization state of a light-wave probe.

Although known for almost a century, the use of ellipsometry has increased rapidly in the last two decades. Among the most significant recent developments are new applications, novel and automated instrumentation and techniques for error-free data analysis.

Ellipsometry can be used to determine the dielectric properties of surfaces and thin films as well as the film thickness. If a linearly polarized light, of a known orientation, is specularly reflected from a surface, then the reflected light is elliptically polarized – Figure 3.9. The shape and orientation of the ellipse depend on the angle of incidence, the direction of the polarization of the incident light, and the dielectric properties of the surface. In the operation mode employed in this work, we can measure the polarization of the reflected light with a quarter-wave plate followed by the sample and the analyser; the orientations of the quarter-wave plate and the

analyser are varied until no light passes through the analyser. This mode is known by PCSA (Polarizer, Compensator, Sample, Analyser, in this sequence)

From these orientations and the direction of polarization of the incident light we can calculate the relative phase change, Δ and the relative amplitude change, ψ, introduced by reflection from the surface. ψ and Δ can give us the ratio between the s-polarized (E-field polarized perpendicular to the plane of incidence, $\vec{E}_s$) and p-polarized (E-field polarized parallel to the plane of incidence, $\vec{E}_p$) light reflected by the surface under study.

$$\frac{\hat{r}_p}{\hat{r}_s} = \tan\Psi \cdot e^{i\Delta} \qquad \text{Equation e}$$

where $\hat{r}_p$ and $\hat{r}_s$ are the Fresnel reflection coefficients (material dependent)

$$\hat{r}_p = \frac{\vec{E}_p^{ref}}{\vec{E}_p^{inc}} \quad ; \quad \hat{r}_s = \frac{\vec{E}_s^{ref}}{\vec{E}_s^{inc}} \qquad \text{Equation f}$$

An ellipsometer measures the changes in the polarization state of light when it is reflected from a sample. If the sample undergoes a change, for example a thin film on the surface changes its thickness, its reflection properties will also change. Measuring these changes in the reflection properties can allow us to deduce the actual change in the film thickness.

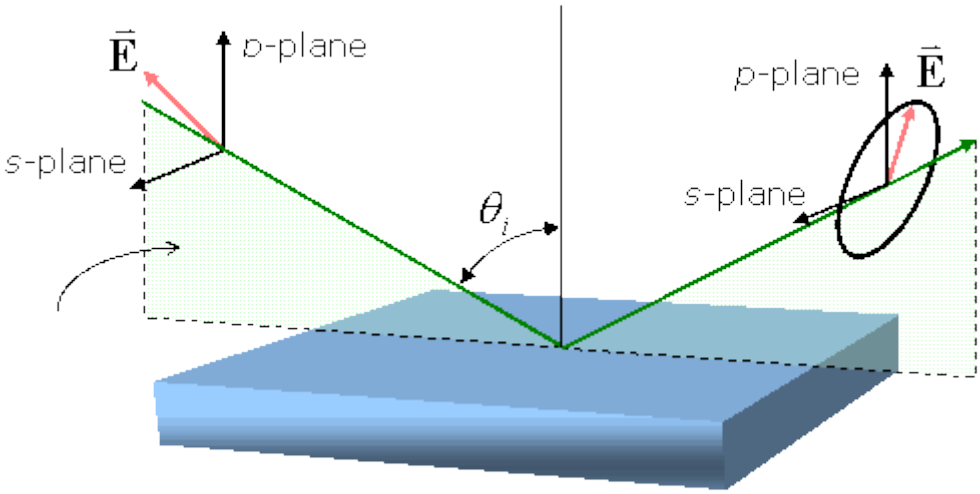

Figure 3.9 - Principle of ellipsometry measurements.

The most important application of ellipsometry is to study thin films. The sensitivity of an ellipsometer is such that a change on the film thickness of a few

Angstroms is usually easy to detect. This is what makes ellipsometry so powerful, one can measure film thickness, refractive index, and extinction coefficient of single films, layer stacks, and substrate materials with very high sensitivity. Rough surfaces, interfaces, material gradients, as well as mixtures of different materials can also be analyzed. Ellipsometry in the infrared provides an emerging powerful technique for the structural analysis of organic films.[31,32,46–48]

The refractive index of a film or a substrate material can be measured with a sensitivity better than 5×10^{-4}, which is the highest available value for non-invasive optical measuring methods, especially for thin films. The extinction coefficient can be measured with nearly the same sensitivity, which corresponds to a lower limit of 10–100 cm^{-1} for the absorption coefficient of the material.

The number of measurable layers of a stack is only limited by the optical contrast between the different layers. Further advantages of ellipsometry compared to other metrological methods are the non-invasive and non-destructive character of the optical method, the low energy input into the sample, the direct measurement of the dielectric function of bulk materials, and the ability to take measurements in any kind of optically transparent environment.

Film thickness and the complex refractive index (comprising the real part – often called simply *refractive index, n* – and the imaginary part - *extinction coefficient, k*) of the probed material can be determined either directly from Ψ and Δ (semi-infinite media or transparent materials) or by fitting procedures to a given model (optically absorbing thin films).

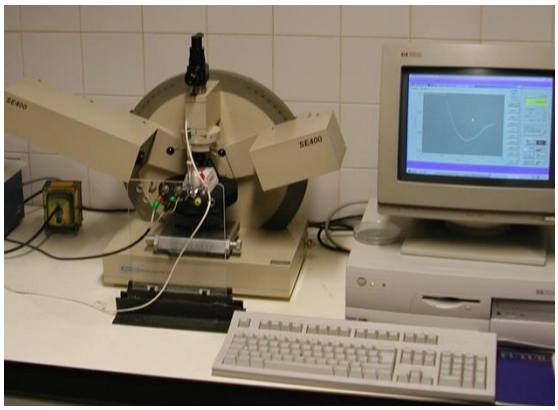

A

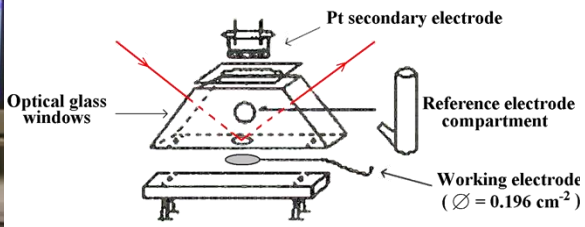

B

Figure 3.10 – a) Ellipsometer used in this work and b) scheme of the electro-optical cell employed for in-situ ellipsometric measurements.

A Sentech SE-400 ellipsometer was used operating with a λ = 632.8 nm (laser He-Ne) polarized light probe in PCSA mode – Figure 3.10 a). The resulting signal was collected by a microcomputer fitted with the SE-In-Situ software. The incident angle was of 70º and the polarization angle of 45º against the incident plane. A homemade three electrodes, two compartments electro-optical cell with two quartz windows facing the laser beam was used – Figure 3.10 b). The potential of a Pt disk working electrode with an exposed area of 0.196 cm^2 was controlled against the saturated calomel reference electrode through an EG&G model 273a potentiostat. A platinum grid was employed as secondary electrode.

3.2. Results and discussion

The films were synthesized as described in section 3.1.1 in aqueous media containing NaPSS. The redox characterization was performed by cyclic voltammetry at ν = 50 mV s^{-1} in aqueous or acetonitrile solutions of 0.1 M $LiClO_4$. Before the characterization in the organic medium the films were thoroughly rinsed with water and dried overnight in a sealed compartment packed with silica-gel, to eliminate all the water that could have been left after the synthesis.

3.2.1. Galvanostatically grown film in organic medium

The synthesis of PEDOT-PSS under galvanostatic control was accompanied by ellipsometry being the obtained data depicted in Figure 3.11.

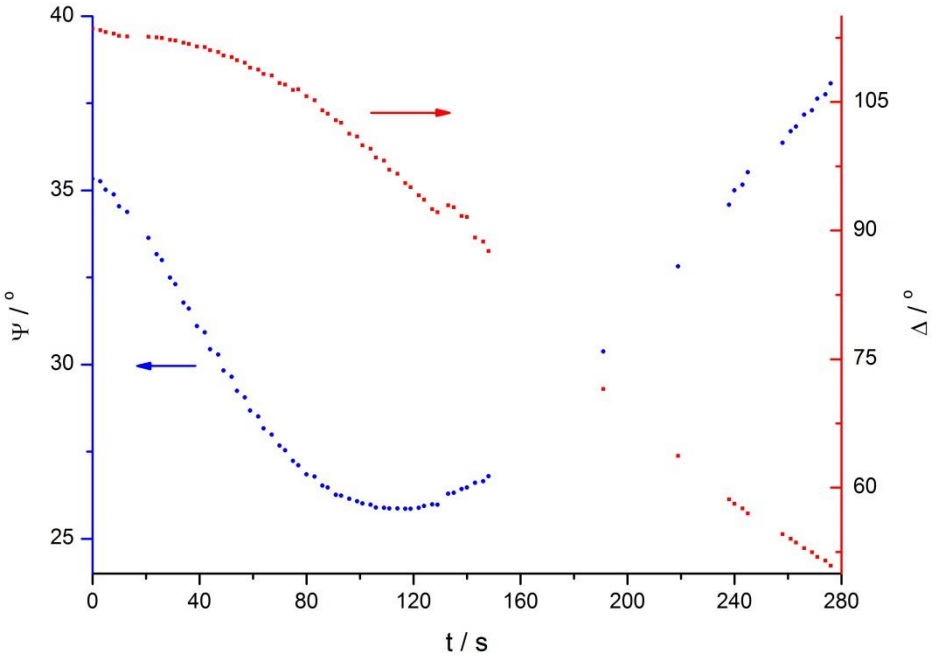

Figure 3.11 – Ellipsometric signals evolution during the galvanostatic synthesis of PEDOT-PSS at i=0.2 mA cm^{-2} in aqueous solution of 10 mM EDOT and 0.1 M NaPSS.

In order to estimate the film thickness and the optical properties of the film in the oxidized state, the common procedure [48] of fitting simulated data, computed for a model of homogeneous layers, to the experimental data was employed, being the result displayed in Figure 3.12. Despite the irregularity of the experimental data caused by the heterogeneity of the solution (emulsion like), it was possible to obtain a reasonable fit considering the formation of a film composed by 2 layers with refractive indices ñ = 1.277 - 0.09*i* (inner) and ñ = 1.210 – 0.20*i* (outer) with a total thickness of 203 nm (88 nm (inner) + 115 nm (outer layer)). These values reveal a more porous (lower refractive index) and more absorbing (higher extinction coefficient) outer layer than the inner one. For this particular polymer it is known that a higher value of k indicates a less conducting section of the material [47]. The global structural features revealed by this polymer are comparable to those found for the potentiostatically prepared PEDOT-ClO_4^- system [47] (ñ = 1.167 - 0.160*i* and ñ = 1.130 – 0.157*i* for the inner and outer layer respectively) despite the higher optical

density (refractive index) that should be ascribed to the presence of PSS in the polymeric matrix.

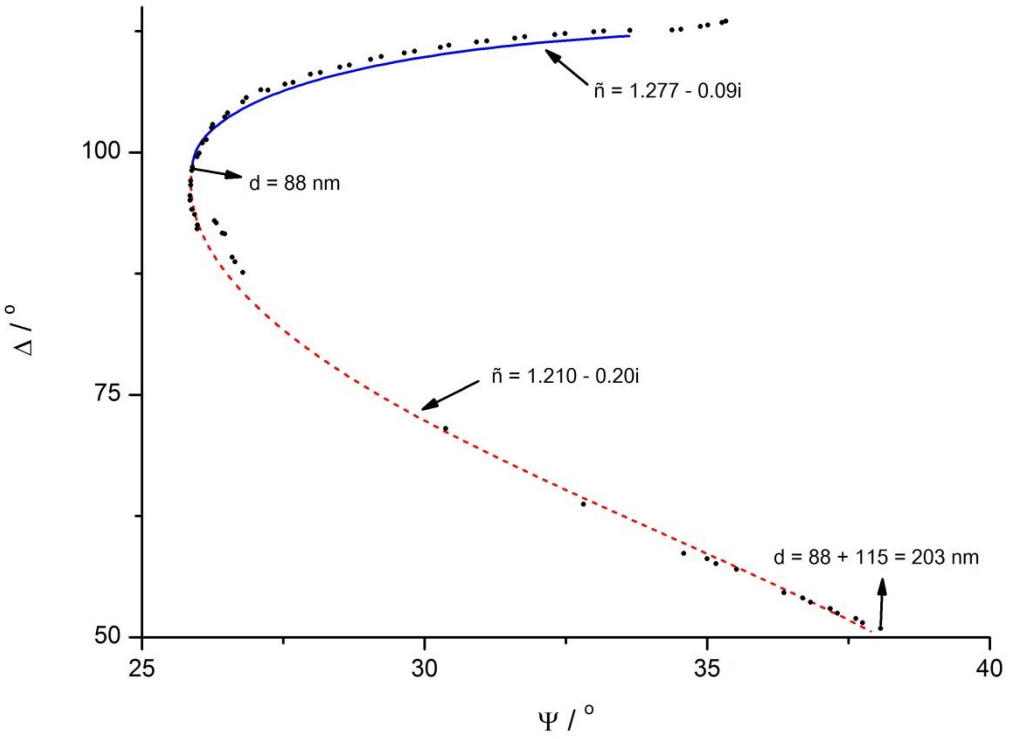

Figure 3.12 – Experimental ellipsometric data (circles) and simulated evolution of Ψ and Δ (lines) of a film composed by two homogeneous layers. Data recorded during the galvanostatic synthesis of PEDOT-PSS at i=0.2 mA cm^{-2} in aqueous solution of 10 mM EDOT and 0.1 M NaPSS.

The cyclic voltammogram of such modified electrode in $LiClO_4/CH_3CN$ solution is shown in Figure 3.13 and is similar to those reported elsewhere [29,44,45]. It is characterized by an oxidation wave centred at ≈ 0.2 V followed by a significant current increase at potential values beyond 0.9 V. Experiments (not shown here) with higher anodic limits (up to 1.4 V) did not revealed the formation of a current peak at potentials higher than 1.1 V but only a continuous increase of the current. Those experiments lead to the degradation of the polymer, revealed by the continuous decrease of its electroactivity in subsequent voltammetric cycles. In order to avoid the polymer overoxidation, the anodic scan limit was kept at values ≤1.1 V. In the

reverse scan the reduction of the polymer is characterized by an ill-defined broad reduction wave at ≈0.0 V followed by a marked reduction peak at -0.75 V.

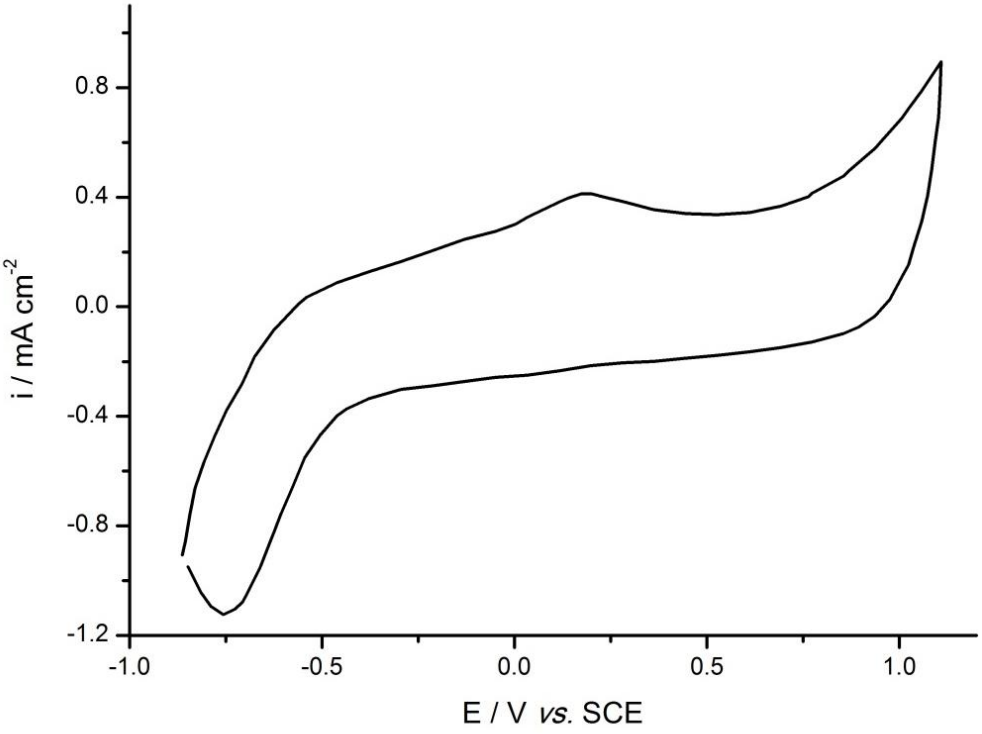

Figure 3.13 – Voltammogram (3rd cycle) of PEDOT-PSS, galvanostatically grown, in $LiClO_4/CH_3CN$, from -850 to 1100 mV at ν = 50 mV.s^{-1}.

In order to obtain relevant information about the mass fluxes taking place during the redox conversion of the PEDOT-PSS in this medium, the redox behaviour of the polymer was evaluated by microgravimetry. In Figure 3.14 is displayed the evolution of mass during a voltammetric cycle. The EQCM data surprisingly reveals a mass increase during the anodic scan with a slight inversion of tendency at the anodic limit, and release of mass in the cathodic sweep till the reduction peak at the more negative potentials start to develop. It should be noted that the mass incorporation in the film during the anodic potential scan takes place even at the more negative region of potentials although a more important increase begins at potentials close to that of the oxidation wave of the polymer. Other relevant aspect is that there is a net decrease of mass during a complete potential cycle, suggesting that some incorporated material in the polymer releases the matrix during the redox

conversion. This could be due to some PSS not effectively immobilized in the outer surface of the polymer that leave the modified electrode during the processes of expansion/contraction typical of the redox conversion of polymers. This observation is in good agreement with the optical data determined for this system that suggest a high amount of PSS in a porous outer layer.

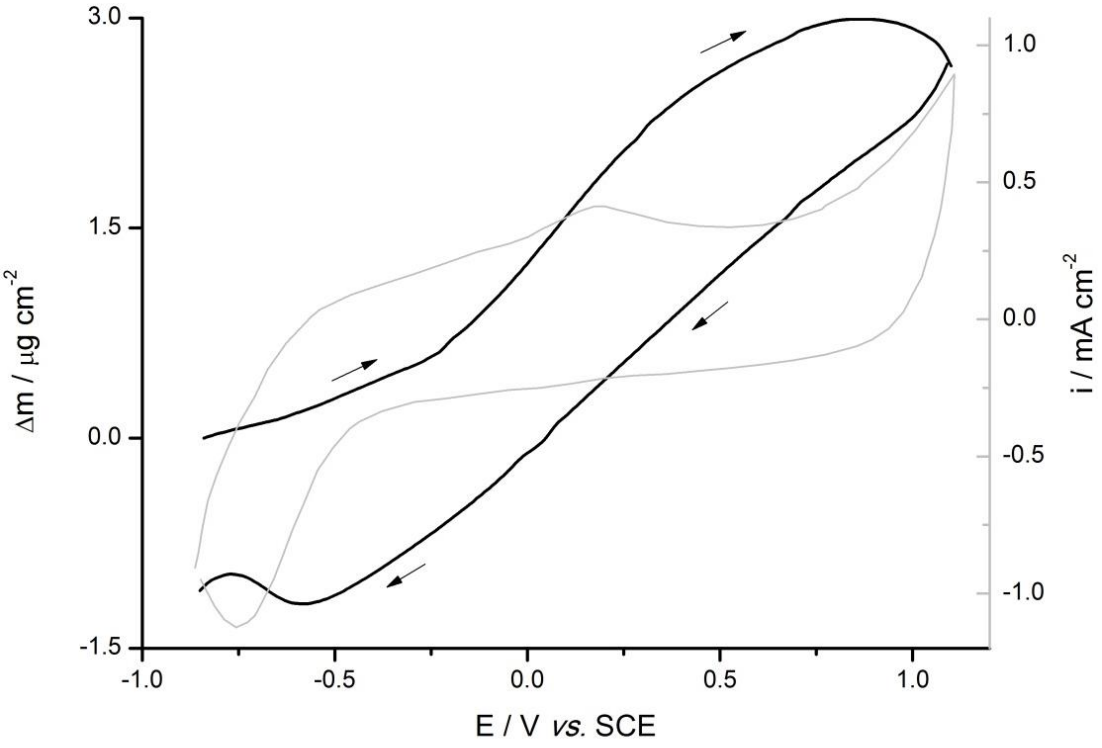

Figure 3.14 – Mass variations during the redox conversion of the galvanostatically grown PEDOT-PSS (3rd cycle) in $LiClO_4/CH_3CN$, from -850 to 1100 mV at ν = 50 $mV.s^{-1}$. In grey is shown the correspondent cycle voltammogram.

With the information collected by EQCM, one can imagine that the incorporation of perchlorate anions in oxidation and its expulsion on reduction should be the main fluxes associated to the polymer redox conversion. However, the possibility of solvent contribution for the observed mass changes must be taken into account to avoid erroneous interpretations. To evaluate the relative significance of the solvent for the mass variations, the redox conversion of the polymer was also studied by probe beam deflection which is non-sensitive to the solvent flux.

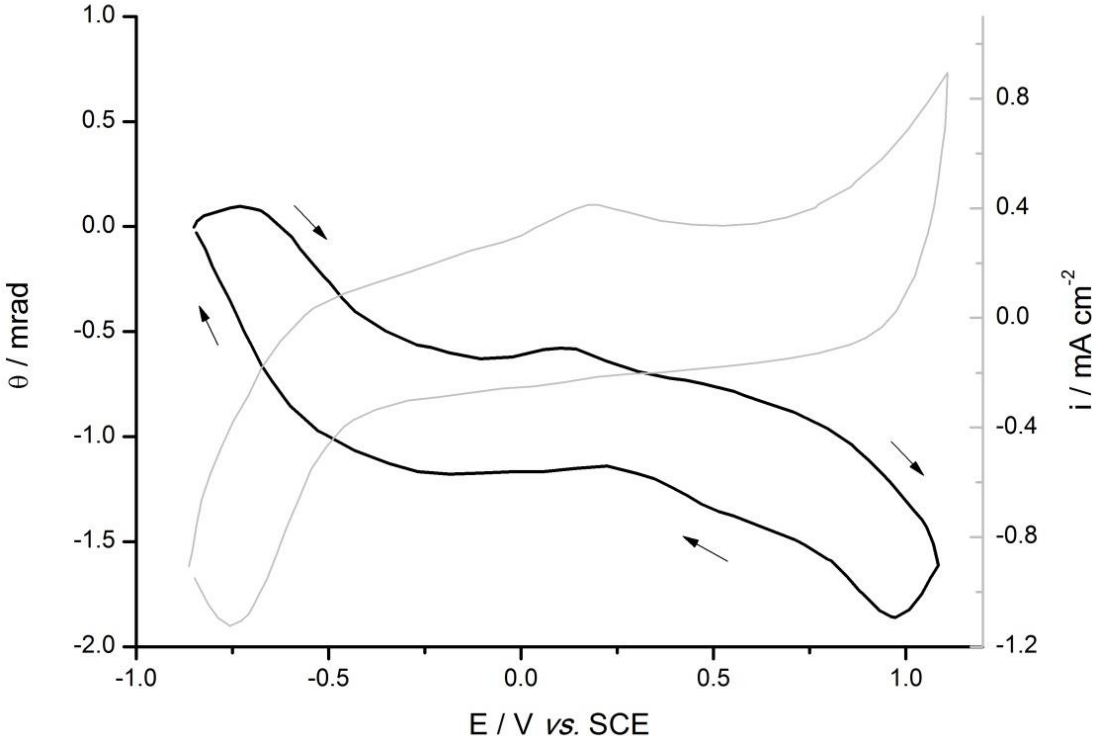

Figure 3.15 – Deflectogram (3rd cycle) of PEDOT-PSS, galvanostatically grown, in $LiClO_4/CH_3CN$, from -850 to 1100 mV at ν = 50 mV.s^{-1}. In grey is shown the correspondent cycle voltammogram.

As described in Section 3.1.3, according with the conventions used in this work, an increase of the measured value of θ means an intake of ionic species into the film, and an outtake when a decrease of this value is observed.

The deflectogram in Figure 3.15 shows a predominant expulsion of species in the anodic sweep and intake in the cathodic sweep. Such global features can only be explained by a pseudo-cationic doping of the polymer, involving mainly the Li^+ cation according with:

Anodic	$PEDOT^0\text{-}PSS^-,Li^+ \rightarrow PEDOT^+\text{-}PSS^- + Li^+_{(sol)}$
Cathodic	$PEDOT^+\text{-}PSS^- + Li^+_{(sol)} \rightarrow PEDOT^0\text{-}PSS^-,Li^+$

In the beginning of the anodic sweep there is a slight intake of species at the cathodic limit but this corresponds to the end of the reduction process from the

previous cycle, and is caused by the time delay in the electric and optical response of the system.

Still at the anodic sweep, a net intake of species at ≈ 0.2 V is observed. Since the oxidation of the polymer is taking place, and at this potential the polymer is already at the oxidised state ($PEDOT^+$-PSS^-), a cationic intake will not be plausible, so one can merely assume anions (ClO_4^-) incorporation. Is in this potential region that the polymer oxidation proceeds more intensively and the rate of expulsion of cations may be not enough to assure the electroneutrality, forcing the intake of anions into it. After this balance is achieved, the following ion transfer processes will be dominated by Li^+ cations discharge in the polymer.

At the beginning of the cathodic scan there is an apparent outtake of species but this is due to the time delay, already mentioned, between the electronic charge transfer and correspondent species optical detection. In fact, during the negative sweep and in the entire potential range, the ionic transfer is dominated by the Li^+ incorporation in the film, being the negative deflection eventually compensated by anion expulsion at potentials near the reduction wave of PEDOT at ≈0.0 V. It is known that this polymer suffer strong structural modifications in the potential region nearby 0 V [38] and, under those conditions, it is likely that the cation flux alone cannot maintain by itself the polymer electroneutrality, requiring the anion participation for the charge compensation process. Another explanation for the features observed at potentials close to 0V both in oxidation and reduction – entrance of species in the anodic scan and expulsion in the reverse sweep – may be the ingress and ejection of ionic pairs (electrolyte) associated to the swelling and shrinking of the polymer that occur in this potential range during its oxidation and reduction, respectively [47]. At more negative potentials, lower than -0.4V, a strong Li^+ incorporation in the film is clear, corresponding to the negative current peak in the voltammogram.

Also a relevant aspect to note is the fact that the net deflection at the beginning and end of the potential cycle have the same value which means that the ionic fluxes of the anodic and cathodic sweeps are practically reversible, which would be the optimum behaviour of the polymer to be used in a battery.

3.2.2. Potentiodynamically grown film in organic medium

Films of PEDOT-PSS synthesized under potentiodynamic control were characterized by cyclic voltammetry, being the voltammogram of the modified electrode in $LiClO_4/CH_3CN$ solution illustrated in Figure 3.16. It is also characterized by an oxidation wave centred at ≈ 0.2 V followed by a significant current increase until it reaches the anodic potential limit. In the cathodic scan the reduction of the polymer is characterized by an ill-defined broad reduction wave at ≈0.0 V followed by a marked reduction peak at -0.65 V. Despite the similar redox behaviour as the galvanostatically grown film, this polymer presents a lower overpotential for the reduction process at the more negative potential values, revealing a structurally better organized system as it should be expected for a potentiodynamically grown film.

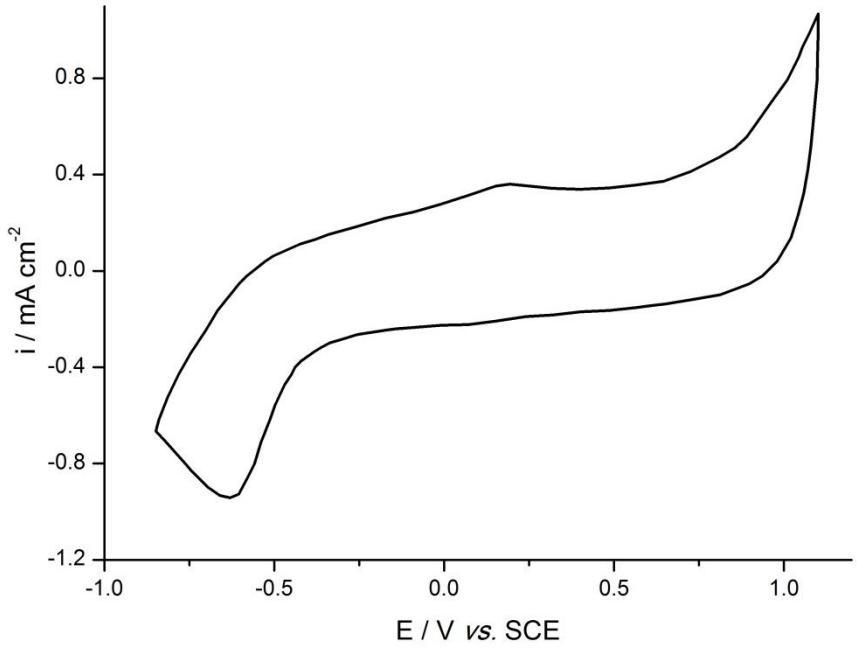

Figure 3.16 - Voltammogram (3rd cycle) of PEDOT-PSS, potentiodynamically grown, in $LiClO_4/CH_3CN$, from -850 to 1100 mV at ν = 50 mV.s^{-1}.

The EQCM data shown in Figure 3.17 also exposes a mass increase during the anodic sweep with a minor mass loss at the anodic limit, and a continuous mass loss throughout the cathodic sweep until it reaches the reduction peak and, after it, mass incorporation takes place at the more negative potentials. Again, the mass

integration in the film during the anodic sweep takes place even at the more negative region of potentials although a more important increase begins at potentials close to that of the oxidation wave of the polymer (as seen before in Figure 3.14). With this type of polymer there is a slight gain of mass after a complete potential cycle, indicating this net uptake of mass inside the film, that the structure equilibrium of the polymer in this solution was not yet reached.

Moreover, in this type of polymer the magnitude of the mass fluxes in a complete cycle is smaller than the one in the galvanostatically grown polymer suggesting, as expected, that this type of polymer is less porous than the galvanostatically grown one.

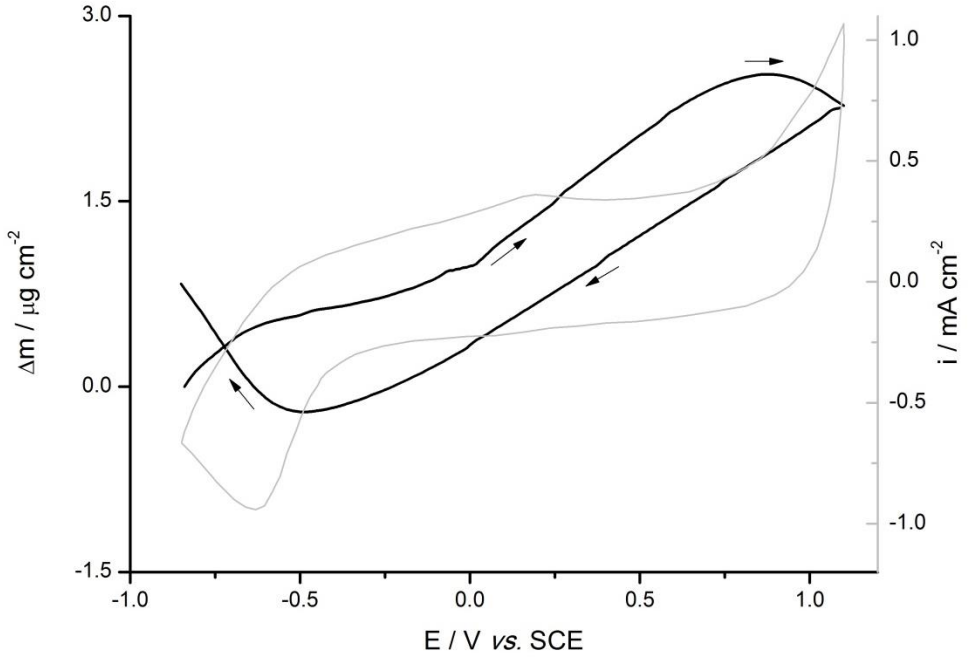

Figure 3.17 – Mass variations during the redox conversion of the potentiodynamically grown PEDOT-PSS (3rd cycle) in $LiClO_4/CH_3CN$, from -850 to 1100 mV at ν = 50 $mV.s^{-1}$. In grey is shown the correspondent cycle voltammogram.

Notwithstanding the mass intake during polymer oxidation, the data gathered during the PBD experiments revealed that the ionic flux is dominated by Li^+ ions expulsion during the entire anodic scan, as depicted in Figure 3.18. In fact, after the slight positive deflection at the beginning of the experiment due to the PBD time delay, a continuous outtake of species goes until the conclusion of the scan. It should be noted that at the potential of the oxidation wave of the PEDOT-PSS at ≈ 0.2 V,

this outtake of species gets smaller, giving reason to believe that a slightly incorporation of species takes place, likely due to the incorporation of electrolyte during polymer swelling.

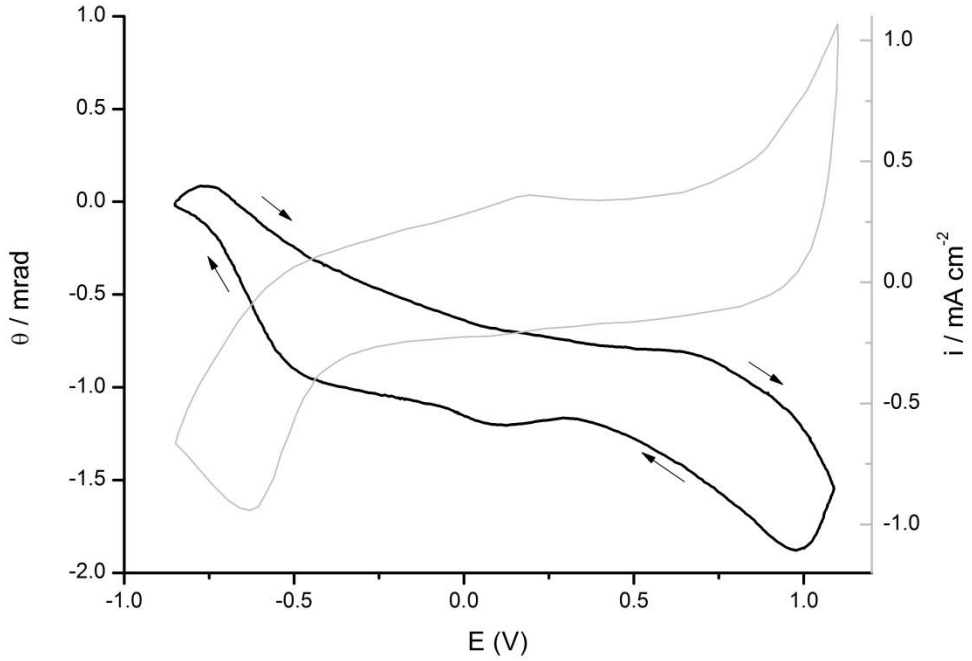

Figure 3.18 - Deflectogram (3rd cycle) of PEDOT-PSS, potentiodynamically grown, in $LiClO_4/CH_3CN$, from -850 to 1100 mV at ν = 50 mV.s^{-1}. In grey is shown the correspondent cycle voltammogram.

In the cathodic scan there is again, like in Figure 3.15, an apparent discharge of species in the anodic limit, for the same reason as mentioned before, followed by a continuous incorporation of species until the conclusion of this scan, eventually compensated by the expulsion of ionic pairs at ≈ 0.0 V, concomitant with the polymer shrinkage. For more negative potentials, namely E< -0.4V, an intense incorporation of cations is observed being this the main ion flux involved in the charge compensation correspondent to the reduction of the polymer in this potential region. A reported elsewhere [47], the PEDOT reduction proceeds by two successive stages (two reduction waves), being the electrochemical reaction precisely the same; the reason that originates the two consecutive reduction phases is purely mechanic and is related with the polymer shrinkage. As the polymer start to reduce, there is a deep contraction of its structure rendering difficult the counterion flux, almost ceasing the process; for the complete reduction of the film, high cathodic

overpotentials are required and a second reduction peak appears at rather high negative potential values. As indicated by the optical parameters of the PEDOT-PSS, this film is rather compact (compared to the non-PSS doped film [47]) and then, the first reduction wave (where the polymer shrinking happens) is poorly noticed, being the reduction mainly accomplished at quite negative potentials. Being the electrochemical process in the two reduction events the same, and since the PBD data clearly indicates that at E<-0.4V the ionic flux associated with the polymer reduction is dominated by Li^+ intake, the same type of flux should be involved in the first reduction wave, regardless this process is masked by the electrolyte expelling.

Despite the likely different compactness of the galvanostatically and potentiodynamically synthesized films, the extent of ion transfer is approximately the same in both polymers, as evidenced by the similar magnitude of deflection recorded in the two systems (Figure 3.15 and Figure 3.18). However, the potentiodynamically grown PEDOT-PSS is more adherent to the platinum electrode and, since both films presented similar electrochemical properties (Figure 3.13 and Figure 3.16), the following studies were performed with the films potentiodynamically prepared.

Since it was observed an intense cation expulsion in polymer oxidation at high positive potential values, the anodic limit was decreased to 0.9V, - Figure 3.19 - in order to appraise if it affects the Li^+ incorporation in reduction at high negative potential values.

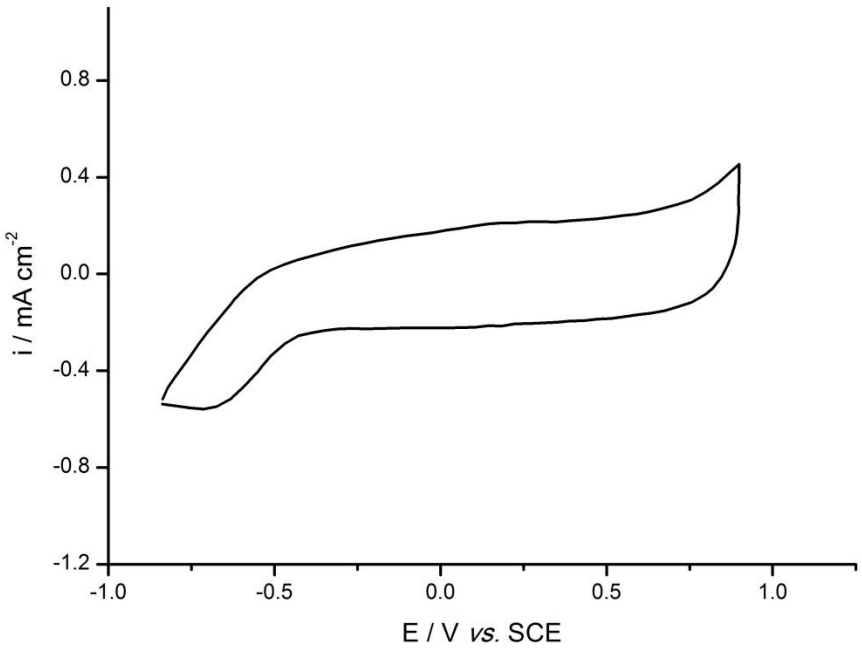

Figure 3.19 - Voltammogram (3rd cycle) of PEDOT-PSS, potentiodynamically grown, in $LiClO_4/CH_3CN$, from -850 to 900 mV at ν = 50 mV.s^{-1}.

By lowering the anodic limit, the peak potentials of oxidation and reduction of the PEDOT-PSS remain the same as in the later voltammogram (Figure 3.16), but the oxidation and reduction currents of the PEDOT-PSS decreased.

The decrease of exchanged charge means that less polymer is converted, hence less electrons transferred and then less Li^+ involved in the redox process. Of course, in an application of such conducting polymer as cathode in a battery, higher potentials should be used to charge the PEDOT-PSS (e.g. 1.1V) in order to optimize the charge capacity of the device.

As expected, the EQCM data in Figure 3.20 show a similar, although slightly smaller mass variation than in Figure 3.17.

Similar tendencies are also found in the PBD studies - Figure 3.21 – compared to the deflectogram presented in Figure 3.18. The main difference resides in the extent of ion transfer that is decreased by lowering the anodic potential limit. This experiment shows that a significant amount of Li+ ions remains incorporated in the film during the conversion of the polymer since during each cycle the potential is not high enough to expel them. For a good performance of PEDOT-PSS in a Li-ion battery, a higher potential must be applied to the polymer in order to charge it since -

0.9 V is not high enough to eject a significant amount of lithium ions from the polymer matrix.

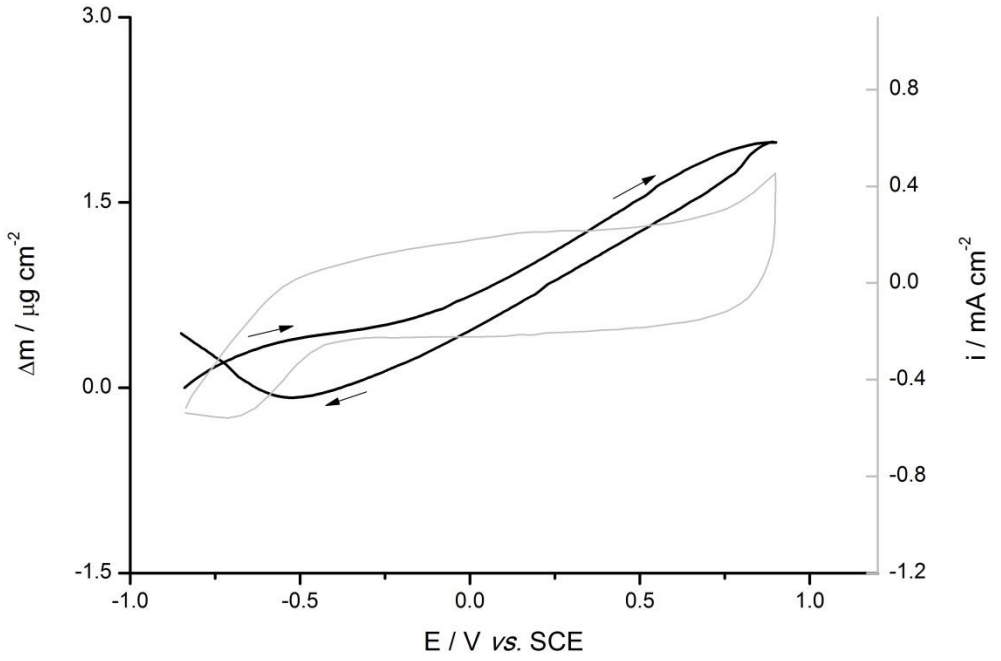

Figure 3.20 - Mass variations during the redox conversion of the potentiodynamically grown PEDOT-PSS (3rd cycle) in $LiClO_4/CH_3CN$, from -850 to 900 mV at ν = 50 mV.s^{-1}. In grey is shown the correspondent cycle voltammogram.

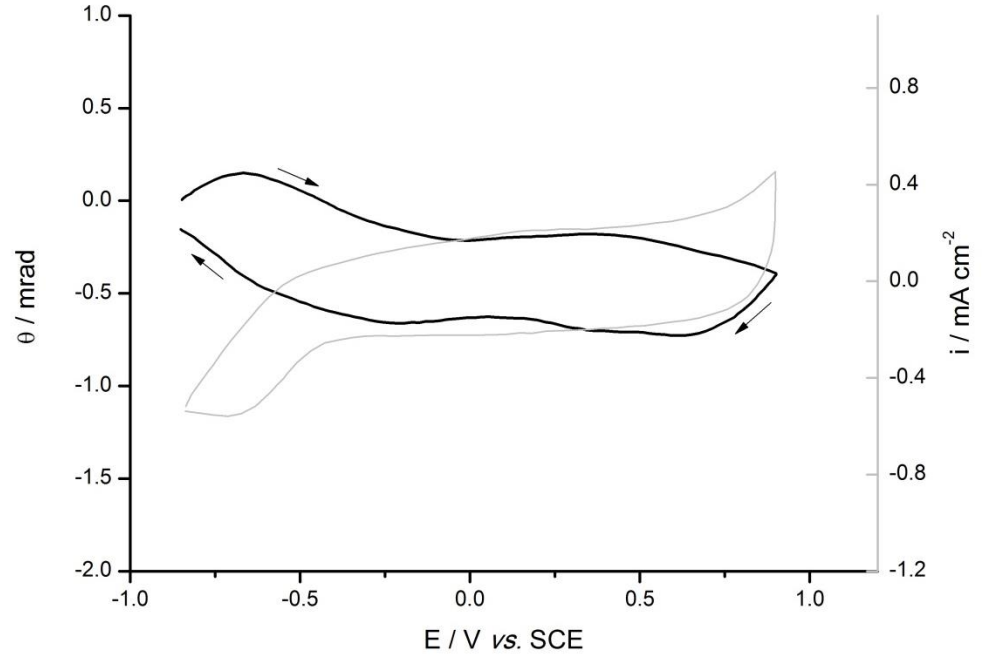

Figure 3.21 - Deflectogram (3rd cycle) of PEDOT-PSS, potentiodynamically grown, in $LiClO_4/CH_3CN$, from -850 to 900 mV at ν = 50 mV.s^{-1}. In grey is shown the correspondent cycle voltammogram.

The redox behaviour of a PEDOT-PSS film recorded during a potential cycle starting from the open circuit potential is shown in Figure 3.22. Since the film was not completely reduced prior the experiment, the voltammogram displays initially a negative current corresponding to the undoping of the polymer, but the other redox features are similar to those already shown for continuously cycled films in the same potential limits. Notwithstanding the magnitude of the oxidation and reduction peaks are slightly higher than those observed in the voltammogram in Figure 3.19, suggesting that more active sites are available for redox conversion since the polymer didn't suffer the packing effect caused by electric discharge or continuous potential cycling. Also the mass variation during the voltammetric experiment, shown in Figure 3.23, exhibits the same general features as in the Figure 3.20, being the mass exchange during the potential cycle somewhat higher than observed for the polymer under continuous cycling.

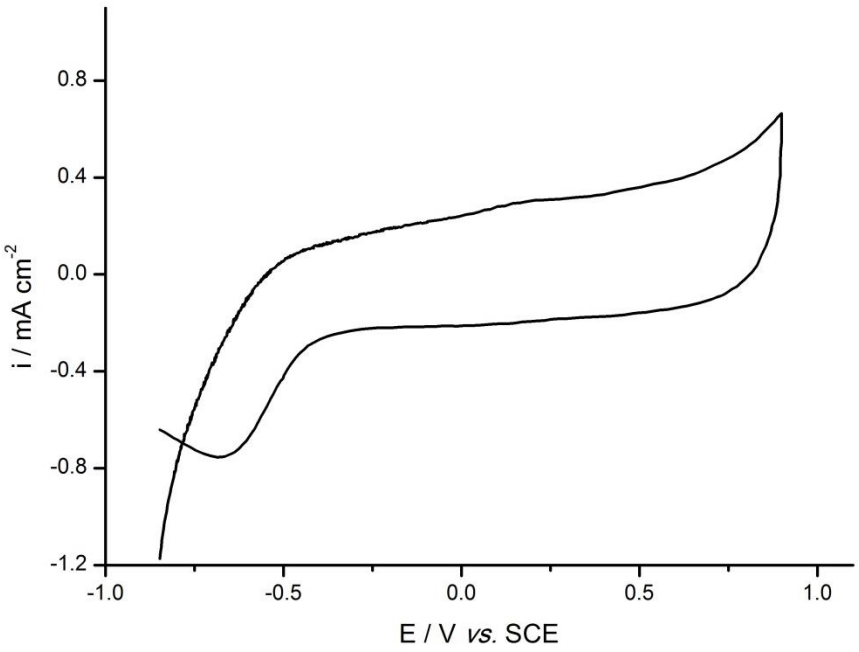

Figure 3.22 - Voltammogram (1st cycle) of PEDOT-PSS, potentiodynamically grown, in $LiClO_4/CH_3CN$, after being at open circuit potential, from -850 to 900 mV at v = 50 $mV.s^{-1}$.

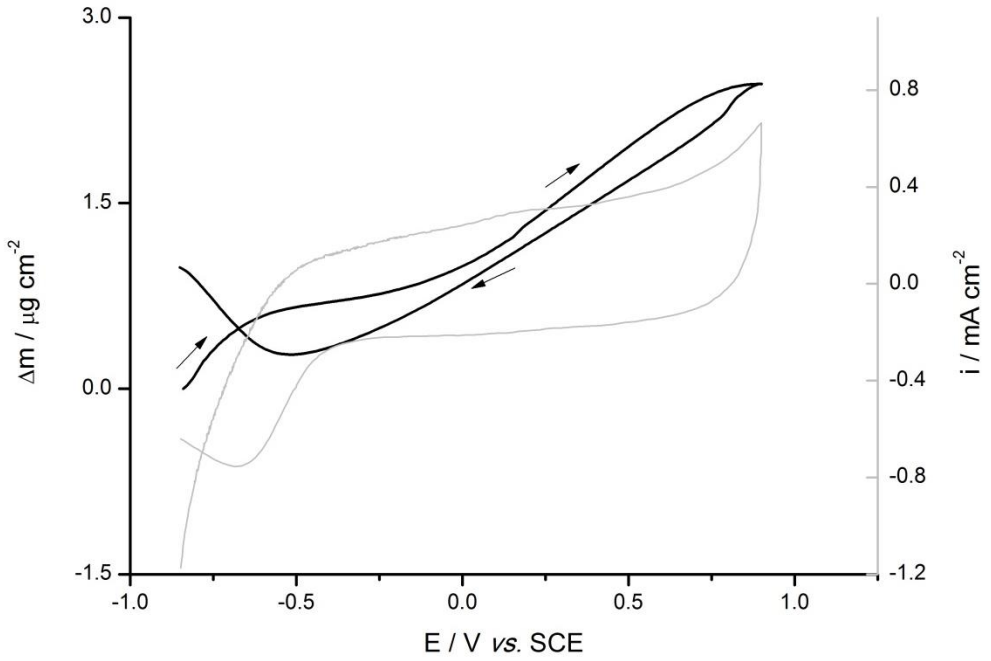

Figure 3.23 - Mass variations during the redox conversion of the potentiodynamically grown PEDOT-PSS (1st cycle) in $LiClO_4/CH_3CN$, after being at open circuit potential, from -850 to 900 mV at ν = 50 mV.s^{-1}. In grey is shown the correspondent cycle voltammogram.

The PBD data presented in Figure 3.24 reveals characteristics similar to the other deflectograms, being the main difference a strong positive signal corresponding to the intake of Li^+ at the beginning of the anodic potential scan. This process is caused by the reduction of the polymer at such negative potentials (the modified electrode was on open circuit potential prior the voltammogram has started) and the incorporation of cations is so intense that, even for a light cation such as Li^+, the initial mass increase can be noticed in the EQCM experiment shown in Figure 3.23. The other PBD features are similar to those reported for the film under continuous cycling but the extent of ionic transfer is higher than observed on that experiment, as it was expected by the same tendency verified in the voltammogram.

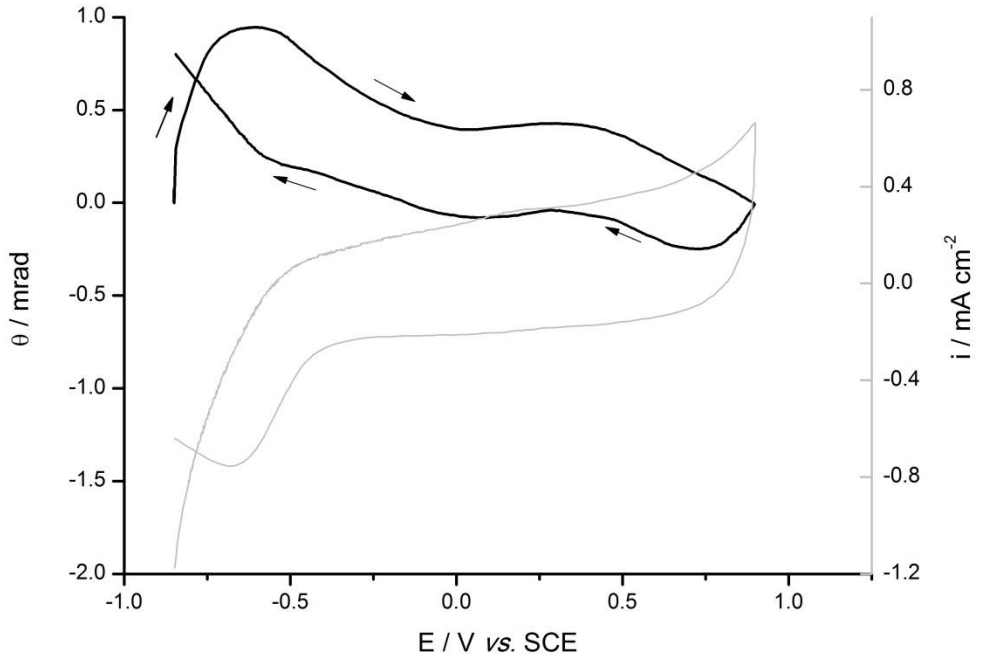

Figure 3.24 - Deflectogram (1st cycle) of PEDOT-PSS, potentiodynamically grown, in $LiClO_4/CH_3CN$, after being at open circuit potential, from -850 to 900 mV at ν = 50 $mV.s^{-1}$. In grey is shown the correspondent cycle voltammogram.

To appraise the effect that the complete discharge of the polymer (high amount of incorporated Li^+) have in its redox behaviour and in particular on the ionic fluxes in the potential window of the experiment, the modified electrode was discharged by applying -0.85 V for 20 seconds prior its voltammetric characterization, being the recorded voltammogram shown in Figure 3.25. The redox behaviour is characterized by an oxidation peak at ≈ 0.35 V, a broad reduction wave centred at ≈ 0.2 V and a reduction peak at ≈-0.7 V. As it is typical on conducting polymers, the oxidation peak occurs at a higher potential value than observed in the case of a non-discharged film (Figure 3.22 (≈0.20 V)) as due to the fact that the polymer was fully reduced at the beginning of the potential scan and so, a higher overpotential is required to oxidise it. However, since more active sites were reduced, the extension of the oxidation is higher and the anodic current peak is more intense than in the previous experiments (Figure 3.19 and Figure 3.22). The polymer reduction is particularly evident at rather negative potential values but the current peak at ≈-0.7 V is less intense than those monitored in the previous experiments, suggesting that the forced discharge of the polymer (with concomitant Li^+

incorporation) promoted a high compactness degree of the polymer which makes difficult the ion exchange process.

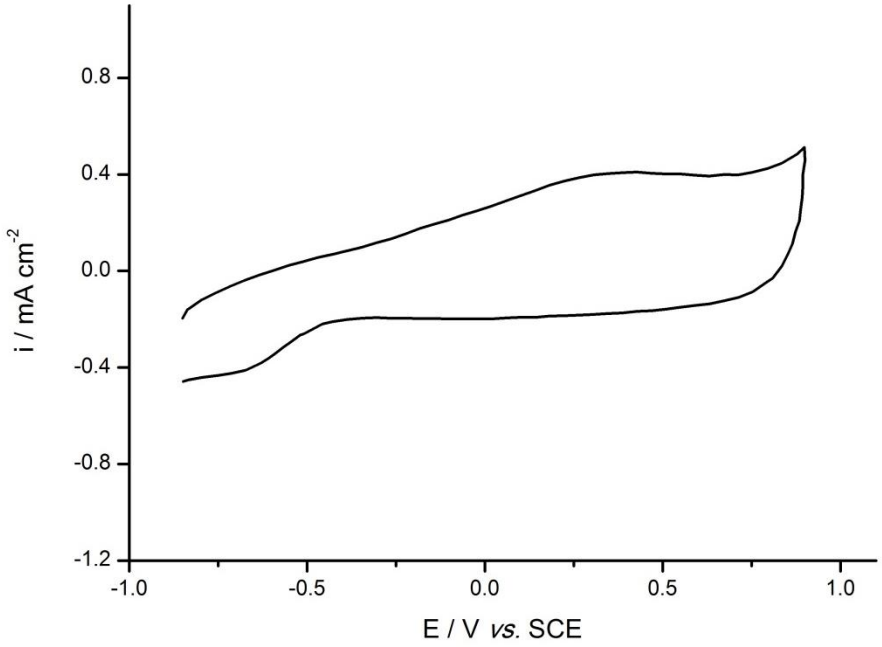

Figure 3.25 – Voltammogram (1st cycle) of PEDOT-PSS, potentiodynamically grown, in $LiClO_4/CH_3CN$, after 20 seconds of discharge, from -850 to 1100 mV at v = 50 mV.s^{-1}.

The EQCM data in Figure 3.26 support the postulated above, given that the mass variation in a full potential cycle is very small; being the mass increase in the film on oxidation mainly ascribed to the intake of solvent (and electrolyte), a smaller magnitude of mass change must be associated to a more compact film that exhibits to some extent a difficulty in carry out the typical structural changes of the polymer. These film characteristics are also reflected by the PBD analysis of such film, depicted in Figure 3.27. As expected, the deflectogram shows that throughout the anodic sweep the outtake of cations is significantly small, until it reaches the potential region of the oxidation wave of the polymer, where there is the incorporation of a significantly amount of species preceding it the outtake of Li^+, evident for E>0.5 V. Under these conditions is not clear if the counterion flux is dominated by the cation expulsion, or if the anion can enter as a dopant ion. Actually, a deep reduction of the film like the one that was carried out by keeping the modified electrode at -0.85 V for 20 seconds, may confine a large amount of Li^+

counterions deeply in the film, inhibiting its diffusion across the polymer to participate in the ionic transfer, due to a high compactness degree attained.

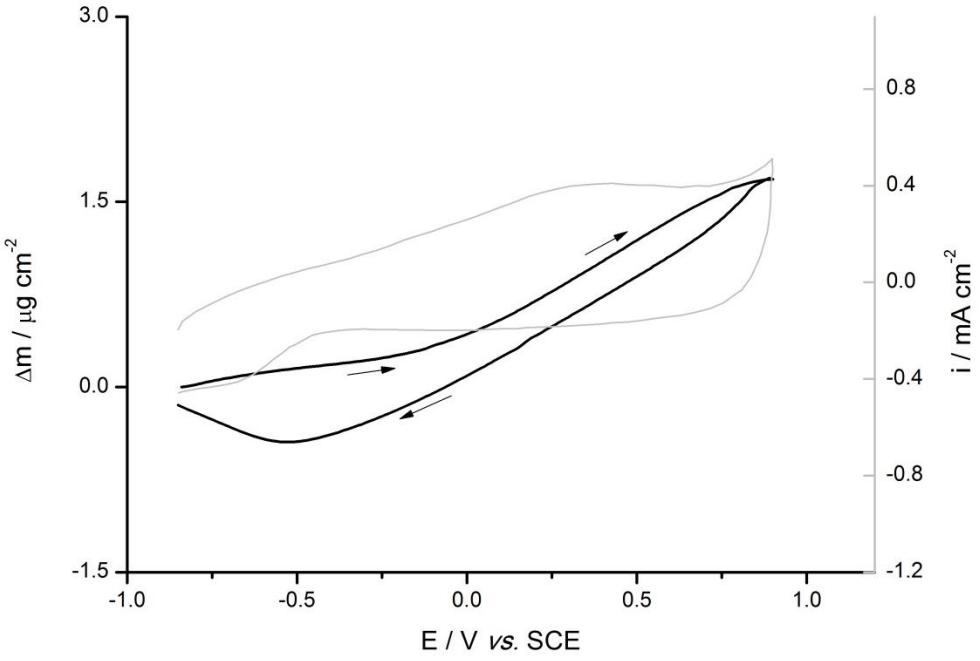

Figure 3.26 – Mass variations during the redox conversion of the potentiodynamically grown PEDOT-PSS (1st cycle) in $LiClO_4/CH_3CN$, after 20 seconds discharge, from -850 to 900 mV at ν=50 mV.s^{-1}. In grey is shown the correspondent cycle voltammogram.

The previous experiments indicate that the anion may also have a role in the redox conversion of the polymer, especially when the polymer is deeply reduced. In a battery, such situation corresponds to a fully discharged device and then there is no problem when dealing with a primary battery but, in the case of a secondary battery (rechargeable) care must be taken in order to not fully discharge the device. Also in this last case, the charging potential of the polymer film should be 1.1V vs. SCE in order to maximize the expulsion of cations preserving the film from overoxidation.

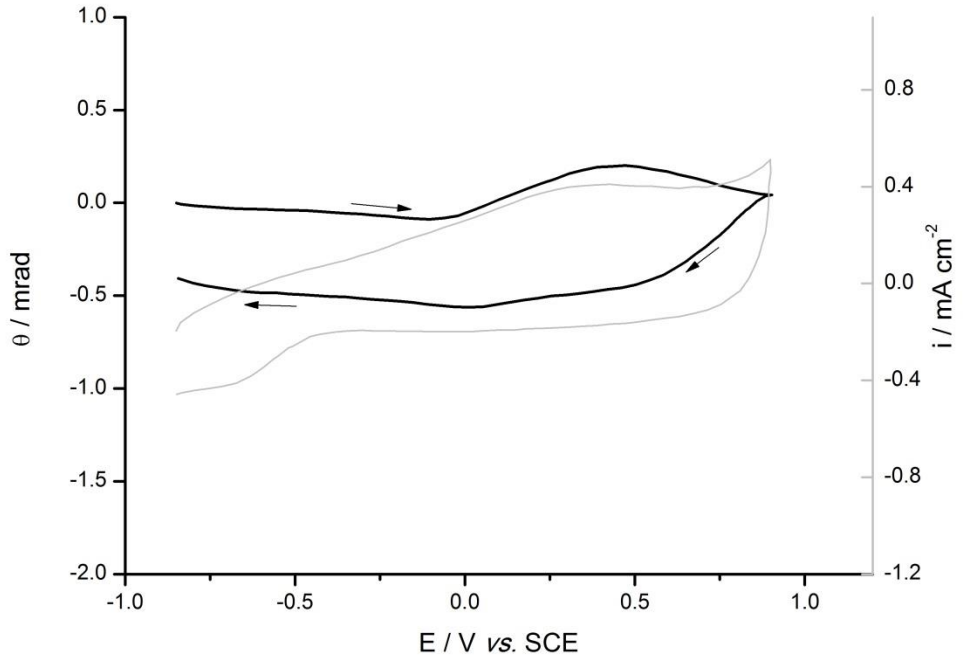

Figure 3.27 – Deflectogram (1st cycle) of PEDOT-PSS, potentiodynamically grown, in $LiClO_4/CH_3CN$, from -850 to 900 mV at v=50 mV.s^{-1}. In grey is shown the correspondent cycle voltammogram.

3.2.3. Galvanostatically grown film in aqueous medium

Nowadays the electrolyte solutions used in batteries, and in particular in Li-ion batteries, are organic but, due to the economical and environmental constraints, the actual research is also directed towards the use of aqueous solutions, which additionally present higher ionic conductivities than the organic ones. Moreover, the mass transfer of Li^+ ions taking place during the redox transformations of PEDOT-PSS was not fully elucidated so far and so, the same approach applied to study this phenomenon in organic solvent was extended to aqueous solutions.

Galvanostatically prepared PEDOT-PSS films similar to those used in the studies in organic solvent (see section 3.1.1) were characterized by cyclic voltammetry in aqueous solution of $LiClO_4$ in the potential range from -0.8 to 0.8 V vs. SCE, being the recorded redox behaviour displayed in Figure 3.28. The overall shape of the voltammogram is similar to that reported in the literature for this polymer in aqueous solution and is characterized by broad oxidation and reduction waves without defined peaks but the cathodic shoulder at ≈-0.4 V.

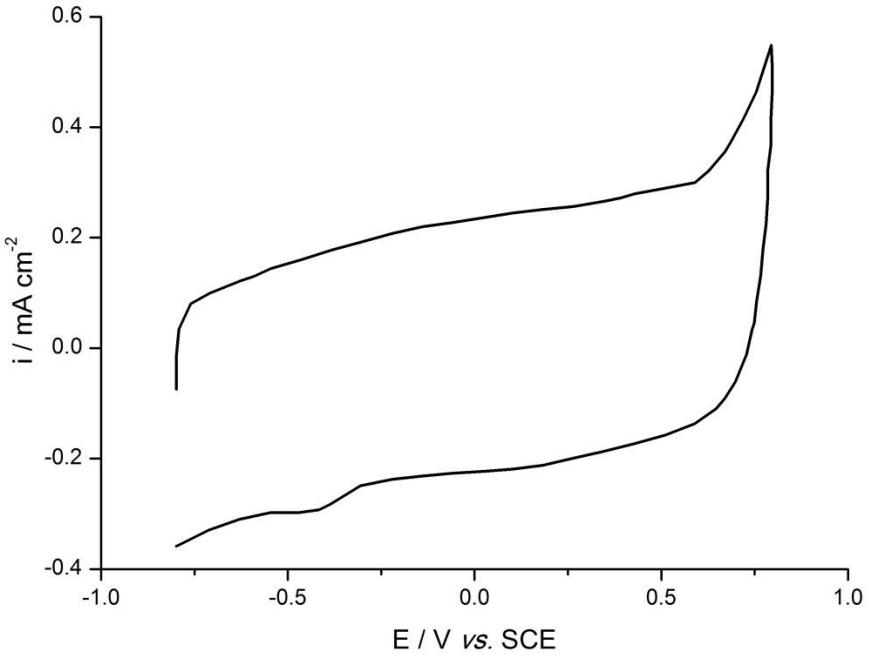

Figure 3.28 - Voltammogram (1st cycle) of PEDOT-PSS, galvanostatically grown, in $LiClO_4/H_2O$, from -800 to 800 mV at ν=50 mV.s^{-1}.

The mass changes recorded during the electrogravimetric experiments with this film are presented in Figure 3.29, showing a continuous mass decrease until 0.2 V followed by an incorporation of mass in the polymer for higher potentials. In the reverse scan the opposite situation is depicted. It should be noted that, irrespective the similar electric charge involved in the redox transformations, the amplitude of mass variation in Figure 3.29 is much smaller than those observed in organic medium, likely due to the lighter water molecule as compared with the acetonitrile molecule.

For this solvent (H_2O) the solvation of ions must be considered converting the light Li^+ ion in a heavy hydrated cation, so the mass variations will be very sensitive to the movements of Li^+ [49,50], as seen in both sweeps between -0.8 and 0.2 V(anodic) and 0.0 to -0.8 V (cathodic). At more positive potentials the mass changes cannot be ascribed to the cation fluxes but may correspond to the entrance and expulsion of solvent (and electrolyte) in the polymer in the anodic and cathodic scan, respectively.

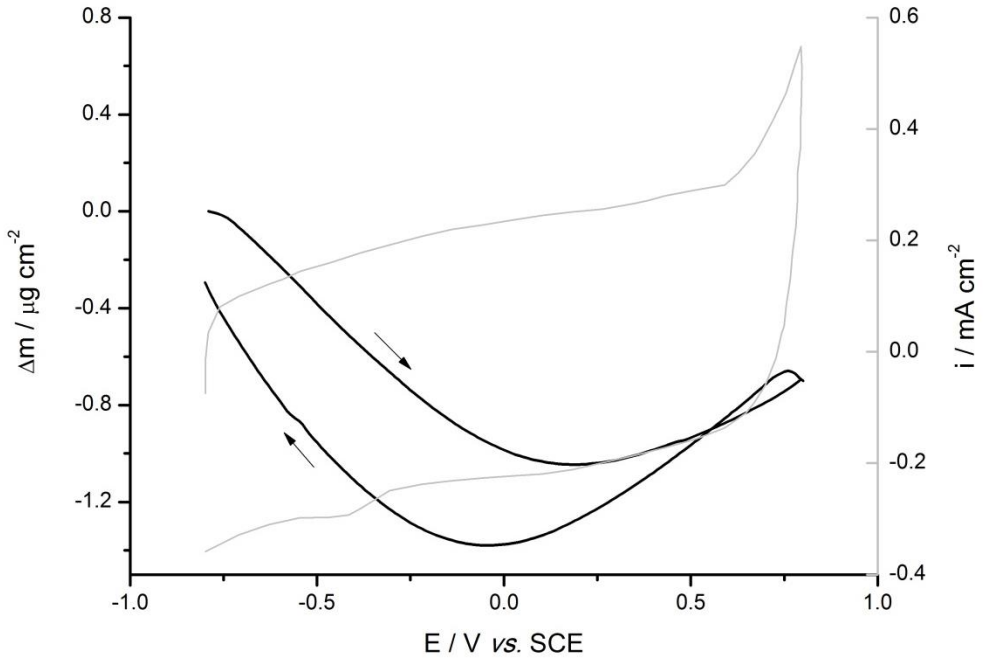

Figure 3.29 - Mass variations during the redox conversion of the galvanostatically grown PEDOT-PSS (1st cycle) in $LiClO_4/H_2O$, from -800 to 800 mV at ν=50 mV.s^{-1}. In grey is shown the correspondent cycle voltammogram.

The PBD analysis of the conversion process of this film in aqueous medium was also performed and the resulting deflectogram is shown in Figure 3.30. As expected the results demonstrate that the redox transformations of the polymer are mainly accompanied by cation ejection and incorporation on oxidation and reduction, respectively. An opposite flux to that of the cation is found at the high positive values and can be due to the transfer of electrolyte (ionic pairs) associated to the structural transformations of the polymer, or to the eventual participation of the ClO_4^- anion as effective counterion for high doping levels. As for the mass fluxes studied by EQCM, also the magnitude of the laser deflection is much lower in aqueous solution than in organic medium which may indicate that the net beam deflection value is a resultant of opposite fluxes from both ionic species, being the net deviation dominated by the cation transfer.

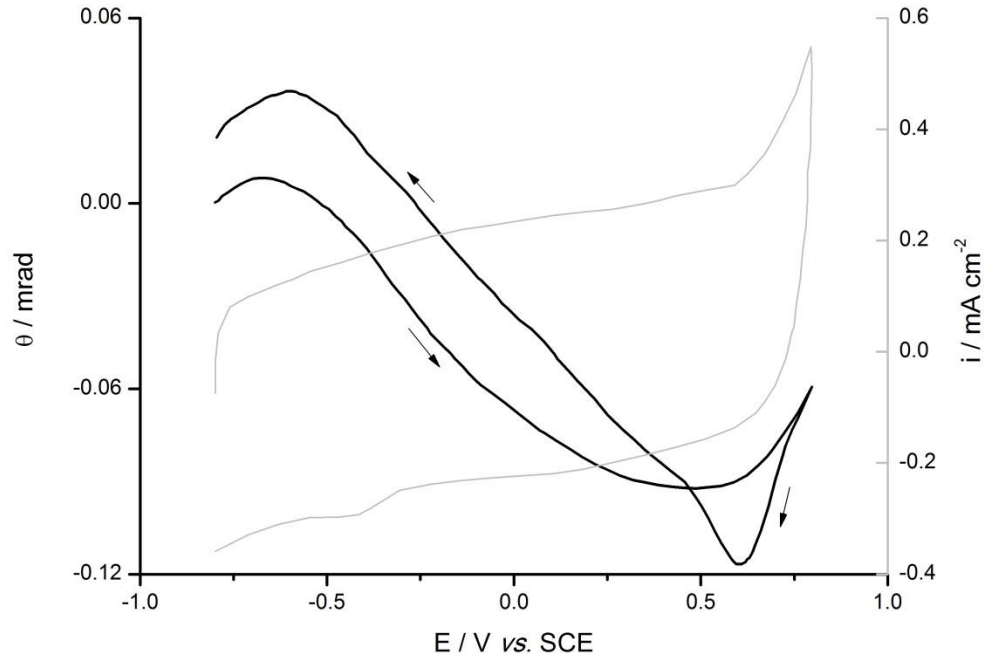

Figure 3.30 - Deflectogram of PEDOT-PSS, galvanostatically grown, in $LiClO_4/H_2O$, from -800 to 800 mV at ν = 50 $mV.s^{-1}$. In grey is shown the correspondent cycle voltammogram.

3.2.4. Potentiodynamically grown film in aqueous medium

A PEDOT-PSS film potentiodynamically prepared (see section 3.1.1) in order to exhibit approximately the same electroactivity of the one galvanostatically synthesized, being its redox behaviour in aqueous solution displayed in Figure 3.31. Its characteristics are similar to those revealed by the polymer prepared under galvanostatic control presented in Figure 3.28.

The EQCM characterization of the polymer conversion is depicted in Figure 3.32, revealing the same overall features as evidenced by the film prepared at constant current but the mass decrease in the anodic scan takes place in a shorter potential interval and the mass uptake occurs sooner and in a larger extension. If the mass incorporation (on oxidation) is due to the intake of solvent caused by swelling of the polymer, this means that those structural transformation happens at lower potentials which is a typical feature of a better organized polymer, with longer chains, as expected for a potentiodynamically prepared film. Is should be mentioned the small hysteresis of the mass transfer process that contributes to a negligible net mass variation during a potential cycle.

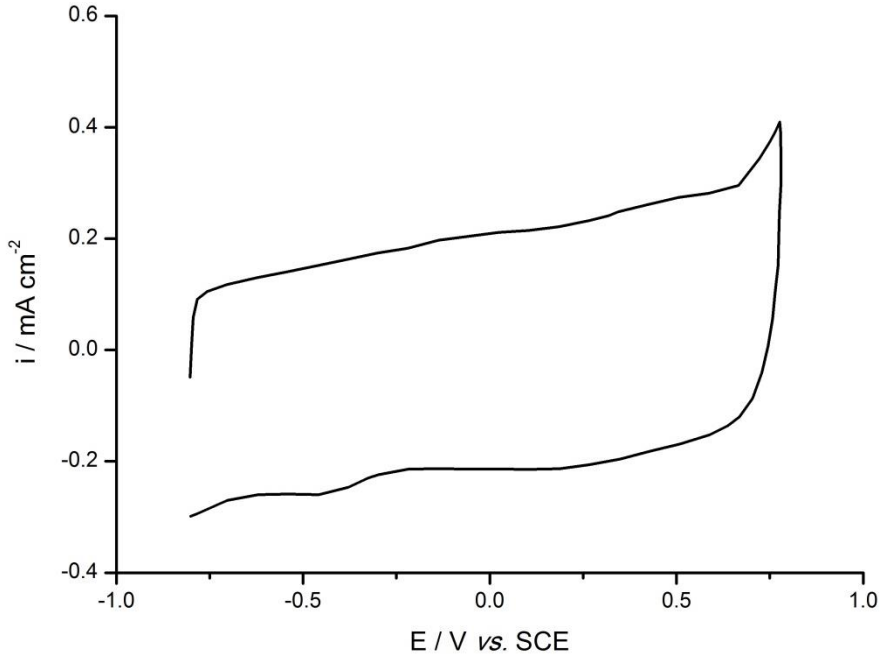

Figure 3.31 - Voltammogram (1st cycle) of PEDOT-PSS, potentiodynamically grown, in $LiClO_4/H_2O$, from -800 to 800 mV at ν = 50 mV.s^{-1}.0

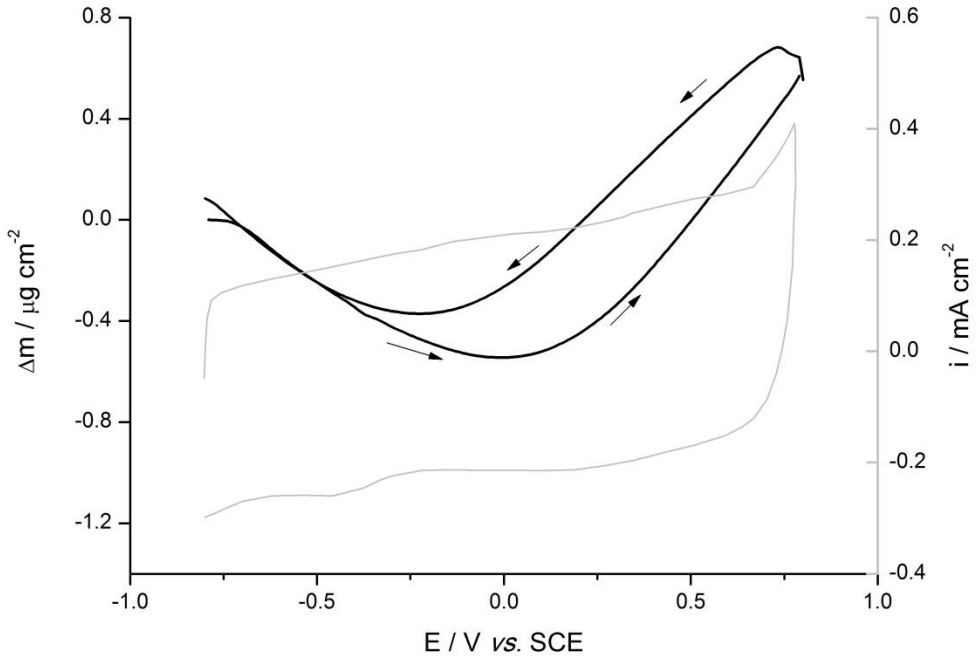

Figure 3.32 – Mass variations during the redox conversion of the potentiodynamically grown PEDOT-PSS (1st cycle) in $LiClO_4/H_2O$, from -800 to 800 mV at ν = 50 mV.s^{-1}. In grey is shown the correspondent cycle voltammogram.

The deflectogram in Figure 3.33 shows that throughout the anodic sweep until 0.2 V there is an outtake of the cations, and afterwards the deflection is mainly ruled by species incorporation on the polymer. The expulsion of cations takes place in a shorter interval than that of the galvanostatic grown film, once again revealing a better structured polymer. However, for a film with approximately the same electroactivity, the magnitude of the beam deflection is much lower than that of the polymer prepared at constant current, clearly showing that the recorded beam deviation results from mixed and opposite fluxes where the anion contribution cannot be disregarded. In particular, in a more compact and organized polymer like the potentiodynamically synthesized one, the ingress and egress of strongly hydrated Li^+ ions may be somewhat difficult and comparable to the ClO_4^- flux out and into the polymer. This hypothesis is supported by the inversion of the deflection of the beam close to the cathodic potential limit during the reductive sweep that suggests anion expulsion at the end of the potential cycle.

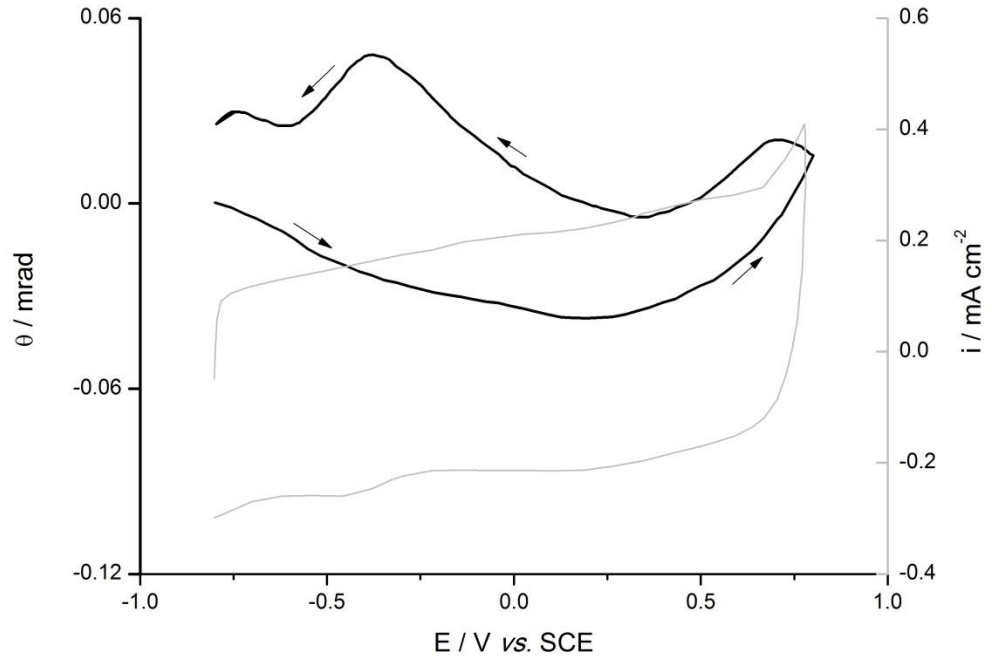

Figure 3.33 – Deflectogram of PEDOT-PSS, potentiodynamically grown, in $LiClO_4/H_2O$, from -800 to 800 mV at $\nu = 50$ mV.s^{-1}. In grey is shown the correspondent cycle voltammogram.

3.3. Conclusion and Future work

The physico-chemical processes taking place during the PEDOT electrochemical growth in an aqueous solution containing NaPSS polyelectrolyte were investigated, where two different electrochemical techniques have been employed. In particular cyclic voltammetry and chronoamperometry have been used to establish the best conditions to synthesize a stable and homogeneous PEDOT-PSS film on a platinum electrode.

This study showed that PEDOT-PSS films deposited from 10 mM EDOT and 0.1 mM NaPSS electrolytic solution, can be formed, are stable and are characterized by a high electroactivity, fulfilling the requirements for a working material under Li^+ ionic transport control to be employed as a cathode in lithium batteries.

The application of macromolecular polyelectrolyte PSS was used to restrict the ionic transport to the Li^+ ion, and the data revealed that the initial purpose was completely achieved in organic medium (the one used in Li-ion batteries); a non-ideal pseudo-cationic doping was identified in aqueous solution, since the perchlorate anion (ClO_4^-) also participates in the conversion process, being the relative extension of each contribution dependent on the electrochemical mode used in the polymer synthesis. These conclusions were only possible to retrieve from the combined information of the PBD and EQCM that allowed distinguishing the solvent mass fluxes from that of the ions, which can be resolved individually.

The extent in which the EQCM signal are affected by the Li^+ transfer is much stronger in water than in CH_3CN due to the apparent mass increase of the Li^+ promoted by the solvation of the small cation by the water molecules.

The experiments indicate that the anion may also have a role in the redox conversion of the polymer, especially when the polymer is deeply reduced. In a battery, such situation corresponds to a fully discharged device and then there is no problem when dealing with a primary battery but, in the case of a secondary battery (rechargeable) care must be taken in order to not fully discharge the device. Also in this last case, the charging potential of the polymer film should be 1.1V vs. SCE in order to maximize the expulsion of cations preserving the film from overoxidation.

The electrochemical synthesis approach presented in this work allows obtaining, from aqueous solutions PEDOT-PSS, films with structural and

electrochemical features reproducible and controlled which could be integrated in some advanced technological devices.

The results are sufficiently encouraging to continue work with PEDOT-PSS as a cathode in lithium batteries and the construction and testing a rechargeable device composed by a PEDOT-PSS cathode and a Li anode should be the natural step in this investigation.

4. Lithium Iron Silicates

There is great interest in investigating Li intercalation compounds that might have application as cathodes in new generations of lithium-ion batteries. Nowadays most of the cathodes used for lithium-ion batteries are transition metals, layered oxides or spinel structures. They rely almost exclusively on the exploitation of lithium colbalt oxide or lithium nickel oxide as the active cathode material. These materials, notwithstanding safety issues, cause of their nature of strong oxidizers in direct contact with an organic electrolyte. Phosphate cathodes, particularly $LiFePO_4$, have been extensively studied and continue to be important.[51–53]

Although this type of cathode materials presents a high theoretical energy density, they also display other issues, such as their instability at the end of the charging process and decomposition at high temperatures.

To develop more stable cathode materials, the Fe olivine phosphate, $LiFePO_4$, has been raised much interest and expectations due to the fact that the oxyanion group (PO_4) makes it more stable than the current oxides, even under severe operating conditions. [51,54–56]

Exploring these advances of the polyoxyanion compounds as safe and cheaper cathode materials, an increasing interest has been focused on silicates as an alternative to phosphates.

In this regard, one advantage of polyoxyanion intercalation compounds, when compared with transition metal oxides is that the binding of oxygen in the polyoxyanions enhances its stability and thus safety.[57–60]

Several wurtzite-type structures with tetrahedrally or tetragonally coordinated ions are known to be good Li-ion conductors. Typically, they contain isolated polyanions AO_4^{n-} with covalent A–O bonds (for A=Al, Si, Ge, P and V). The structural stability of the polyanion matrix allows for a wide range of different cation compositions, with polymorphs exhibiting vacancy- or interstitialcy-driven Li-ion conductivity, and with various pathways and dimensionalities for the ionic conduction process. [61–63]

The strong Si-O bond has the same stabilization effect as the P-O bond in the $LiFePO_4$, and it is valuable characteristic in the delivery of the good reversibility on

cycling because the presence of the strong Si-O bonds that increases the high electrochemical performance of olivine-type silicates, making them potentially low-cost and safe cathode material for large-scale Li-ion battery application.

Li_2MSiO_4 (M= Fe, Ni, Co, Mn) is a new group of electrochemically active silicate-based materials for lithium ion batteries, among which Li_2FeSiO_4 has been given more attention than any other of its family materials.

Furthermore, the reason why silicates such as Li_2FeSiO_4 have attracted increasing attention is that iron and silicon are among the most abundant and therefore lowest cost elements on Earth. Developing cheap and safe cathode materials is a prime target for large-scale lithium batteries in the future.

In all cases, the structure features Silicon and Iron that are connected to oxygen atoms in a tetrahedral coordination, which are plentiful apply and a stable Fe–Si–O bond which provides high thermal stability. [64–66]

Li_2FeSiO_4 was first synthesized and characterized for Li-ion battery application by *Nyten et al* [67] in an organic electrolyte. Also the demonstration of reversible electrochemical lithium insertion–extraction for Li_2FeSiO_4 was also first studied by Nytén et al.[68]. After that, many works have been devoted to the study of this cathode material due to its many advantages such as low cost, abundance of precursors, environmental benignity and high theoretical capacity (166 mAh g^{-1}) for one electron reaction. [68–71] Although all the studies for Li_2FeSiO_4 were made only for one electron reaction, it enables the possibility of extraction more than one lithium per molecule, i.e., the extraction of two Li ions in two consecutive electron redox processes giving rise to a much higher energy density. [72]

However, there are inherent disadvantages of $Li_2FeSiO4$ such as poor electronic conductivity, slow lithium diffusion and ion transmittability, which prevent the attainment of high electrochemical capacity and stable cyclability. To overcome its intrinsic low electrical conductivity of pristine Li_2FeSiO_4, considerable efforts have been made by carbon coating, particle size reduction, and super-valence ion doping [73–75]

The operating voltage of Li_2FeSiO_4 is 2.8 V with a flat charge/discharge profile suggesting a two phase process electrochemistry. The main drawback of this material is its poor conductivity which is in the order of 6×10^{-14} S cm^{-1}([76]).

Many different synthetic routes have been employed to obtain this material such as citric-assisted sol-gel method [77], solid-state method [78,79] and hydrothermal method [58] giving many different structure, polymorphs, whose presence depends on the temperature used for its synthesis.[80]

4.1. Experimental procedures

4.1.1. Synthesis of Li_2FeSiO_4

For the synthesis of this compound, the abundance, cost and also the easiness of synthesis of the starting reagents was considered.

To achieve this goal, three methods were applied: hydrothermal, solid-state reaction and the combustion method.

For hydrothermal synthesis (HTS), stoichiometric amounts of lithium hydroxide (LiOH – Sigma-Aldrich) and of SiO_2 (Sigma), were mixed in 80 mL of water and sonificated in an ultrasonic bath. Iron (II) chloride tetrahydrate (Riedel-de Haen) was separately dissolved in 40 mL of water (these measures were adapted to the autoclave used).

During this work, different stoichiometric molar ratio of Li:Fe:Si were studied (2:1:1, 3:1:1 and 4:1:1) in order to optimize the synthesis process. The prepared dispersion and solution were mixed and transferred into a Teflon-lined stainless-steal autoclave (130 mL of capacity), sealed, and maintained at 150 °C at different dwell times 24, 48 and 72 h. The resulting grey powder was filtrated, rinsed several times with distilled water, and dried under vacuum.

For the solid-state reaction (SS) and combustion method (CM) synthesis, Li_2CO_3 (Sigma-Aldrich), $FeC_2O_4.2H_2O$ (Alfa-Aesar) and SiO_2 (Sigma) were used as starting materials. In the solid-state reaction, the starting materials, in a stoichiometric ratio (Li:Fe:Si = 1:1:1), were dispersed into acetone thoroughly mixed in a mortar to form a slurry mixture, and then calcinated in a horizontal tube under a flowing of N_2 to prevent the oxidation of Fe^{2+} cation.

In the combustion method (CM), in addition to the starting materials, citric acid (Sigma) was also used as fuel. The stoichiometric amounts of reagent grade Li, Fe and Si (1:1:1) sources were dissolved in the minimum amount of distilled water.

The fuel was then added to the solution in a stoichiometric molar ratio of 1:1:1:4 (Li:Fe:Si:$C_6H_8O_7$). The reaction was carried out in a beaker placed on an electric heater and kept at, no more than 120ºC to evaporate the excess water, until the liquid adopted a syrup consistency. Later the syrup swelled up and transformed into brown foam when exposed to continued heating this foamy mass started to burn spontaneously without flame and finally transformed into light and downy brownish-black powder. This ash-formed powder was then collected, ground in an agate mortar, and further heat-treated under a flowing of N_2 to prevent the oxidation of Fe^{2+} cation. For both methods the calcination temperatures were chosen according to the TGA/DSC studies (section 4.2.1) of the starting materials for preparation of Li_2FeSiO_4.

4.1.2. Powder X-Ray Diffraction (XRD)

X-ray powder diffraction (XRD) is a rapid analytical technique primarily used for phase identification of a crystalline material which can provide information on unit cell dimensions. The analysed material is finely ground, homogenized, and average bulk composition is determined.

It's a versatile, non-destructive technique that reveals detailed information about the chemical composition and crystallographic structure of natural and manufactured materials and it is one of the key characterization techniques when working with crystalline materials. The diffraction pattern derives from the interaction of X-rays with the electrons of atoms present in the crystalline lattice. The arrangement of the atoms within the lattice givse rise to constructive or destructive interference of scattered X-rays [81,82]. The selection criteria for the interference can be obtained from Bragg's Law:

$$n\lambda = 2d \sin(\theta) \qquad \text{Equation g}$$

where n is the order of reflection, d the interplanar spacing, and θ the Bragg angle, defined as the angle between the reflecting plane of the crystal and the incident or

reflected beam. First-order reflection (n=1) is normally stronger, and the reflected intensity decreases with increasing n.

The crystallographic structural characterization was performed by X-ray powder diffraction (XRD, Rigaku SmartLab) employing Cu Kα radiation.

Samples were prepared by being ground to powder form using a mortar and pestle, and mounting the powder in specifically designed holders.

Sample analysis was performed with a step size of 0.0152º, a step time of 2 seconds in the diffraction angle range of 2θ from 10 to 80° (where 2θ is the angle between the sample and the incoming ray multiplied by two).

4.1.3. Scanning Electron Microscopy (SEM)

Scanning Electron Microscopy (SEM) was used in order to study the morphology of the synthesized material. SEM functions similarly to a regular microscope, using electrons, instead of light. An electron gun produces a stream of electrons thermionically which are directed towards the anode (target) that contains a small aperture (Figure 4.1). Electrons which pass through the aperture are then focused into a beam using several circular electromagnets. The sample is then placed on the stage which is located at the bottom of the column. Afterwards beam of electrons scan the area around the sample. The electrons are either absorbed by the sample or they are scattered. The scattered electrons are called secondary electrons. These secondary electrons are collected by a detector which converts the signal and a detailed image of the sample is obtained. [40,81,83,84]

Sample analysis was performed at voltages from 5 to 10 kV with a working distance of 15 mm. A FEI Nova™ NanoSEM Scanning Electon Microscope (SEM FEI INSPECT-F) was used to collect all the SEM data.

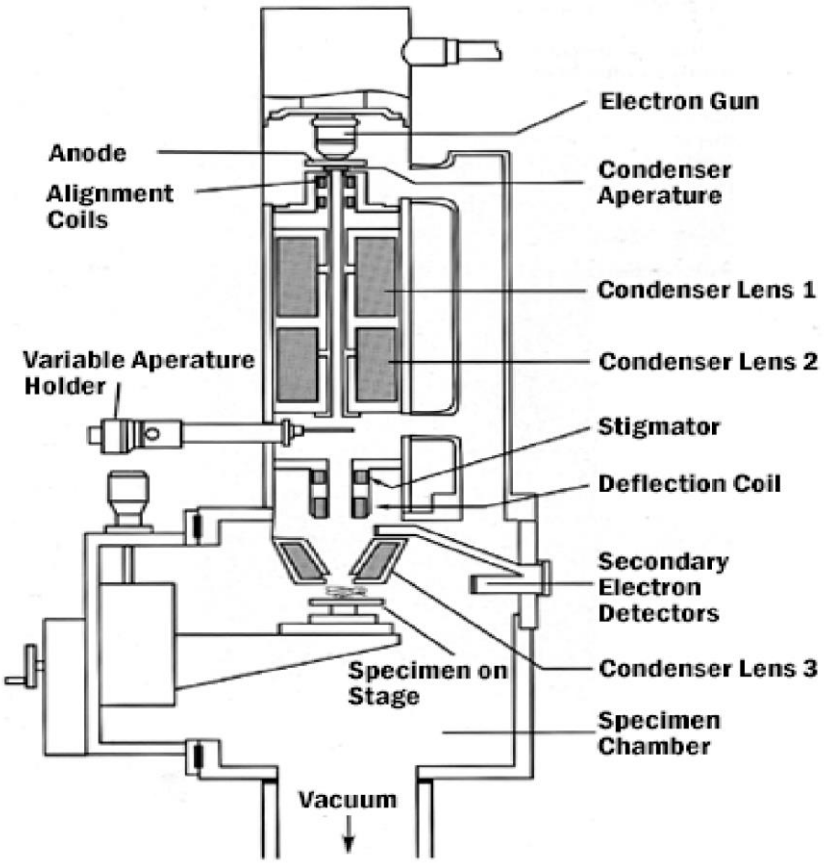

Figure 4.1 – Schematic representation of revelant components inside the SEM. [83]

4.1.4. Thermogravimetric analysis and Differential Scanning Calorimetry (TGA/DSC)

Thermogravimetry analysis (TGA) is one of the most powerful techniques from the standpoint of quantitative data, often being used in combination with other techniques.

It's a technique that is performed to determine the variation in the weight of a sample in relation to change in temperature. This technique allows the investigation of the material thermal stability as well as it's reactivity in a specific atmosphere. Usually, a sample is placed in a platinum or alumina crucible and the furnace is then flushed with the desired gas. The temperature in the furnace is then increased linearly and the change in weight is recorded throughout the experiment.[85]

TGA has been applied extensively to the study of analytical precipitates for gravimetric analysis. Information such as extent of hydration, appropriate drying

conditions, stability ranges for intermediate products, and reaction mechanisms can all be deduced from appropriate TG curves.

The approach taken here can be generalized to the compositional analysis of many materials. TGA also facilitates comparisons of the relative stabilities of polymers and other materials. An analysis of curves prepared at different heating rates makes it possible to extract kinetic data for estimating the service lifetimes of such materials.

Table 4.1 - Processes that can be studied by thermogravimetry. [85]

Process	Weight
Ad- or absorption	Gain
Desorption	Loss
Dehydration/desolvation	Loss
Sublimation	Loss
Vaporization	Loss
Decomposition	Loss

The instrument used for this analysis is a thermobalance. Component details vary according to the design, and the choice of a particular instrument is usually dictated by requirements of the problem under investigation (temperature range, sensitivity, etc.).

The balance transmits a continuous measure of the mass of the sample to an appropriate recording system, which is very often a computer. The resulting plot of mass vs. temperature or time is called a TG curve. Balance sensitivity is usually in the order of one microgram, with a total capacity of as much as a few hundred milligrams.

Differential scanning calorimetry (DSC) is a thermoanalytical technique that measures the difference in the amount of heat required to increase the temperature of the sample in comparison to a reference. There, a reference crucible is placed on an adjacent holder to the sample crucible. The system is then flushed with a desired gas and heated. DSC is useful to measures glass transitions, crystallizations, fusion temperatures as well as a variety of other chemical reactions [81,85–88]

TGA/DSC measurements were performed using a NETZSCH STA 449 C Jupiter apparatus. The advantage of such apparatus is that both the TGA and DSC measurements can be performed simultaneously. The weight loss and heat flow were recorded during both the heating step and the cooling step.

The samples were analysed under Ar atmosphere with a heating rate of 10 °C min^{-1}. The cooling step was set to 20 °C.min^{-1}, because the apparatus used did not contain a rapid cooling system and so there were likely deviations from the set rate.

Afterwards, the samples were heated from room temperature to 1000°C. The sample size varied from approximately 20 to 30 mg.

4.1.5. Electrochemical analysis

The electrochemical properties of the Li_2FeSiO_4 samples were assessed using CR2025 coin cells (Figure 4.2).

The cathode was prepared by mixing 80%(w) of the active material with 10%(w) acetylene black and 10%(w) poly-vinylidene fluoride (PVDF). The role of the PVDF and acetylene black mixture is to connect each particle and bind them together so that electrons can be transported to and from the current collector.

The mixture was made into slurry by using N-methyl-2-pyrrolidene (NMP) as the solvent. The electrodes were formed by coating the slurry onto Al foils. After drying overnight at 100ºC in a vacuum oven, the electrode disks with 12 mm in diameter were cut and weighed. The cells were assembled with the prepared cathode, with lithium metal as the anode and with Celgard 2400 film as a separator. [89]

The electrolytes were 1 mol.L^{-1} lithium hexafluorophosphate ($LiPF_6$) dissolved in ethylene carbonate (EC)/propylene carbonate (PC)/ethyl methyl carbonate (EMC) (1:1:1, volume ratio). Cell assembly was carried out in an ultra-pure Ar-filled glove box. A hand powered press was used to seal the top and bottom casings together. [78]

The electrochemical measurements were performed using a battery test system (LAND CT2001A) between 2.0 V and 3.7 V vs Li/Li+, due to the redox couple of Fe^{2+}/Fe^{3+} that occurs at 2.8 V for Li_2FeSiO_4 vs Li/Li^+.

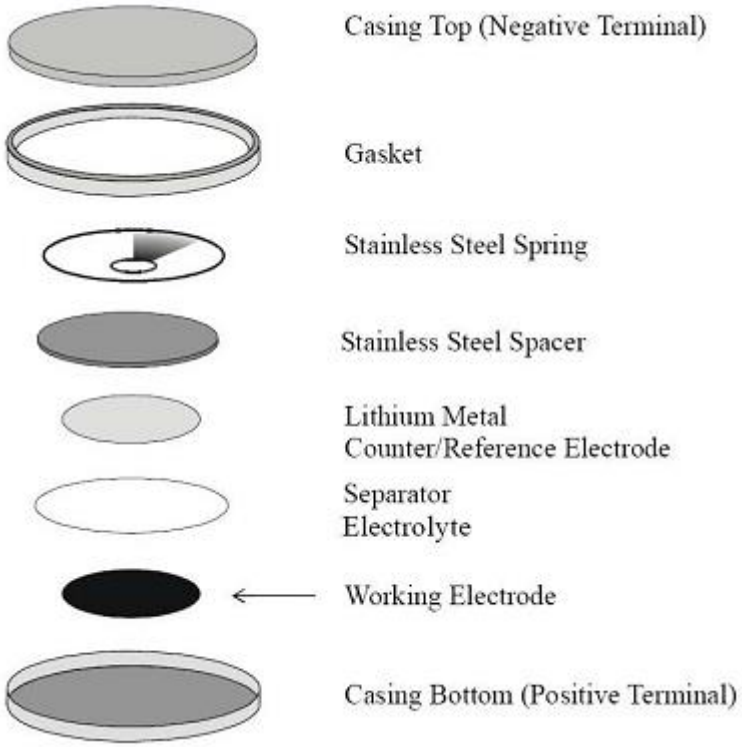

Figure 4.2 - Components of a standard laboratory coin cell. [78]

The cells were cycled on a Battery Testing System LAND CT2001A, Battery Testing System Neware with the BST8-MA software. The current rate was chosen such that a full cycle (charge and discharge) could be performed in ~20 hours..

4.2. Results and discussion

The goal of this part of the project was to create a novel synthesis of Li_2FeSiO_4 using low cost precursors and simple laboratory equipment in order to reduce the overall synthetic cost of this electrode material. The reactions for the different methods to synthesize Li_2FeSiO_4 can be described as showed on Table 4.2:

Table 4.2 - Overall reactions for each of the synthesis methods used on this work.

Synthesis	Reaction
HTS	$LiOH_{(s)}+SiO_{2(s)}+FeCl_2\cdot 4H_2O_{(s)}\rightarrow Li_2FeSiO_{4(s)}+2Cl^-_{(aq)}+4H_2O_{(l)}$
SS	$Li_2CO_{3(s)}+SiO_{2(s)}+FeC_2O_4\cdot 2H_2O_{(s)}\rightarrow Li_2FeSiO_{4(s)}+\uparrow 3CO_{2(s)}+\uparrow 2H_2O_{(s)}$
CM	$Li_2CO_{3(s)}+SiO_{2(s)}+FeC_2O_4\cdot 2H_2O_{(s)}+(n)C_6H_8O_{7(s)}+9/2O_{2(g)}\rightarrow Li_2FeSiO_{4(s)}+\uparrow(8+n)CO_{2(g)}+\uparrow(6+n)H_2O_{(g)}$

These reaction schemes give rise to the desired material along with some side products, without any negative impact on the reaction.

4.2.1. Thermal characterization

To know the optimal sintering temperature for the CM and SS methods, the TGA/DSC technique was attempted, giving the thermogravimetric spectrum of the precursor materials for the preparation of Li_2FeSiO_4 by both synthesis methods, which is displayed in Figure 4.3.

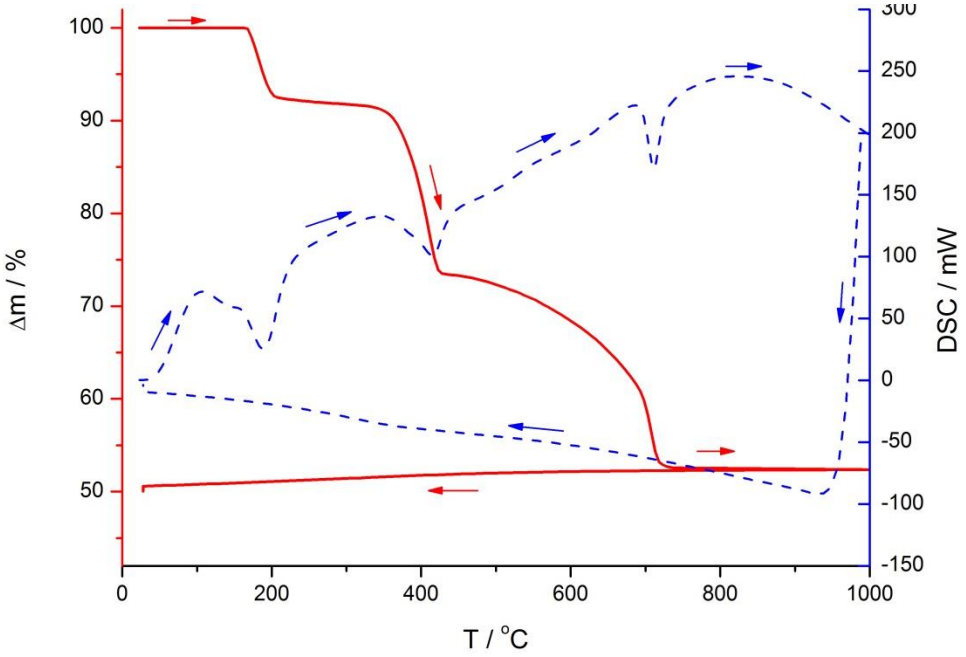

Figure 4.3 – Spectrum of the TGA and DSC measurement curves for the precursor materials for the synthesis of Li_2FeSiO_4 (mixture of Li_2CO_3 - SiO_2 - $FeC_2O_4 \cdot 2H_2O$)

The TGA curve is shown in red, while the associated DSC curve is shown in blue.

In this temperature sweep the DSC curve presented two endothermic heat flows at 188 and 410ºC, and obvious mass loss (8.5 and 18.6 %, respectively) is also seen in the TGA curve, corresponding to losing lattice water and the decomposition of $FeC_2O_4 \cdot 2H_2O$, respectively. As the temperature rises, a wide endothermic heat flow appears at 710ºC in the DSC curve, and continual mass loss is observed in the TGA curve, indicating the decomposition of Li_2CO_3 and formation of silicate. The

mass of raw materials did not decrease over 710ºC, so it can be concluded that the reaction could not be achieved at annealing temperature below 710ºC.

The weight of the sample after 800 °C then stays constant until the end. During the cooling of the sample, the weight does not change. In the case of the DSC, during the heating step an endothermic event is observed at approximately 975 °C which has not been identified, but it may be associated with the crystallization of Li_2FeSiO_4.

All this is in accordance to what has been described elsewhere.[67,90–93]

4.2.2. Structural characterization

According to the latest reports, Li_2FeSiO_4 assumes two typical structures: α-Li_3PO_4 based orthorhombic structure with Pmn_{21} space group (ICSD-262047)[52] and with Pmnb space group (ICSD-247485)[66], the first being most common than the second. Their X-ray Diffraction patterns are represented respectively in Figure 4.4 and Figure 4.5.

The lattice parameters for these structures are shown on Table 4.3.

Table 4.3 - Reported structural data on Li_2FeSiO_4 in the literature.

Space group	a / Å	b / Å	c / Å	V / Å^3
Pmn_{21}	6.278(1)	5.351(1)	4.972(1)	167.027
Pmnb	6.284(7)	10.657(1)	5.039(1)	337.418

Although all the samples of this work have been compared with both patterns of the two different space-groups above, the diffractograms shown next only present the comparison with the Pmn_{21} space-group.

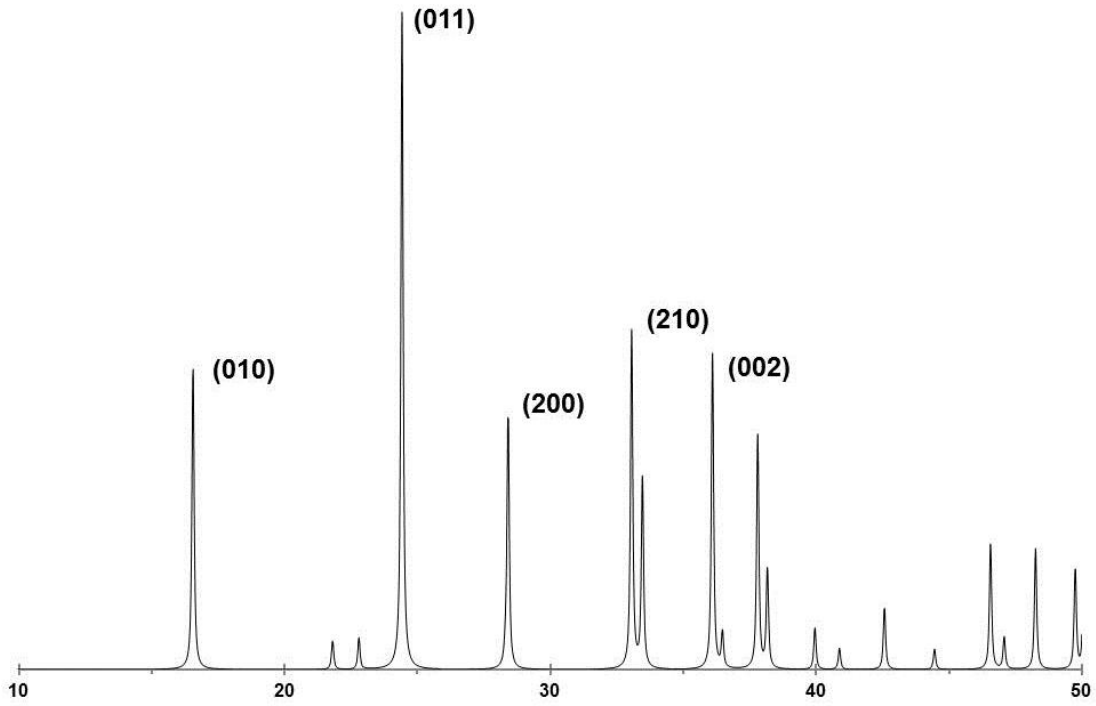

Figure 4.4 - X-ray Diffraction powder pattern of Li_2FeSiO_4 with space group: Pmn_{21} [52] and respective Miller indexes.

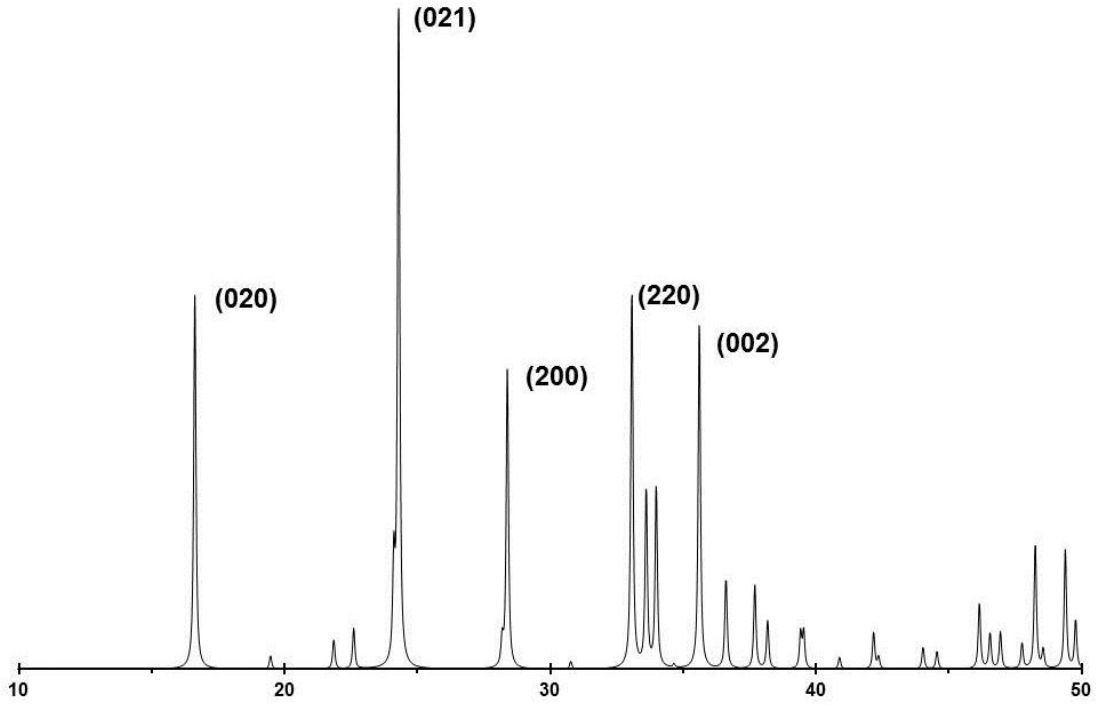

Figure 4.5 - X-ray Diffraction powder pattern of Li_2FeSiO_4 with space group: Pmnb[66] and respective Miller indexes.

The first synthesized and characterized sample was the one obtained by the HTS method. Initially, the X-Ray diffractometer used in the beginning of this work (STOE *Stadi P*) didn't plot a suitable XRD pattern for either of the samples studied, when compared with the literature, as will be shown further.

Due to this fact, changes to optimize the synthesis processes studied in this work were attempted, as will be explained further.

For the HTS method of synthesis, specifically, none of the optimization changes seemed to work, since the several XRD patterns obtained were similar to the one shown on Figure 4.6. Consequently, this synthesis method was abandoned and the following experiments focused on the optimization of the other two synthesis methods.

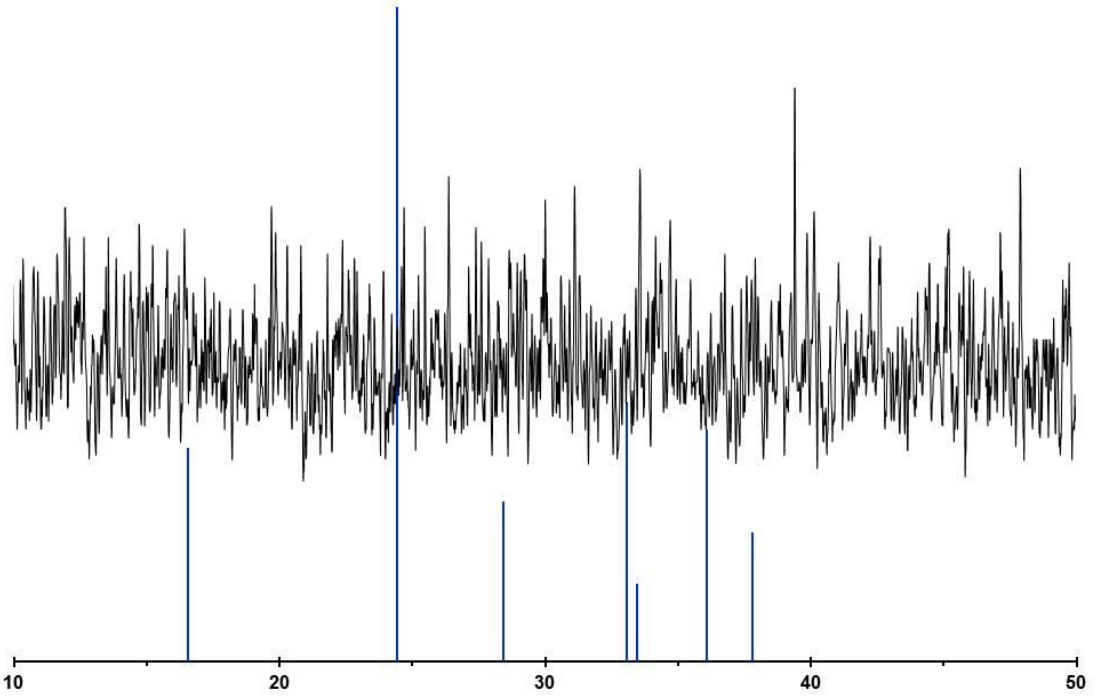

Figure 4.6 - X-ray Powder diffractogram of Li_2FeSiO_4 synthesized by HTS method (1:1:1 ratio) for 48h at 150ºC. Measurements done with the STOE diffractometer. Also reported bars of that correspond to the pattern X-ray Powder diffraction of Li_2FeSiO_4 with Pmn_{21} space group.[52]

Therefore, synthesis the Li_2FeSiO_4 was attempted using the CM and SS methods. Since the starting materials are about the same in both methods, as said earlier, a TGA was made to discover the desirable calcination temperature.

Unfortunately, these synthesis methods were not showing good preliminary results either as shown on Figure 4.7 and Figure 4.8.

As is illustrated in Figure 4.7 the diffractogram obtained from the sample of the CM method sintered for 8h as 800ºC, shows a powder diffraction pattern different from the one expected for the Li_2FeSiO_4 material. After running a search through the ICSD files, it was found that this diffractogram is very similar to the Fe powder pattern (ICSD-41506)[94] which may be explained by the Fe fluorescence, that blinds the true powder diffraction pattern of the sample, as previously reported by *Armstrong et.al.*[65]. Nevertheless, this fact was ignored, as there were previous reports on this compound using Cu Kα radiation with the same diffractometer.[67]

In addition, the sample from the SS method, which was also sintered for 8h at 800ºC showed no-affirmative results either, as shown in Figure 4.8. It became apparent that there were still optimization changes to be made in both methods, in order to obtain the expected compound. This was of major importance, since the synthesis of the desired compound had to be validated with a difractogram showing the appropriate powder diffraction pattern.

Furthermore, attempts at optimizating both synthesis methods by changing the calcination temperature and dwell time were performed, but did not produce any significant changes on the powder diffraction patterns obtained in all the new samples synthesized, since the obtained diffractograms were similar to the ones illustrated on Figure 4.7 and Figure 4.8.

Due to this, another type of change on the initial features of the synthesis methods was then attempted, by changing one of the starting materials. Even though this compound is more expensive than the one used in the beginning, FeO was used instead of $FeC_2O_4 \cdot 2H_2O$, in order to avoid even more side products during the synthesis process. The overall reactions are shown on Table 4.4.

Table 4.4 - Overall reactions for each of the synthesis methods used on this work after the optimization changes.

Synthesis	Reaction
SS	$Li_2CO_{3(s)}+SiO_{2(s)}+FeO_{(s)} \rightarrow Li_2FeSiO_{4(s)}+\uparrow CO_{2(s)}$
CM	$Li_2CO_{3(s)}+SiO_{2(s)}+FeO_{(s)}+(n)C_6H_8O_{7(s)}+9/2O_{2(g)} \rightarrow Li_2FeSiO_{4(s)}+\uparrow(6+n)CO_{2(g)}+\uparrow(4+n)H_2O_{(g)}$

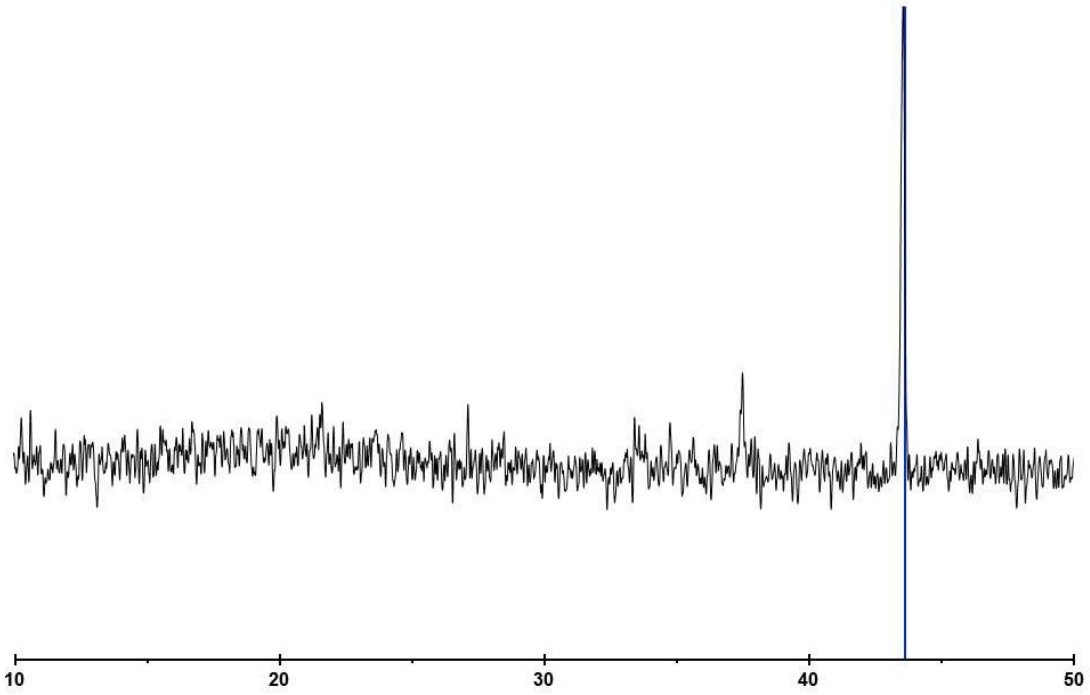

Figure 4.7 - X-ray powder diffractogram of Li_2FeSiO_4 synthesized by CM for 8h at 800ºC in N_2 atmosphere, measurements done with the STOE diffractometer. Also reported bars of that correspond to the pattern X-ray Powder diffraction of Fe.[94]

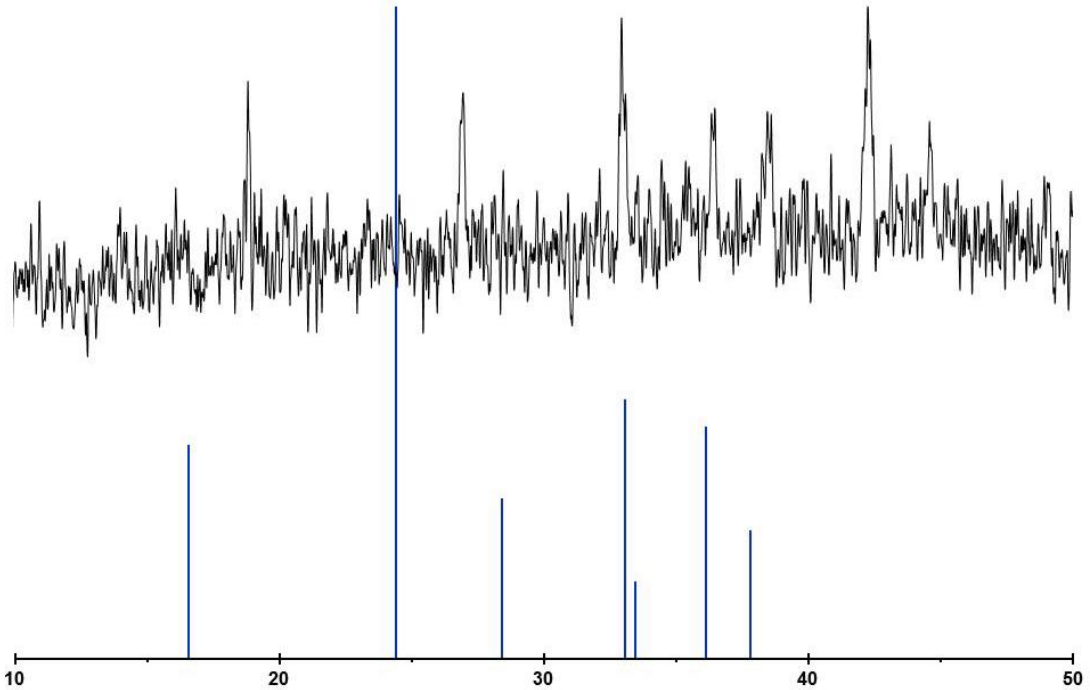

Figure 4.8 - X-ray powder diffractogram of Li_2FeSiO_4 synthesized by SS for 8h at 800ºC in N_2 atmosphere. Measurements done with the STOE diffractometer. Also reported bars of that correspond to the pattern X-ray Powder diffraction of Li_2FeSiO_4 with Pmn_{21} space group.[52]

After the adjustments on both samples mentioned above, the synthesis were made and both structural analysis seemed to change, as can be seen by the appearance of the diffraction peaks at the Bragg angles resulting from the Miller index (010), (011), (200), (210) and (120) show on Figure 4.9 and Figure 4.10 which indicate that the phase of the Li_2FeSiO_4 was starting to form. This change was seen after a heating at 800ºC for 10h; after this two other heating rounds were performed, at the same temperature and dwell time for both.

After the second heating round the diffraction peaks for the Miller indexes described above sharpen, specially the (011) peak, suggesting that the Li_2FeSiO_4 phase was forming, and that with the continued heating rounds it was possible to finally achieve the desired compound. However, after the third heating round, the obtained diffractograms present once again an unsatisfactory result, similar to the ones seen previously on Figure 4.7 and Figure 4.8.

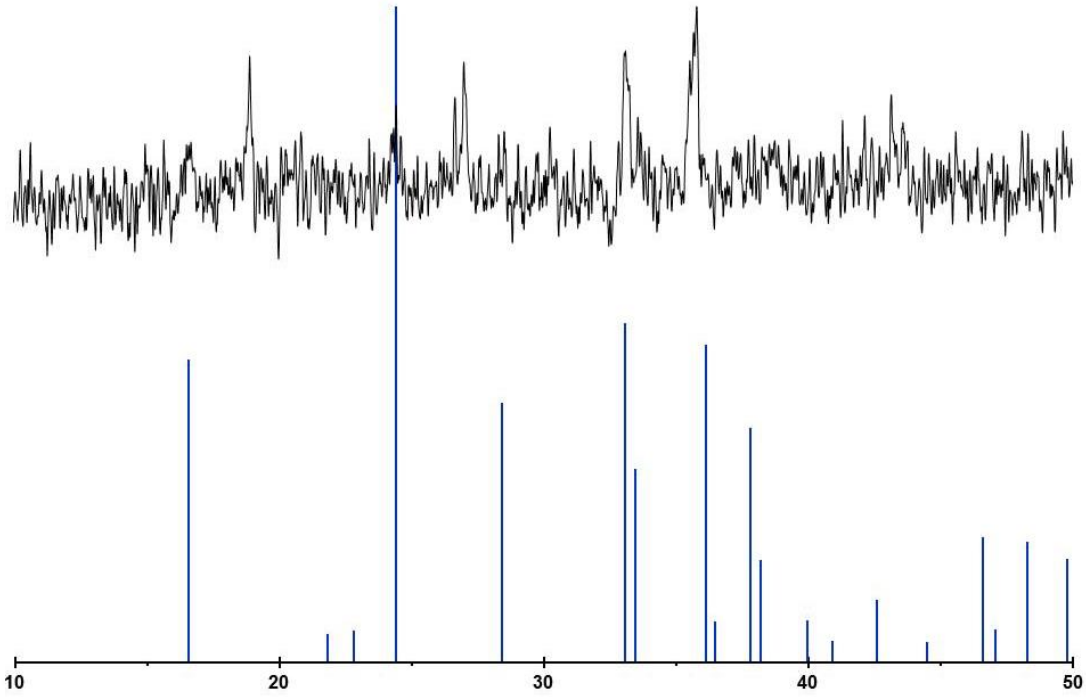

Figure 4.9 - X-ray powder diffractogram of Li_2FeSiO_4 synthesized by CM for 10h at 800ºC in N_2 atmosphere. Measurements done with the STOE diffractometer. Also reported bars of that correspond to the pattern X-ray Powder diffraction of Li_2FeSiO_4 with Pmn_{21} space gr oup. [52]

The obtained diffractogram, shown in Figure 4.10, indicates that the powder pattern seems to have gotten worse than expected, which was odd, because the

heating of the compound should aid on the formation of the desired phase since the diffraction peaks become high and sharp, indicating the crystallinity of the compound increases.

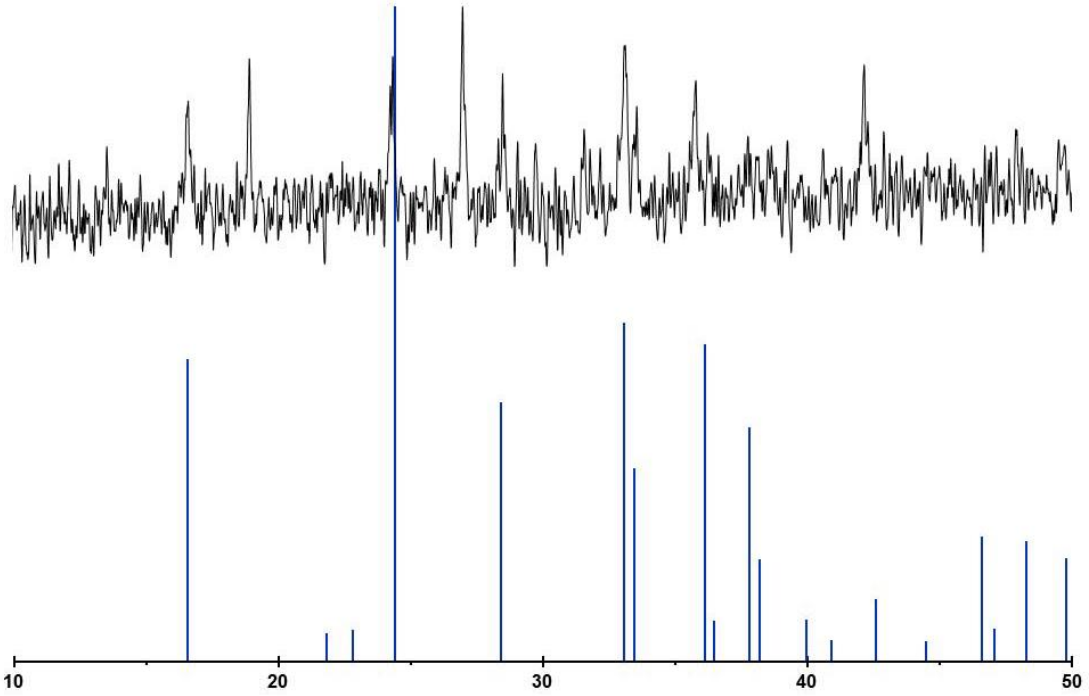

Figure 4.10 - X-ray powder diffractogram of Li_2FeSiO_4 synthesized by SS for 10h at 800ºC in N_2 atmosphere. Measurements done with the STOE diffractometer. Also reported bars of that correspond to the pattern X-ray Powder diffraction of Li_2FeSiO_4 with Pmn_{21} space gr oup.[52]

Due to this, the last two samples were measured on the RIGAKU diffractometer, since it is a more powerful device and inhibits the Fe-fluorescence in the diffractogram, which was regarded this time. The diffractograms obtained are shown on Figure 4.11 and Figure 4.12.

As shown on these diffractograms, the Fe-fluorescence should never be disregarded, since it blinded the true structural aspects of the synthesized samples of Li_2FeSiO_4.

When comparing the diffractogram obtained with the literature, it becomes apparent that the desired phase of Li_2FeSiO_4 was formed, even though there were some identified impurities.

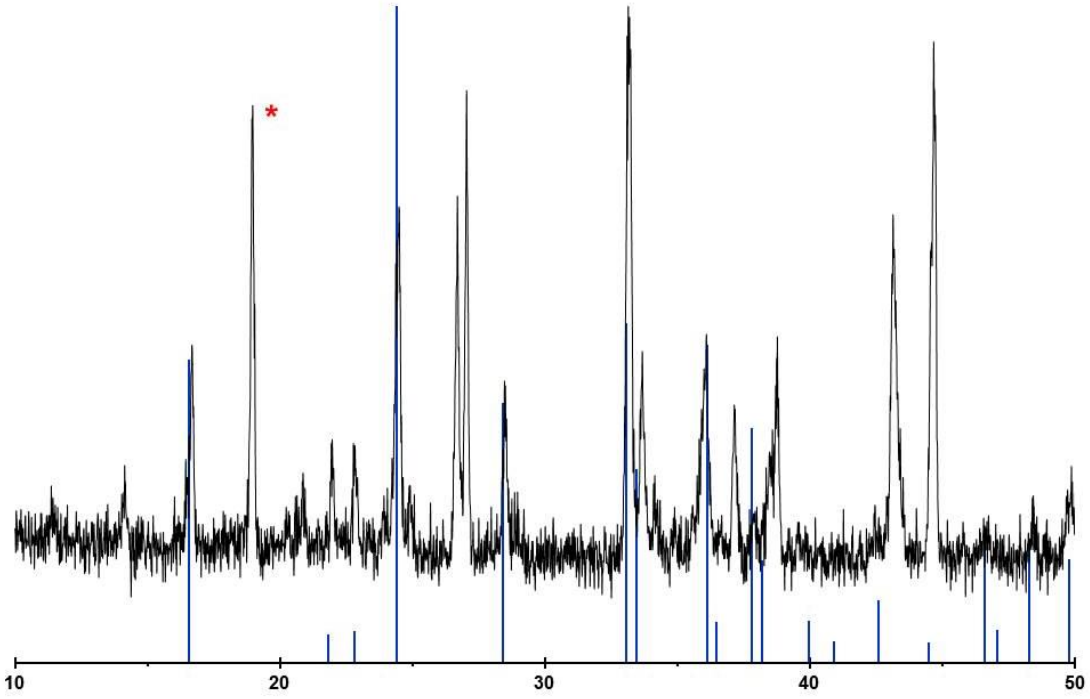

Figure 4.11 - X-ray powder diffractogram of Li_2FeSiO_4 synthesized by CM for 10h at 800ºC in N_2 atmosphere. Measurements done with the STOE diffractometer. Also reported bars of that correspond to the pattern X-ray Powder diffraction of Li_2FeSiO_4 with Pmn21 space group[52](*Li_2SiO_3 – ICSD-853)

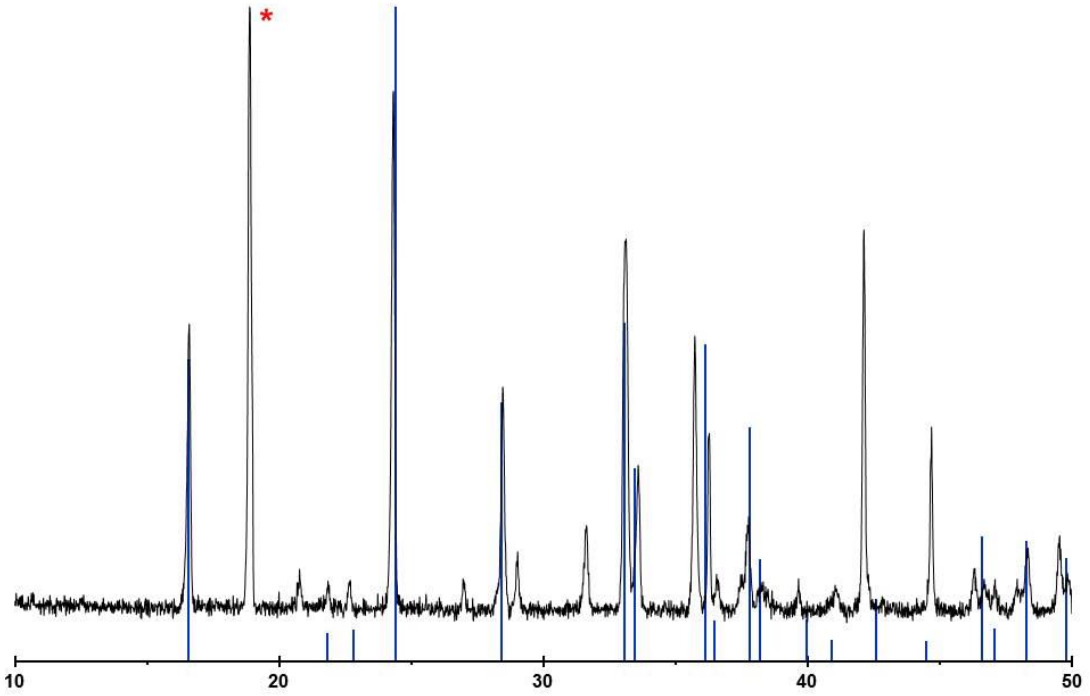

Figure 4.12 - X-ray powder diffractogram of Li_2FeSiO_4 synthesized by SS method heated for 10h at 800ºC, 3 times, in N_2 atmosphere. Measurements done with RIGAKU diffractometer. Also reported bars of that correspond to the pattern X-ray Powder diffraction of Li2FeSiO4 with Pmn21 space group.[52] (*Li_2SiO_3 – ICSD-853)

As shown in Figure 4.11 and Figure 4.12 the diffraction peaks referring to the expected Miller indexes did increase with the three heating rounds. Also, another phase was identified at the Bragg angle ~18º, which was identified on the ICSD database as Li_2SiO_3 (ICSD-853), which may indicate that the reaction was not complete and possibly needed a significantly higher number of heating rounds, in order to acquire the final Li_2FeSiO_4 phase.

Considering these new discoveries, another XRD pattern of the first sample synthesized by the HTS method was attempted but this time on the RIGAKU diffractometer.

The resulting XRD pattern of this sample is shown in Figure 4.13. and it seemed to indicate that the Li_2FeSiO_4 phase was formed giving rise to a diffraction profile similar to the one present in the literature[67,78,79,74]. However, some impurities were detected, namely $FeSiO_4$ (ICSD-69460) and Li_2SiO_3 (ICSD-853), which could develop from the synthesis process, or from the structural instability due to the oxidation of the material, when exposed to the air, as described elsewhere [90].

From the CM and SS methods, as previously shown, a small amount of the Li_2FeSiO_4 phase was formed. Unfortunately, these methods didn't seem promising, since after the calcination process the powder tends to adhere to the porcelain crucible leading to a lower product yield. Furthermore, it needs high calcination temperatures and extensive dwell times. Additionally, the high cost of the FeO in comparison to the other available Fe-compounds makes these last two methods significantly more expensive.

Due to these facts coupled with the lack of time to optimize all the synthesis methods simultaneously, and in order to achieve the goals proposed in this work, it was necessary to focus on only one of the synthesis methods used. The HTS method was thus chosen for further optimization.

Moreover, due to the problems generated by the diffractometer used (STOE), all the following XRD patterns were subsequently performed in the RIGAKU X-Ray diffractometer.

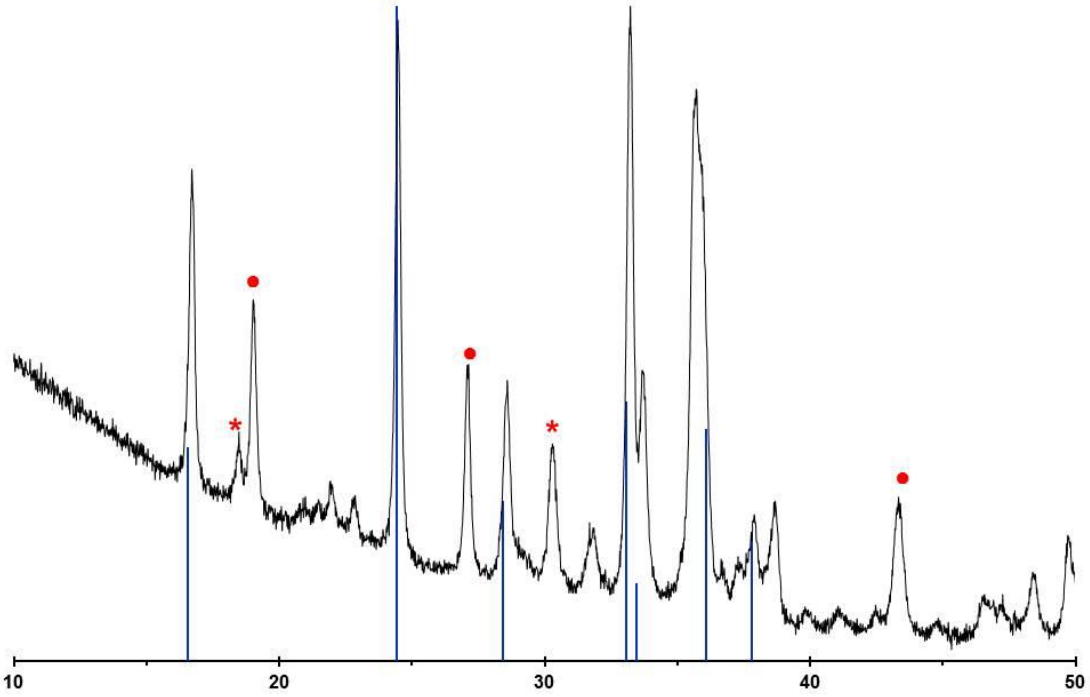

Figure 4.13 - X-ray powder diffractogram of Li_2FeSiO_4 synthesized by HTS (ratio 1:1:1) heated for 48h at 150ºC. Measurements done with RIGAKU diffractometer. Also reported bars of that correspond to the pattern X-ray Powder diffraction of Li2FeSiO4 with Pmn21 space group.[52] **(*Fe_2SiO_4 – ICSD- 69460; ●Li_2SiO_3 – ICSD-853).**

The optimization changes mentioned above regarding the stoichiometric molar ratio of Li:Fe:Si, and the dwell time in the autoclave, were once again performed. as described above (Synthesis of Li2FeSiO4).

All of the compounds synthesized by this method where the Li_2FeSiO_4 was formed appeared to have the same powder pattern.

However, the samples also seemed to contain significant amount of $FeSiO_4$ (ICSD-69460) and Li_2SiO_3 (ICSD-853).

The best results were obtained by using the stoichiometric ratio of 4:1:1 and the dwell time of 72 h. The XRD pattern of the sample obtained these parameters is represented in Figure 4.14.

These parameters were used for all subsequent studies.

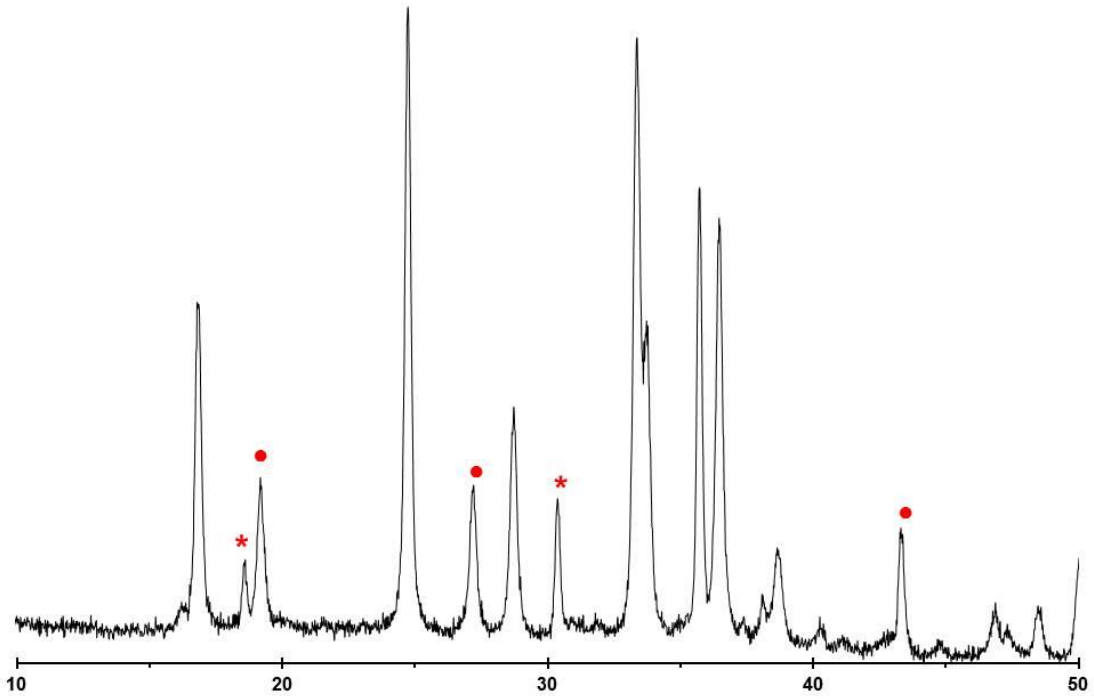

Figure 4.14 - - X-ray powder diffractogram of Li_2FeSiO_4 synthesized by HTS (ratio 4:1:1) heated for 72h at 150ºC. Measurements done with RIGAKU diffractometer. Also reported bars of that correspond to the pattern X-ray Powder diffraction of Li2FeSiO4 with Pmn21 space group.[52] (*Fe_2SiO_4 – ICSD- 69460; ●Li_2SiO_3 – ICSD-853).

The XRD pattern of this sample shown in Figure 4.14 can be indexed to the orthorhombic system with Pmn_{21} space group.

The narrow diffraction peaks indicate that the sample has good crystallinity, even though there are still two impurities in the sample, mainly $FeSiO_4$ (ICSD-69460) and Li_2SiO_3 (ICSD-853).

It was possible to compute the cell parameters of the synthesized sample using the *Checkcell program*[95] by the diffraction peaks obtained. The phase can be indexed by the orthorhombic unit cells of 6.4651, 5.329 and 4.972 Å, closely matching those of *Nytén et al* [67], as compared in Table 4.5

Table 4.5 - Li_2FeSiO_4 cell parameters in the literature and the calculated from the sample.

Space group	a / Å	b / Å	c / Å	V / Å3
Pmn_{21}	6.278(1)	5.351(1)	4.972(1)	167.027
Li_2FeSiO_4_HTS	6.465(1)	5.329(3)	4.862(3)	167.521

4.2.3. Morphological characterization

Particle size and morphology of the synthesized sample was analysed using SEM. In Figure 4.15 are the SEM images of the sample mentioned above. It shows that there are many fine particles and agglomeration in the sample which has a wide particle size distribution. This sample consists of non-uniform agglomerates typically 7 to 10 µm in size. The agglomerates which are formed from smaller interconnected particles measure ~250 nm. Usually, Li_2FeSiO_4 with small particle size, in the range of 50 to 250 nm, is favourable for Li^+ diffusion because it shortens the distance of Li^+ diffusion in solid particles leading to an overall increase in performance.[64,65]

Hence, a milling procedure was performed on the obtained material to reduce the particle size, which should result in superior performance.

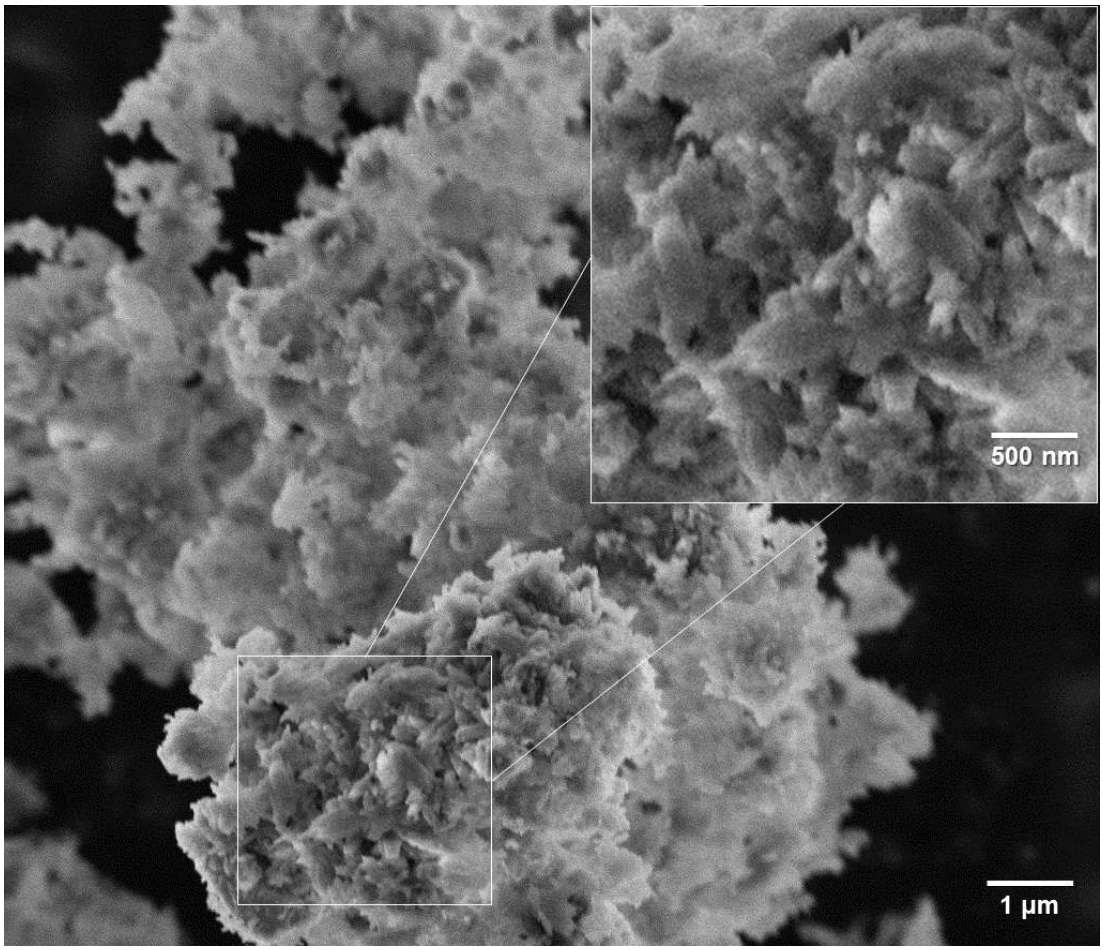

Figure 4.15- SEM data at different magnification with a scale bar of 1 µm and 500 nm for the synthesized Li_2FeSiO_4 particle by HTS (ratio 4:1:1) heated for 72h at 150°C.

4.2.4. Electrochemical characterization

As was mentioned before, the study of the processes of discharge and charge are very important to understand the function of the battery.

Table 4.6 – Redox reactions on the electrodes for the discharge and charge processes.

Process	Redox reactions on the electrodes
Discharge	Anode: $Li_{(s)} \rightleftharpoons Li^{+}_{(aq)} + e^{-}$ Cathode: $LiFeSiO_{4(s)} + Li^{+}_{(aq)} + e^{-} \rightleftharpoons Li_2FeSiO_{4(s)}$
Charge	Cathode: $Li_2FeSiO_{4(s)} \rightleftharpoons LiFeSiO_{4}{}_{(s)} + Li^{+}_{(aq)} + e^{-}$ Anode: $Li^{+}_{(aq)} + e^{-} \rightleftharpoons Li_{(s)}$

Normally applying a high current leads to smaller capacity and a lower current leads to higher capacity due to the system being close to an equilibrium state

Due to the low intrinsic conductivity of Li_2FeSiO_4, a carbon coating step is essential to enhance the electrical conductivity and obtain improved electrochemical performance from the material.

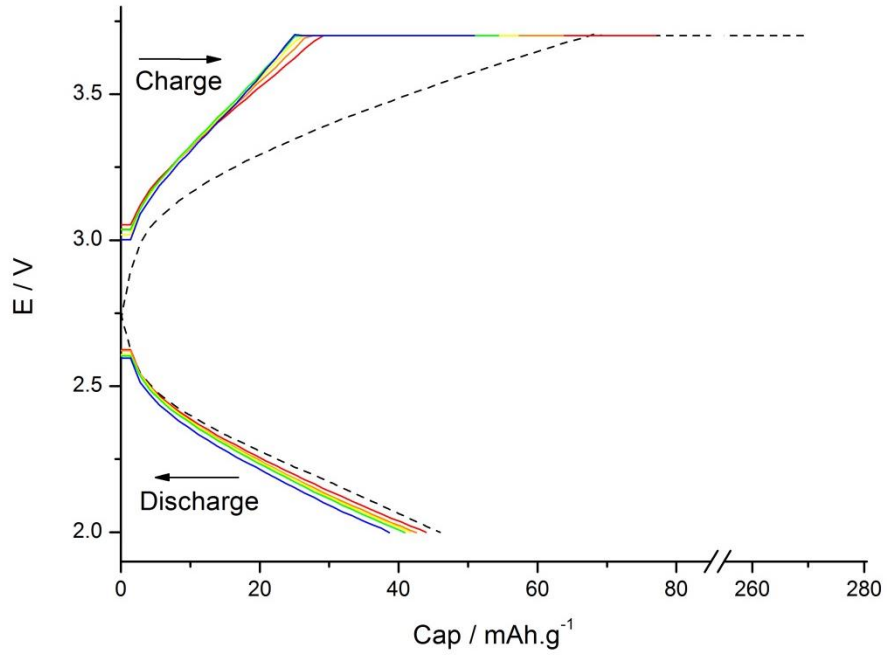

Figure 4.16 - Voltage versus capacity plot of Li_2FeSiO_4. Black-dash, red, orange, yellow, green, blue curves correspond to the 1st, 3rd, 5th, 7th, 9th and 11th, respectively.

Figure 4.16 shows the voltage versus capacity plot of the synthesized Li_2FeSiO_4. The battery assembly details are described in the experimental section (4.1.5. Electrochemical analysis).On the first charge/discharge cycle, denoted with the black line, the charging capacity was 269.23 $mAh.g^{-1}$ and the discharging capacity was 46 mAh g^{-1}, while in the second cycle the charge capacity is 77.02 $mAh.g^{-1}$ and the discharge capacity was 43.93 $mAh.g^{-1}$. *Nytén and al.*, suggested that the voltage drop after the first cycle is attributed to a phase transition to a more stable structure.[67]

Cycling data is presented in Figure 4.17. It can be observed that both charge and discharge profiles during the different cycles, tend to decrease from the 2nd cycle to the 11th. The small capacity delivered by this material, is probably due to the structure's instability: this means that during the charge process most of the Li^+ ions that were inserted during the discharge process could not get out of the cathode during the charge process, hence a high charge capacity and a low discharge capacity. Tin spite of this poor cycle, a good efficiency of about 80% was obtained with this battery.

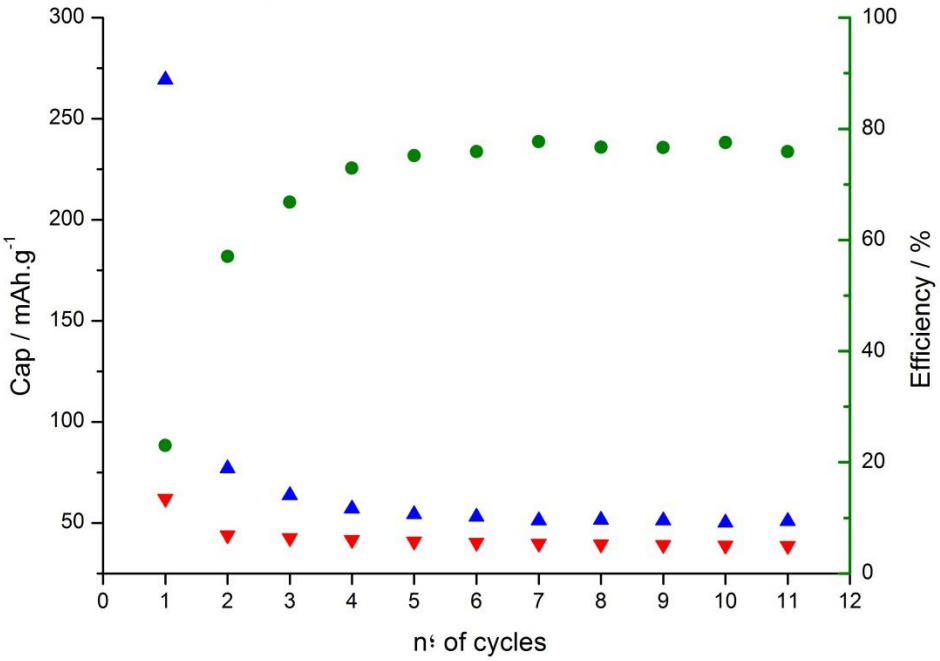

Figure 4.17 - Charge capacity (▲blue dots), discharge capacity (▼red dots) and efficiency (●green dots) versus cycling of the carbon coated Li_2FeSiO_4.

4.3. Conclusion and Future work

When working with inorganic synthesis, it is always difficult to obtain high purity materials, and consequently reproducible results and high conductivity.

In this work it has been demonstrated that it is possible to synthesize Li_2FeSiO_4 from low cost precursors via simple synthesis methods.

The synthesis originated a material with large particle size which formed large agglomerates with high crystallinity but poor conductivity. The material was milled to reduce particle size and carbon coated in order to obtain good electrochemical data. Unfortunately, theoretical capacity was not reached for these samples; still a good battery efficiency of 80% was achieved.

The most probable reason behind the low electrochemical performance was that even after milling the particle size was still quite large and the coating of Li_2FeSiO_4, with carbon black (which is amorphous), decreased the crystallinity of the compound, leading to the lower conductivity of the virgin compound and lowering its electrochemical performance.

The first path for further research would be optimizing the synthesis of Li_2FeSiO_4 so that higher electrochemical performance could be obtained. This could be achieved by improving the milling methods to produce smaller sized material. By using precursors of smaller particle size and shorter heating time, the final particle size of the material could be improved and one could avoid the formation of large agglomerates.

As mentioned before, large particle size material is not desired since the lithium ion has to migrate from the inside of the particle to the surface. The larger the particle, the longer will be the diffusion path and the diffusion time be.

Therefore, at higher current rates the lithium that is contained within the center of the particle will not be extracted as rapidly as surface ions, which will ultimately result in poor electrochemical performance.

A battery manufactured from large particle size materials could possibly only operate at very low current rates, thereby reducing it practicality. By reducing the particle size and increasing the surface area of the active materials, the diffusion path will be reduced and the lithium ion would have to travel shorter distances in order to

access the electrolyte faster. This should lead to better electrochemical performance and possibly better rate capabilities.

Also to achieve high purity cathode materials, the stoichiometric amounts of the starting materials should be more extensively studied in all the synthesis methods studied.

5. Economics

For this work two reagents were bought: EDOT and Iron Oxalate all the other reagents were already in the stock, so only the quantities used will be considered for the final calculations. Also the glass material used, since none of it was broken, will not be considered.

Table 5.1 - Weight, Volume, price and quantities used and money spent in the reagents for this work.

Reagent	Weight / g	Volume / L	price / €	€/g or L	Quantity used / g or L	Money spend / €
C_6H_8O7	1000.00	-	39.20	0.04	20.00	0.78
$FeC_2O_4.2H_2O$	250.00	-	27.80	0.11	20.00	2.22
$FeCl_2.4H_2O$	100.00	-	186.50	1.87	25.00	46.63
Li_2CO_3	100.00	-	30.20	0.30	15.00	4.53
LiOH	100.00	-	48.60	0.49	10.00	4.86
SiO_2	100.00	-	28.00	0.28	19.82	5.55
EDOT	10.00	-	69.50	6.95	20.00	139.00
NaPSS	100.00	-	65.80	0.66	20.00	13.16
$LiClO_4$	100.00	-	59.10	0.59	20.00	11.82
CH_3CN	-	1.00	207.50	207.50	0.20	41.50
N_2	-	56.00	365.00	6.52	30.00	195.54
					TOTAL	465.59

As shown in Table 5.1 the total of money spend in reagents was 465.59 €, excluding the MilliQ water and distillate water.

For each analysis in the characterization techniques, there is a price associated. Doing an estimation of the cost of each analysis and the number of analysis made, we can get the total of money spent.

Table 5.2 – Price for each analysis technique used, number of analysis made and money spend for this work.

Technic	Price / €	nº of analysis	Money spend / €
TGA/DSC	19.00	10	190.00
XDR	5.00	30	150.00
SEM	20.00	4	80.00
Ellipsometry	10.00	5	50.00
PBD	5.00	30	150.00
EQCM	5.00	30	150.00
		TOTAL	770.00

So by Table 5.2 the total of money spend was 770.00 €. This means that the sum of the amount of reagents used, and the analysis made is 1235.59 €.

Since this value represents around 80% of the total amount spent in this work, without including the water, electricity, liquid waste treatment, and maintenance of the laboratory, which represents the other 20%, the total amount is 1545.00 €.

6. Safety and Environmental concerns

All the experiments were performed using personal protective equipment (PPE) such as protective clothing, goggles, or other garment or equipment designed to protect the wearer's body from injury.

Also the facilities of the laboratory had the adequate ventilation, avoiding dust formation, breathing vapors, mist or gas of hazardous reagents.

In Table 0.1 (Appendix) is described the new labelling of the chemicals used in this work according with the new standard regulation by REACH. (http://ec.europa.eu/environment/chemicals/reach/review_2012_en.htm)

The reagents that need even more careful handling were the EDOT (Toxic), $FeCl_2.4H_2O$ (Corrosive), LiOH (Toxic and Corrosive) and SiO_2 (Carcinogetic).

All the waste of surplus and non-recyclable solutions were kept in proper packages and afterwards send to a licensed disposal company. None of products were disposed in the public drains.

One of the main concerns about this work, if the materials were fabricated in the industry, was the carbon dioxide production as a side product.

It is already known that industrial carbon dioxide can be produced by several methods, many of which are practiced at various scales of the industrial production of ammonia, for example. Although carbon dioxide is not often recovered, usually results from combustion of fossil fuels as well fermentation of sugar in the brewing of beer, whisky and other alcoholic beverages. It also results from thermal decomposition of limestone, CaCO3, in the manufacture of lime (calcium oxide, CaO).

Although all this, carbon dioxide is used in a variety of applications: precursor to chemicals, food, beverages, wine making, inert gas, fire extinguisher, supercritical CO_2 as solvent, agricultural and biological applications, oil recovery, etc. If a plant of carbon dioxide recovery was attached to the plant where the cathode materials were synthesized, this could be very profitable for the company.

References

1. *BP Global Reports and publications Statistical Review of World Energy*, 2012.

2. M. Aresta, *Carbon Dioxide Recovery and Utilization*, Springer, 2003.

3. H. Boll, W., Hochgesand, G., Higman, C., Supp, E., Kalteier, P., Müller, W.-D., Kriebel, M., Schlichting, H. and Tanz, *Gas Production, 3. Gas Treating*, Ullmann's Encyclopedia of Industrial Chemistry, Weinheim, Germany, 2011.

4. J. Richards, *Solar Energy*, Marshall Cavendish, 2009.

5. *http://www.sankey-diagrams.com/sun-energy-reloaded-or-make-it-look-nicer/*.

6. J. J.-M. Tarascon and M. Armand, *Nature*, 2001, **414**, 359–367.

7. D. Berndt, D. and Spahrbier, *Batteries*, Ullmann's Encyclopedia of Industrial Chemistry, Weinheim, Germany, 2001.

8. M. Wakihara, O. Yamamoto, and O. Wakihara, M; Yamamoto, *Lithium Ion Batteries Fundamentals and Performance*, WILEY-VCH Verlag GmbH, Weinheim, 1998.

9. U. Wietelmann and R. J. Bauer, in *Ullmann's Encyclopedia of Industrial Chemistry*, Wiley-VCH Verlag GmbH & Co. KGaA, 2000.

10. G. Nazri and G. Pistoia, *Lithium batteries: science and technology*, Springer, 2003.

11. W. A. Van Schalkwijk and B. Scrosati, *Advances in Lithium-Ion Batteries*, Kluwer Academic Publishers, Boston, 2002.

12. M. S. Whittingham, *Chemical Reviews*, 2004, **104**, 4271–4302.

13. A. Elschner, S. Kirchmeyer, W. Lovenich, U. Merker, and K. Reuter, *PEDOT: Principles and Applications of an Intrinsically Conductive Polymer (Google eBook)*, CRC Press, 2010.

14. E. Tamburri, S. Sarti, S. Orlanducci, M. L. Terranova, and M. Rossi, *Materials Chemistry and Physics*, 2011, **125**, 397–404.

15. S. Duluard, B. Ouvrard, a Celik-Cochet, G. Campet, U. Posset, G. Schottner, and M.-H. Delville, *The journal of physical chemistry. B*, 2010, **114**, 7445–51.

16. L. Groenendaal, F. Jonas, D. Freitag, H. Pielartzik, and J. R. Reynolds, *Advanced Materials*, 2000, **12**, 481–494.

17. B. Scrosati, *Polymer international*, 1998, **47**, 50–55.

18. T. Stöcker, A. Köhler, and R. Moos, *Journal of Polymer Science Part B: Polymer Physics*, 2012, **50**, 976–983.

19. B. Somboonsub, M. a. Invernale, S. Thongyai, P. Praserthdam, D. a. Scola, and G. a. Sotzing, *Polymer*, 2010, **51**, 1231–1236.

20. S. Y. Kim and G. T. R. Palmore, *Electrochimica Acta*, 2012, **77**, 184–188.

21. E. Poverenov, M. Li, A. Bitler, and M. Bendikov, *Chemistry of Materials*, 2010, **22**, 4019–4025.

22. a. I. Melato, M. H. Mendonça, and L. M. Abrantes, *Journal of Solid State Electrochemistry*, 2008, **13**, 417–426.

23. L. Zhan, Z. Song, J. Zhang, J. Tang, H. Zhan, Y. Zhou, and C. Zhan, *Electrochimica Acta*, 2008, **53**, 8319–8323.

24. S. Rattan, P. Singhal, and A. Verma, *Polymer Engineering and Science*, 2013.

25. Y. Xia and J. Ouyang, *Journal of Materials Chemistry*, 2011, **21**, 4927.

26. H.-W. Siao, S.-M. Chen, and K.-C. Lin, *Journal of Solid State Electrochemistry*, 2010, **15**, 1121–1128.

27. Y. H. Kim, C. Sachse, M. L. Machala, C. May, L. Müller-Meskamp, and K. Leo, *Advanced Functional Materials*, 2011, **21**, 1076–1081.

28. A. Onorato, M. a. Invernale, I. D. Berghorn, C. Pavlik, G. a. Sotzing, and M. B. Smith, *Synthetic Metals*, 2010, **160**, 2284–2289.

29. E. Tamburri, S. Orlanducci, F. Toschi, M. L. Terranova, and D. Passeri, *Synthetic Metals*, 2009, **159**, 406–414.

30. G. Henze, in *Ullmann's Encyclopedia of Industrial Chemistry*, Wiley- VCH Verlag GmbH & Co. KGaA, 2008.

31. J. O. Bockris, A. K. N. Reddy, and M. E. Gamboa-Aldeco, *Modern Electrochemistry 2A: Fundamentals of Electrodics*, Springer, 2001.

32. A. J. Bard and L. R. Faulkner, *Electrochemical Methods: Fundamentals and Applications*, Wiley, 2000.

33. R. Kötz, C. Barbero, and O. Haas, *Berichte der Bunsengesellschaft für physikalische Chemie*, 2010, **97**, 427–430.

34. E. Vieil, K. Meerholz, T. Matencio, and J. Heinze, *Journal of Electroanalytical Chemistry*, 1994, **368**, 183–191.

35. G. G. Láng and C. A. Barbero, *Laser Techniques for the Study of Electrode Processes*, Springer, 2012.

36. C. A. Barbero and M. C. Miras, *The Journal of the Argentine Chemical Society*, 2003, **91**, 1–40.

37. E. Vieil and C. Lopez, *Journal of Electroanalytical Chemistry*, 1999, **466**, 218–233.

38. W. Plieth, A. Bund, U. Rammelt, S. Neudeck, and L. Duc, *Electrochimica Acta*, 2006, **51**, 2366–2372.

39. J. C. Rivière, L. Fabry, S. Pahlke, A. Quentmeier, K. Hinrichs, W. Hill, B. Gruska, A. Röseler, and G. Friedbacher, in *Ullmann's Encyclopedia of Industrial Chemistry*, Wiley-VCH Verlag GmbH & Co. KGaA, 2000.

40. K. Hunger, P. Mischke, and W. Rieper, in *Ullmann's Encyclopedia of Industrial Chemistry*, Wiley-VCH Verlag GmbH & Co. KGaA, 2000.

41. D. D. B. Hibbert, K. Weitzner, B. Tabor, and P. Carter, *Biomaterials*, 2000, **21**, 2177–2182.

42. Q. Xie, Z. Li, C. Deng, M. Liu, Y. Zhang, M. Ma, S. Xia, X. Xiao, D. Yin, and S. Yao, *Journal of Chemical Education*, 2007, **84**, 681–684.

43. a. R. Hillman, S. J. Daisley, and S. Bruckenstein, *Electrochimica Acta*, 2008, **53**, 3763–3771.

44. A. Lisowska-Oleksiak, K. Kazubowska, and A. Kupniewska, *Journal of Electroanalytical Chemistry*, 2001, **501**, 54–61.

45. V. Syritski, K. Idla, and A. Öpik, *Synthetic Metals*, 2004, **144**, 235–239.

46. C. H. G. Tompkins and E. A. Irene, *Handbook of Ellipsometry*, Springer-Verlag GmbH, 2005.

47. L. M. M. Abrantes, J. P. P. Correia, and a. I. I. Melato, *Journal of Electroanalytical Chemistry*, 2010, **646**, 75–84.

48. J. P. Correia, L. M. Abrantes, and E. Vieil, *Materials Science Forum*, 2004, **455-456**, 657–660.

49. W. Rudolph, M. H. Brooker, and C. C. Pye, *The Journal of Physical Chemistry*, 1995, **99**, 3793–3797.

50. C. Bock, G. Markham, A. Katz, and J. Glusker, *Theoretical Chemistry Accounts*, 2006, **115**, 100–112.

51. R. C. Longo, K. Xiong, W. Wang, and K. Cho, *Electrochimica Acta*, 2012, **80**, 84–89.

52. N. Yabuuchi, Y. Yamakawa, K. Yoshii, and S. Komaba, *Dalton Transactions*, 2011, **40**, 1846–1848.

53. Z. Zheng, Y. Wang, A. Zhang, T. Zhang, F. Cheng, Z. Tao, and J. Chen, *Journal of Power Sources*, 2012, **198**, 229–235.

54. H. GUO, K. Xiang, X. CAO, X. Li, Z. WANG, and L. LI, *Transactions of Nonferrous Metals Society of China*, 2009, **19**, 166–169.

55. B. Huang, X. Zheng, and M. Lu, *Journal of Alloys and Compounds*, 2012, **525**, 110–113.

56. J. W. Fergus, *Journal of Power Sources*, 2010, **195**, 939–954.

57. B. L. Ellis, K. Town, and L. F. Nazar, *Electrochimica Acta*, 2012, **84**, 145–154.

58. C. Eames and A. Armstrong, *Chemistry of Materials*, 2012, **24**, 2155–2161.

59. B. Xu, D. Qian, Z. Wang, and Y. S. Meng, *Materials Science and Engineering: R: Reports*, 2012, **73**, 51–65.

60. H. Hao, J. Wang, J. Liu, T. Huang, and A. Yu, *Journal of Power Sources*, 2012, **210**, 397–401.

61. A. Liivat and J. O. Thomas, *Solid State Ionics*, 2011, **192**, 58–64.

62. A. Saracibar, *Chemistry of Materials*, 2012, **24**, 495–503.

63. R. Yang, X. Liu, Y. Qu, J. Lei, and J.-H. Ahn, *Transactions of Nonferrous Metals Society of China*, 2012, **22**, 2529–2534.

64. D.-H. Seo, H. Kim, I. Park, J. Hong, and K. Kang, *Physical Review B*, 2011, **84**, 220106.

65. a R. Armstrong, N. Kuganathan, M. S. Islam, and P. G. Bruce, *Journal of the American Chemical Society*, 2011, **133**, 13031–5.

66. C. Sirisopanaporn, A. Boulineau, D. Hanzel, R. Dominko, B. Budic, a R. Armstrong, P. G. Bruce, and C. Masquelier, *Inorganic chemistry*, 2010, **49**, 7446–51.

67. A. Nytén, A. Abouimrane, M. Armand, T. Gustafsson, and J. O. Thomas, *Electrochemistry Communications*, 2005, **7**, 156–160.

68. A. Nytén, M. Stjerndahl, H. Rensmo, H. Siegbahn, M. Armand, T. Gustafsson, K. Edstr?m, and J. O. Thomas, *Journal of Materials Chemistry*, 2006, **16**, 3483.

69. R. Dominko, D. E. Conte, D. Hanzel, M. Gaberscek, and J. Jamnik, *Journal of Power Sources*, 2008, **178**, 842–847.

70. X. Huang, X. Li, H. Wang, Z. Pan, M. Qu, and Z. Yu, *Electrochimica Acta*, 2010, **55**, 7362–7366.

71. L. Li, H. Guo, X. Li, Z. Wang, W. Peng, K. Xiang, and X. Cao, *Journal of Power Sources*, 2009, **189**, 45–50.

72. B. Shao and I. Taniguchi, *Journal of Power Sources*, 2012, **199**, 278–286.

73. X. Huang, X. Li, H. Wang, Z. Pan, M. Qu, and Z. Yu, *Solid State Ionics*, 2010, **181**, 1451–1455.

74. C. Deng, S. Zhang, B. L. L. Fu, S. Y. Y. Yang, and L. Ma, *Materials Chemistry and Physics*, 2010, **120**, 14–17.

75. C. Sirisopanaporn, C. Masquelier, P. G. Bruce, a R. Armstrong, and R. Dominko, *Journal of the American Chemical Society*, 2011, **133**, 1263–5.

76. R. Dominko, M. Bele, M. Gaberšček, a. Meden, M. Remškar, and J. Jamnik, *Electrochemistry Communications*, 2006, **8**, 217–222.

77. C. Deng, S. Zhang, and S. Y. Yang, *Journal of Alloys and Compounds*, 2009, **487**, L18–L23.

78. X.-Y. Fan, Y. Li, J.-J. Wang, L. Gou, P. Zhao, D.-L. Li, L. Huang, and S.-G. Sun, *Journal of Alloys and Compounds*, 2010, **493**, 77–80.

79. K. Zaghib, a. Ait Salah, N. Ravet, a. Mauger, F. Gendron, and C. M. M. Julien, *Journal of Power Sources*, 2006, **160**, 1381–1386.

80. M. Zhang, Q. Q. Chen, Z. Xi, and Y. Hou, *Journal of Materials Science*, 2012, **47**, 2328–2332.

81. D. A. Skoog, F. J. Holler, and S. R. Crouch, *Principles of Instrumental Analysis*, Brooks/Cole, 2007.

82. E. F. Paulus and A. Gieren, in *Ullmann's Encyclopedia of Industrial Chemistry*, Wiley VCH Verlag GmbH & Co. KGaA, 2001.

83. J. A. GOLDSTEIN, *Scanning Electron Microscopy and X-Ray Microanalysis*, Kluwer Academic Pub, 2003.

84. A. Kriete, H. Gundlach, S. Amelinckx, and L. Reimer, in *Ullmann's Encyclopedia of Industrial Chemistry*, Wiley-VCH Verlag GmbH & Co. KGaA, 2000.

85. S. B. Warrington and G. W. H. Höhne, in *Ullmann's Encyclopedia of Industrial Chemistry*, Wiley-VCH Verlag GmbH & Co. KGaA, 2008.

86. *Handbook of Thermal Analysis and Calorimetry: Recent Advances, Techniques and Applications*, Elsevier, 2007.

87. M. E. Brown, *Introduction to Thermal Analysis: Techniques and Applications*, Springer, 2001.

88. P. J. Haines, *Thermal Analysis and Calorimetry*, Royal Society of Chemistry, 2002.

89. P. Arora and Z. (John) Zhang, *Chemical Reviews*, 2004, **104**, 4419–4462.

90. C. Deng, S. Zhang, Y. Gao, B. Wu, L. Ma, Y. H. H. Sun, B. L. L. Fu, Q. Wu, and F. L. L. Liu, *Electrochimica Acta*, 2011, **56**, 7327–7333.

91. G. Hu, Y. Cao, Z. Peng, and C. A. O. Y.-B. HU Guo-Rong PENG Zhong-Dong, DU Ke, JIANG Qing-Lai, *Acta Physico-Chimica Sinica*, 2009, **25**, 1004–1008.

92. V. Berbenni, A. Marini, G. Bruni, and R. Riccardi, *Thermochimica Acta*, 2000, **346**, 115–132.

93. R. Dominko, *Journal of Power Sources*, 2008, **184**, 462–468.

94. J. Häglund, A. Fernández Guillermet, G. Grimvall, and M. Körling, *Physical Review B*, 1993, **48**, 11685–11691.

95. J. Laugier and B. Bochu, 2007.

Appendix

Table 0.1 - Chemical formula, labelling and pictograms of all the reagents used in this work.

	Labelling according Regulation (EC) No 1272/2008 [CLP]	
Chemical Formula	**MSDS**	**Pictogram**
$C_6H_8O_7$	**Hazard statements** H319 Causes serious eye irritation. **Precautionary statements** P305 + P351 + P338 IF IN EYES: Rinse cautiously with water for several minutes. Remove contact lenses, if present and easy to do. Continue rinsing.	
CH_3CN	**Hazard statements** H225 Highly flammable liquid and vapour. H302 Harmful if swallowed. H312 Harmful in contact with skin. H319 Causes serious eye irritation. H332 Harmful if inhaled. **Precautionary statements** P210 Keep away from heat/sparks/open flames/hot surfaces. - No smoking. P280 Wear protective gloves/ protective clothing. P305 + P351 + P338 IF IN EYES: Rinse cautiously with water for several minutes. Remove contact lenses, if present and easy to do. Continue rinsing.	 
EDOT	**Hazard statements** H302 Harmful if swallowed. H311 Toxic in contact with skin. H319 Causes serious eye irritation. **Precautionary statements** P280 Wear protective gloves/ protective clothing. P305 + P351 + P338 IF IN EYES: Rinse cautiously with water for several minutes. Remove contact lenses, if present and easy to do. Continue rinsing. P312 Call a POISON CENTER or doctor/ physician if you feel unwell.	

$FeC_2O_4 \cdot 2H_2O$	**Hazard statements** H302 Harmful if swallowed. H312 Harmful in contact with skin. **Precautionary statements** P280 Wear protective gloves/ protective clothing.	
$FeCl_2 \cdot 4H_2O$	**Hazard statements** H302 Harmful if swallowed. H314 Causes severe skin burns and eye damage. **Precautionary statements** P280 Wear protective gloves/ protective clothing/ eye protection/ face protection. P305 + P351 + P338 IF IN EYES: Rinse cautiously with water for several minutes. Remove contact lenses, if present and easy to do. Continue rinsing. P310 Immediately call a POISON CENTER or doctor/ physician.	 
$LiClO_4$	**Hazard statements** H272 May intensify fire; oxidizer. H315 Causes skin irritation. H319 Causes serious eye irritation. H335 May cause respiratory irritation. **Precautionary statements** P220 Keep/Store away from clothing/ combustible materials. P261 Avoid breathing dust. P305 + P351 + P338 IF IN EYES: Rinse cautiously with water for several minutes. Remove contact lenses, if present and easy to do. Continue rinsing.	 
LiOH	**Hazard statements** H301 + H331 Toxic if swallowed or if inhaled H314 Causes severe skin burns and eye damage. **Precautionary statements** P261 Avoid breathing dust. P280 Wear protective gloves/ protective clothing/ eye protection/ face protection. P301 + P310 IF SWALLOWED: Immediately call a POISON CENTER or doctor/physician. P305 + P351 + P338 IF IN EYES: Rinse cautiously with water for several minutes. Remove contact lenses, if present and easy to do. Continue rinsing.	 

	P310 Immediately call a POISON CENTER or doctor/ physician.	
Li_2CO_3	**Hazard statements** H302 Harmful if swallowed. H319 Causes serious eye irritation. **Precautionary statements** P305 + P351 + P338 IF IN EYES: Rinse cautiously with water for several minutes. Remove contact lenses, if present and easy to do. Continue rinsing.	
N_2	**Hazard statements** H280 Contains gas under pressure; may explode if heated. **Precautionary statements** P410 + P403 Protect from sunlight. Store in a well-ventilated place.	
NaPSS	**If inhaled:** If breathed in, move person into fresh air. If not breathing, give artificial respiration. **In case of skin contact:** Wash off with soap and plenty of water. **In case of eye contact:** Flush eyes with water as a precaution.	
SiO_2	**Hazard statements** H373 May cause damage to organs through prolonged or repeated exposure if inhaled.